Multidimensional inversion of MT data from Alid Geothermal area, Eritrea; comparison with geological structures and identification of a geothermal reservoir

Andemariam Teklesenbet Beyene

Faculty of Earth Sciences
University of Iceland
2012

Multidimensional inversion of MT data from Alid Geothermal area, Eritrea; comparison with geological structures and identification of a geothermal reservoir

Andemariam Teklesenbet Beyene

60 ECTS thesis submitted in partial fulfillment of a
Magister Scientiarum degree in Geophysics

Advisors
Gylfi Páll Hersir
Knútur Árnason

Examiner
Dr. Hjálmar Eysteinsson

Faculty of Earth Sciences
School of Engineering and Natural Sciences
University of Iceland
Reykjavik, January 2012

Multidimensional inversion of MT data from Alid Geothermal area, Eritrea; comparison with geological structures and identification of a geothermal reservoir

Multidimensional inversion of MT data
60 ECTS thesis submitted in partial fulfillment of a *Magister Scientiarum* degree in Geophysics

Abstract

Electrical resistivity methods have been the most powerful tool in geothermal exploration for decades. Of these, MT and TEM are important methods in delineating geothermal resources.

The main objective of this study is to understand the nature (dimensionality) of the MT data from Alid Geothermal area, Eritrea and apply multidimensional inversion to the data and compare the result with geological structures and the identification of a geothermal reservoir. In this project, 47 MT soundings from Alid geothermal area were used for 1D and 3D inversion as well as 2D along four profiles, for inversion. MT data have traditionally been inverted in 1D and 2D for several decades but with the advancement of modern computing techniques, 3D modelling and inversion is now becoming a more general method. 3D MT inversion has been used in various fields such as geothermal studies.

For the purpose of static shift correction, in the 1D inversion, the MT data were jointly inverted with transient electromagnetic (TEM) data from the same location or close by. In the 2D inversion, the apparent resistivity for both the xy and yx modes were previously shift corrected prior to inversion. Whereas for the 3D inversion, shift correction was previously applied to the impedance tensor.

According to the dimensionality analysis, the dimensional indicators of most of the impedance tensors of Alid MT data indicate that the resistivity structure is highly three dimensional or at least of a strong non-1D nature for long periods, greater than 1 s. The resistivity distribution from the models of 3D inversion is comparable to the model results of 1D TEM/MT joint inversion at shallow depths down to about 1 km below the surface. At deeper levels the resulting models from 1D and 3D inversion are different.

Four main resistivity structures are observed in most parts of the survey area mainly from 1D and 3D inversion: A shallow thin high resistivity layer followed by low resistivity. Below there is a high resistivity layer underlain by a deep laying conductor. Lithological contacts or lineaments are identified by the three inversion approaches. A sharp resistivity contact or fault line with an orientation of NE-SW is observed at the depth intervals of approximately 0.5-2 km. This fault line is clearly observed particularly from the modelling result of 3D inversion where the southern side of the fault line is downthrown.

Dedication

I would like to dedicate my thesis to my beloved wife, sons, mother, brothers and sisters.

Preface

Alid is a high temperature geothermal area. It is within a graben located in the south eastern part of Eritrea about 30 km south of the Gulf of Zula along the axis of the East African rift valley bounded by the Eritrean high land to the west and the Danakil Alps to the east.

Previously, several surface geo-scientific works including geology, geochemistry and geophysics were done to delineate the geothermal reservoir in the area. The Icelandic International Development Agency (ICEIDA) funded a geophysical survey (MT and TEM) to explore the Alid geothermal potential. Iceland GeoSurvey (ÍSOR) in collaboration with Eritrean Geological Survey (EGS) conducted a detailed MT/TEM survey in late 2008. The field survey was accomplished by a team from ÍSOR and EGS. The team included the project manager, Dr. Hjálmar Eysteinsson and Guðni Karl Rosenkjær, both geophysicists from ÍSOR, Yonas Estifanos, Mussie Beraki and myself, geophysicists from EGS and Debesai Habte, field assistant from GSE. In addition, two cooks, Rigat Mokenen and Azeb Hagos, and two drivers, Berhane and Salhadin as well as several local workers participated in the survey.

During the field work, a total of 52 MT soundings were measured using four units of MT equipments out of which one served as a remote reference, and 67 TEM soundings were performed with one set of TEM equipment. The terrain in the survey area was difficult and therefore two four-wheel pickup cars, four six-wheel motor bikes and camels were used in the survey. During the data acquisition two groups worked in the field, one for each method of measurements.

A technical report based on 1D inversion of the data was published by ÍSOR in early 2009 (Eysteinsson et al., 2009). This thesis is done in partial fulfilment of the degree of Master of Science in Geophysics and submitted to the University of Iceland accounting for the 60 ECTS units as needed out of the 120 ECTS units required for the degree. In addition, this work is believed to contribute to a better understanding of the resistivity distribution of the geothermal area.

Andemariam Teklesenbet

Table of Contents

List of Figures

xii

Explanation of Symbols

Notation

E (V m^{-1})	Electric field
B (T)	Magnetic Induction
H (A m^{-1})	Magnetic intensity
D (C m^{-2})	Electric Displacement
η (Cm^{-3})	Electric Charge Density of free charges
j (Am^{-2})	Electric Current Density
σ (Sm^{-1})	Electric Conductivity
μ (H/m)	Magnetic Permeability
ε (F/m)	Electric Permittivity
δ (m)	Electromagnetic Skin Depth
T (s)	Period
f (Hz)	Frequency
t (s)	Time
ω (rad/s)	Angular Frequency
ρ (Ωm)	Resistivity (specific resistance)
$\hat{Z}$(Ω)	Impedance tensor (2x2 matrices)
$\hat{Y}$ ((Ωm)$^{-1}$ or S)	Admittance
k (m^{-1})	Propagation Constant (wave number)
x, y and x$'$, y$'$	Reference Frame and Reference Frame Rotated through an angle α
$\mathcal{T}$	Tipper
$\Re$	Real part of the Tipper
$\Im$	Imaginary part of the Tipper
M$_r$	Length of the real part of the induction arrow
M$_q$	Length of the imaginary part of the induction arrow
ρ_a (Ωm)	Apparent Resistivity
ϕ (°)	Impedance phase
i=$\sqrt{-1}$	Imaginary number

Acronyms and abbreviations

MT	Magnetotelluric
TEM	Transient Electromagnetic
ÍSOR	Iceland GeoSurvey
EGS	Eritrean Geological Survey
TE	Transverse Electric
TM	Transverse Magnetic
1D	One Dimensional
2D	Two Dimensional
3D	Three Dimensional
REBOCC	REduced Basis OCCam Inversion
EM	Electromagnetic

Acknowledgements

1 Introduction

Geophysics, in particularly electrical resistivity methods, Magnetotellurics (MT) and Transient Electromagnetics (TEM) have been the most powerful tools in geothermal exploration to explore the geothermal properties of geothermal reservoirs for decades. With these methods, the physical properties of the earth's crust are examined. The main role and activity of geothermal exploration through the use of these geophysical methods is to detect and delineate geothermal resources; locate exploitable reservoirs and to site drill holes, through which hot fluids at depth can be extracted. Generally, most of the geophysical methods have been applied in geothermal prospecting; however, various electrical and thermal methods have been the most useful. Rocks containing geothermal fluids are usually characterized by anomalous low resistivity. Those methods which measure the electrical resistivity at depth have been the most useful of all geophysical methods and used to locate geothermal reservoirs.

The electrical resistivity of rock units is greatly influenced by properties such as fluid content, porosity, degree of fracturing, temperature, and mineral content (Keller, 1989). Saline fluids within pore spaces and fracture openings can reduce the resistivity of a rock matrix considerably. Resistivity can also be decreased by the presence of conductive clay minerals and metallic mineralization. It is common for altered volcanic rocks to contain authigenic minerals that are ten times more conductive than the surrounding rocks and provided that those altered minerals are connected, they will reduce the resistivity of rock matrices considerably (Nelson and Anderson, 1992). Increased temperature generally causes higher ionic mobility and therefore; increased temperature reduces the rock resistivity. In volcanic areas this can be reversed where high temperature minerals like chlorite and epidote will increase the rock resistivity (see e.g., Árnason and Flóvenz, 1992). Unaltered rocks are moderately to highly resistive (hundreds to thousands of Ωm), whereas fault zones will show lower resistivity when they host fluid (Eberhart-Phillips et al., 1995).

This paper describes interpretation of resistivity data from Alid geothermal area. Alid geothermal area is in a graben located in the south eastern part of Eritrea about 30 km south of the Gulf of Zula along the axis of the East African rift valley bounded by the Eritrean high land to the west and the Danakil Alps to the east (Figure 2.1). From previous geochemical studies and due to plenty of surface manifestations observed on the ground, Alid area is believed to be a high temperature geothermal field. Gas geothermometers indicate reservoir temperatures of >250°C for Ilegedi, the largest and most active of the Alid geothermal manifestations (Clynne et al., 1996; Yohannes, 2004).

In 2008, Icelandic International Development Agency (ICEIDA) funded a geophysical survey (MT and TEM) in Alid to investigate a possible geothermal potential. Iceland GeoSurvey (ÍSOR), in collaboration with Eritrean Geological Survey (EGS), conducted the MT/TEM survey in Alid in late 2008 (Eysteinsson et al., 2009).

This thesis focuses on the electromagnetic data from this project to identify the geoelectrical structures and delineate, if possible, the geothermal reservoir in the Alid area using multidimensional inversion techniques. In this project, 47 MT soundings from Alid geothermal field were used for 3D interpretation. MT data have traditionally been inverted in 1D and 2D for decades but with the advancement of modern computing techniques, 3D modelling and inversion is now becoming a more general method. 3D MT inversion has been used in various fields such as geothermal studies (e.g., Han et al., 2008; Newman et al., 2008; Árnason et al., 2010; Cumming and Mackie, 2010).

In this study a 1D inversion of TEM/MT data is applied using TEMTD Occam inversion code from Knútur Árnason (2006a), 2D inversion using REBOCC programme from Siripunvaraporn and Egbert (2000) and 3D inversion using WSINV3DMT programme (Siripunvaraporn et al., 2005). For the 1D, in order to correct the static shift, the MT data were jointly inverted with TEM soundings at the same site. For 2D and 3D cases, the MT data were shift corrected for each mode with TEM soundings before the inversion. The results from the 1D inversion are presented as 1D models for each sounding, as iso-resistivity maps at different elevations as well as resistivity cross-sections. For the 2D inversion, the results are presented as resistivity cross-sections; and the results from the 3D inversion are presented as iso-resistivity maps at different elevations as well as resistivity cross-sections.

In this thesis, overview of the regional and local geology and previous work in Alid area is discussed in chapter 2. Theoretical basis of MT is discussed in chapter 3. Solutions to the wave equations in a horizontally layered earth are discussed. The concept of impedance and its rotations is discussed in detail. Apparent resistivity and phase are derived. Field procedure and real data processing are discussed in chapter 4.

Understanding the inherent dimensionality and geo-electric strike of MT data is an important step in interpreting the data; therefore, dimensionality and strike direction of the data are discussed in chapter 5. In addition, static shift problem and its remedy using central-loop TEM data acquired at the same location is also discussed in chapter 5. The different inversion and results of the inversions are discussed in chapter 6. Lastly, discussion of the results as well as conclusion and recommendation are given in chapter 7.

2 Geological and Geothermal Conditions of Alid Area

The Alid geothermal area is located about 120 km southeast of the port city of Massawa and about 30 km south of Gulf of Zula on the axis of the Danakil depression in the East-African Rift system. (see Figure 2.1).

2.1 Regional Tectonic Setting

The African continent is slowly splitting apart along the East African rift valley, a 3000 km long series of deep basins and flanking mountain ranges. In the Afar depression in south eastern Eritrea and northern Ethiopia (Figure 2.1), the Earth's outermost shell, usually a relatively rigid, 150 km thick plate, has been stretched, thinned and heated to the point of breaking. Hot, partially melted rocks are rising up from the Earth's mantle and are either erupting at the Earth's surface or cooling within the crust. Rifting of Africa and Arabia during the past ~30 Myr produced the ~300 km wide Afar depression, which comprises the Afar triple junction (Figure 2.1). The three rift arms, the Red Sea, Gulf of Aden and East African Rift formed within a Palaeogene flood basalt province associated with the Afar mantle plume (Hayward and Ebinger, 1996, Hirn et al., 1993, Ruegg et al., 1993).

The Danakil depression is a segment of the spreading system that has opened from the Red Sea. Crustal spreading along the axis of the Red Sea is transferred to spreading along the Danakil segment in a right stepping en echelon pattern (Barberi and Varet, 1977). The northern Danakil depression lies near or below sea level for the most of its extent. It is surrounded by the Nubian Plate (comprising the Eritrean-Ethiopian plateau and escarpment) to the west, by the Eritrean Danakil horst to the east, by the Somalian plateau and escarpment to the south, and the Gulf of Zula to the north (Figure 2.1). These bordering regions, the Nubian plate and the Somalian plate are covered primarily by Precambrian gneiss; granite and schist, while the Danakil horst constitutes mainly stratoid basalts. Much of the Afar lowland is covered with Pliocene and Quaternary lavas (CNR-CNRS, 1973). ErtaÁle, one of the most active volcanoes in the world, lies on the same spreading axis as Alid and about 140 km south east of it on the Ethiopian side (Figure 2.1a and c).

Recently, there was a volcanic eruption in Nabro volcano in the Danakil depression located ~240 km southeast of Alid (Figure 2a and b). It is the highest volcano (2218 m) in the Danakil depression. The eruption started on June 13, 2011 after a series of earthquakes ranging up to a magnitude of 5.7 and lasted for several months.
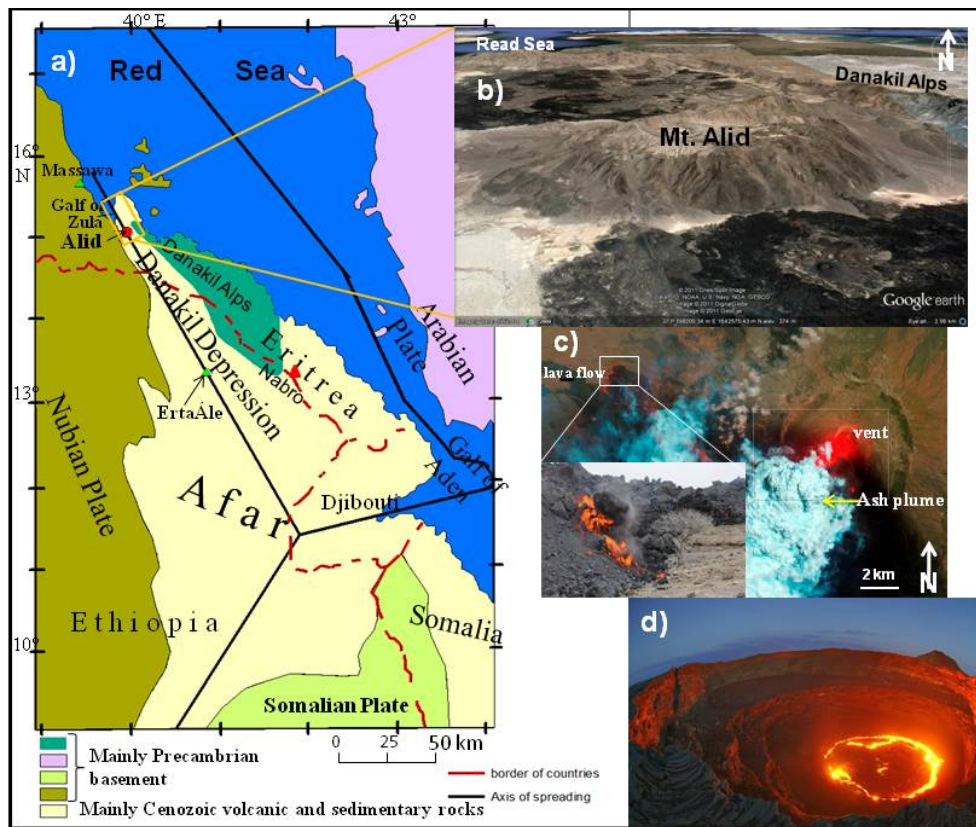
Figure 2.1. (a) Simplified plate tectonic map of the Afar triangle, modified from Barberi and Varet, 1977. (b) satellite image of Alid area, from Google earth. (c) Nabro volcanic eruption, (http://earthquake-report.com, 2011 and www.shabait.com, 2011) (d) ErtaÁle lava lake,(http://www.swisseduc.ch/stromboli/perm/erta/lava-lake,2008)

2.2 Geological and Geothermal setting of Alid

Alid volcanic center is an uplifted, elliptical structural dome which is believed to be formed during an uplift caused by shallow intrusion of rhyolitic magma, some of which was erupted (Clynne et al., 1996). The Alid dome rises as a single mountain roughly to an elevation of about 700 m above the flat surrounding plains of the Danakil depression, to a summit of 904 m. The major axis of Alid dome is 7 km, elongated ENE-WSW, perpendicular to the trend of the rift axis and the minor axis is about 5 km long, parallel to the rift spreading axis (Figure 2.2). Terrain of the Alid volcanic centre is characterized by small to medium and sometimes even high hills and ridges with high cliffs encircling the mountain almost all around.

The Alid volcanic system comprises the Alid dome as a central volcano with a collapsed structure at its central region and a NNW-SSE fissure swarm which transects it. Generally, Alid and its surrounding areas are covered with a variety of rock types. Quaternary basaltic lava flows cover an extensive area north and south of Alid Mountain (Figure 2.2). These young basaltic lava flows which bank unconformably against the foot of the mountain, erupted from the volcanic centres and NNW-SSE trending fissures of the rift axis (Figure 2.2). Scoria and pahoehoe lava flows are the main structural features within these young lava flows with many big caves and fractures. Alluvial and Aeolian sediments also extensively cover the plains around Alid lying mostly on the young basaltic lava.

4

The Alid Mountain itself has a complex geology, consisting dominantly of rhyolite flows, basalts, pyroclastics and sedimentary rocks (Figure 2.2). Silicic lavas and pyroclastics are restricted to the Alid dome but basaltic lavas are found along the fissure swarm to the north and south of it. A volcanic shadow zone is thus present as suggested by Lowenstern et al., 1999. This would imply a zoned magma chamber underneath the dome where basaltic magma does not penetrate the silisic upper section but escapes laterally as dykes to be erupted occasionally on the fissure swarm. The oldest rocks to crop out on Alid are Precambrian quartz-mica and kyanite schists found within a deep canyon, that drains the east side of the mountain. Overlying this basement rock is the sedimentary sequence, consisting of marine siltstone and sandstone, pillow basalt, subaerial basalt, anhydrite beds and fossiliferous limestone, all interpreted to be Pleistocene in age (Clynne et al., 1996; Duffield et al., 1997). Stratigraphically above the sedimentary sequence is the lava shell, which consists of basalt and basaltic andesite lava flows, pyroclastic deposits, amphibole-bearing rhyolite domes, and intercalated Aeolian sands.

West of Alid, the Eritrean highland side exposes metamorphic basement of both low grade and high grade sequences. The low-grade and high-grade sequences are in contact directly west of the village of Buya, almost parallel to the long axis of mount Alid which is ENE-WSW. Rock units on both sides of the contact zone are highly altered and foliated. Dolomitic rock, marble, graphitic slate and calcareous meta-sediments which extend south of the contact zone are the main constituents of the low-grade metamorphic rocks; whereas, Kyanite schist, amphibolite gneiss and granite gneiss which extend north of the contact zone are the main constituents of the high-grade metamorphic rocks.

According to geochemical studies conducted so far, Alid area is considered to be a high temperature geothermal field as is obvious from abundant surface manifestations. Gas geothermometers indicate reservoir temperatures of >250°C for Ilegedi, the largest and most active of the Alid geothermal manifestations (Clynne et al., 1996, Yohannes, 2004).

Alid area is situated in the arid to semi-arid climatic zone and rainfall is moderate. The hydro-geological condition for possible means of recharge water for Alid geothermal area was studied by Andemariam et al. (2006). The highlands on the western side of Alid are believed to be the main catchment area from which water drains to the geothermal system through fractures, faults and fissures.
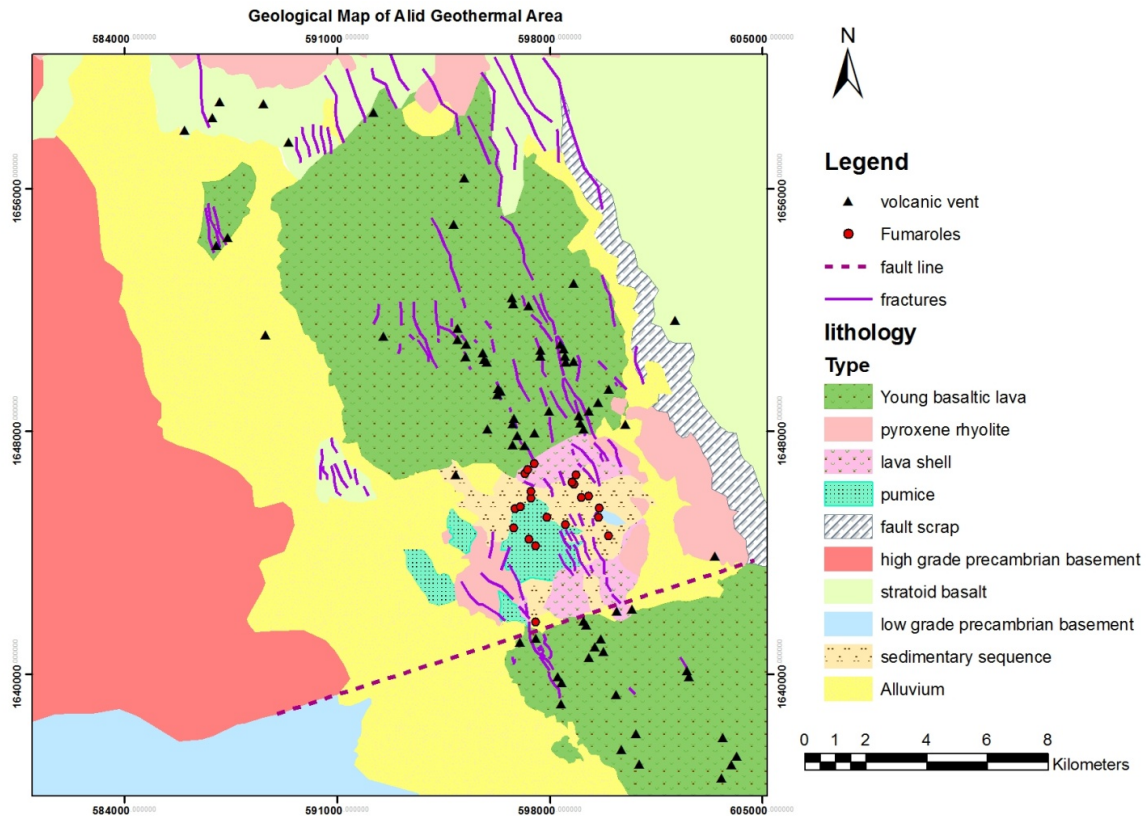
Figure 2.2. Simplified geological map of Alid and its surrounding areas, modified after Clynne et al., 1996 and Andemariam et al., 2006.

2.3 Previous Geothermal Exploration

The history of geothermal exploration in Alid area dates back to 1901-02, when the Italian Institute for military Geography, headed by Angelo Marini, conducted detailed study on Mt. Alid and its environs. The following years, several articles were puplished based on the studies done in the specified period. The article by Marini (1938) contains details on topography, geology, hydrology, fumaroles, seismicity along with place names of Alid area.

Another campaign was conducted by the Ethiopian Geological Survey sponsered by UNDP in 1973. During this survey fumaroles in Alid were mapped. These preliminary works laid grounds for further studies. After the Eritrean independence in 1991, detailed geological and geochemical studies were carried out for the first time in 1996 (Clynne et al., 1996). The USAID funded work was conducted by a team of staff members of the United States Geological Survey (USGS) and a team from Mininstry of Energy and Mines of Eritrea (MEM). In the study, a detailed geological map of Mt. Alid and its vicinity was developed, from which the geological map (Figure 2.2) in this paper is modified. From the geochemical anlysis made, a high temperature (> 250°C) reservoir was proposed to exist below Alid volcanic center. Figure 2.3 shows a conceptual geological cross section through the Alid volcano (Clynne et al., 1996).

In late 2005, the Eritrean Geological Survey (EGS) conducted some surveys in Alid geothermal area. The work was carried out by two groups: a group of geophysicists that conducted a DC resistivity survey on top of Mt. Alid with the aim of delineating structures

or discontinuities (lineaments, faults, etc) related to geothermal activities (Goitom et al., 2006) and a group of geologists that made assessment of faults and fractures as well as mapping of geothermal manifestations (Yohannes et al., 2006). In addition to this, in early 2006, a detailed study of the hydrogeological condition of the Alid area was done by a team of hydrogeologists from EGS (Andemariam et al., 2006).
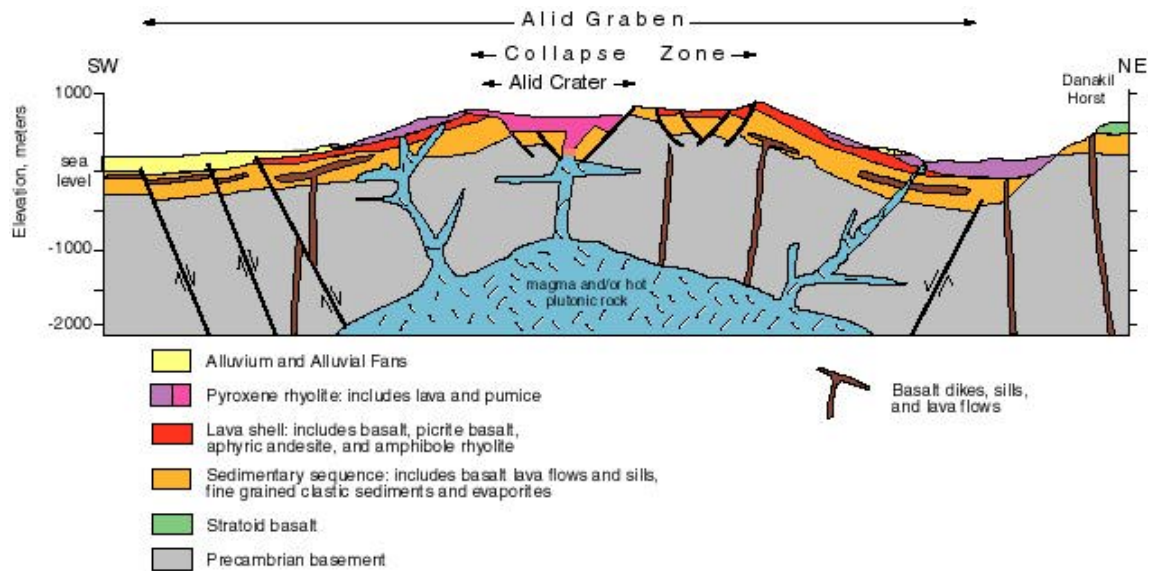
Figure 2.3. Schematic SW-NE geological cross-section through Mt. Alid, (Clynne et al., 1996 taken from http://volcanos.usgs.gov/yvo/aboutus/jlowenstern/alidmaps.html)

3 Magnetotelluric (MT) method

3.1 Basic theory

Magnetotellurics (MT) was originally suggested and developed by Tikhonov (1950) and Cagniard (1953). It is a natural source (passive) electromagnetic geophysical method that images the electrical properties of the earth. Tikhonov for the first time showed that at low frequencies the time derivative of the horizontal magnetic field (**H**) is proportional to the horizontal orthogonal component of the electric field (**E**). While Cagniard who often is accredited to be the father of MT developed formulas relating E_x and H_y on the surface of a layered medium with a plane wave source. Natural variations in the earth´s magnetic field induce electric field (telluric currents) under the earth´s surface. Depending on signal frequency and resistivity of penetrated material, the MT method can resolve geo-electric structures from depths of tens of meters to depths of hundreds of kilometres (Vozoff, 1972 & 1991). There are two frequency ranges: high frequency range and low frequency range. High frequency signals (short wavelengths) image shallow depths while low frequency signals (long wavelengths) have greater penetration depth.

The MT method depends on the penetration of the EM energy into the Earth, which operates under two main assumptions. The first assumption is quasi-static approximation which states that the electrical conduction currents are always much larger than the electrical displacement current; the earth is assumed to be a good conductor, that is $\sigma \gg \omega\varepsilon$. The second assumption is a plane wave source. Because of the large resistivity contrast at the air-Earth interface an incoming natural EM field propagates essentially vertically into Earth causing a vertical refraction of both fields transmitted into the earth (Vozoff, 1972).

The MT method uses broad band electromagnetic field fluctuations with periods ranging, from 10^{-3} s to 10^5 s (or between frequencies of 10^3 Hz to 10^{-5} Hz).

3.1.1 MT source field

There are two main sources which give rise to the MT signal, lightning and solar wind. Meteorological activities such as lightning discharges (Figure 3.1b) which are concentrated in the tropics produce electromagnetic (EM) waves with frequencies higher than 1 Hz, with which we can probe the shallow part of the subsurface. This high frequency signal propagates around the world as guided waves between the earth and the ionosphere.

The electromagnetic field variations with frequencies lower than 1 Hz, called micro-pulsations are produced by the complex interactions between the charged particles in the solar wind and the earth´s magnetosphere and charged particles in the ionosphere. This can vary in magnitude on a daily, weekly, and yearly basis. These EM-field variations are used for deeper crustal investigations. The solar wind is a continuous stream of plasma that carries a weak magnetic field. The pressure of the solar wind onto the magnetosphere causes compressions on the sun side and a tail on the night side (Figure 3.1a). The natural electromagnetic fluctuations have a low magnitude for frequencies between about 0.1 Hz and 10 Hz in the so-called dead band. MT measurements in this frequency range usually suffer from bad data quality.
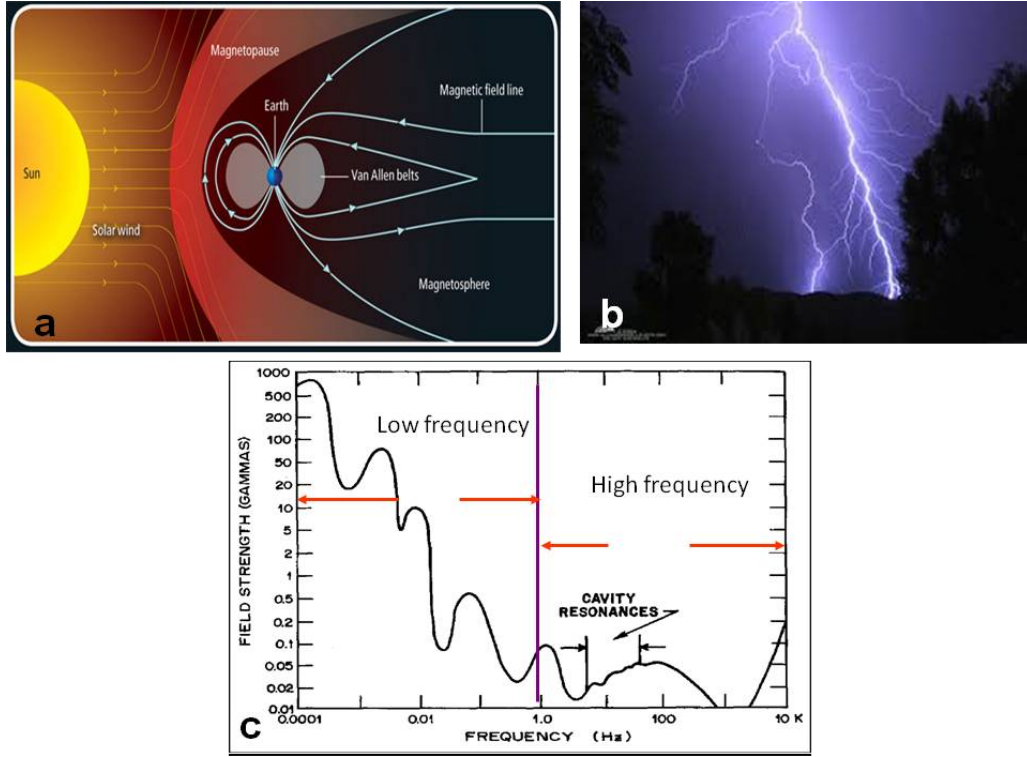
Figure 3.1. Source of EM field. (a) interaction of solar wind with magnetosphere (b) lighting discharges and (c) natural magnetic field spectrum.

3.1.2 Basic Electromagnetic Theory and Governing Equations

The basic theory of the MT method relies on Maxwell's equations:

$$\nabla \times \boldsymbol{E} = -\frac{\partial \boldsymbol{B}}{\partial t}, \qquad \text{Faraday´s law} \qquad 3.1a$$

$$\nabla \times \boldsymbol{H} = \boldsymbol{j} + \frac{\partial \boldsymbol{D}}{\partial t}, \qquad \text{Ampère´s law} \qquad 3.1b$$

$$\nabla \cdot \boldsymbol{B} = 0 \qquad \text{Gauss´s law (no isolated magnetic charge)} \qquad 3.1c$$

$$\nabla \cdot \boldsymbol{D} = \eta, \qquad \text{Gauss´s law} \qquad 3.1d$$

where **E** (*V/m*) is the electric field intensity, **H** (*A/m*) is the magnetic field intensity, **B** (*T*) is the magnetic induction, **D** (*C/m²*) is the electric displacement, η (*C/m³*) is the electric charge density of free charges and **j** (*A/m²*) is the electric current density.

For linear and isotropic media, the vector fields in Maxwell´s equations can be related through constitutive relationships as follows:

$$\boldsymbol{j} = \sigma \boldsymbol{E} \qquad 3.2a$$
$$\boldsymbol{D} = \varepsilon \boldsymbol{E} \qquad 3.2b$$
$$\boldsymbol{B} = \mu \boldsymbol{H} \qquad 3.2c$$

9

Where σ (S/m) is the electrical conductivity (the reciprocal of the electrical resistivity, ρ), ε = $\varepsilon_r\varepsilon_o$ (F/m) is the dielectric permittivity and μ = $\mu_r\mu_o$ (H/m) is the magnetic permeability. σ, ε and μ describe intrinsic properties of the materials through which the electromagnetic fields propagate.

3.1.3 The Electromagnetic Field in conductive media

For homogeneous and isotropic conductive media, Faraday´s law and Ampère´s law in Maxwell´s equations 3.1a and 3.1b can be rewritten using their constitutive equations (3.2a, b, and c) as:

$$\nabla \times \boldsymbol{E} = -\mu\frac{\partial \boldsymbol{H}}{\partial t} \qquad\qquad 3.3a$$

$$\nabla \times \boldsymbol{H} = \sigma\boldsymbol{E} + \varepsilon\frac{\partial \boldsymbol{E}}{\partial t} \qquad\qquad 3.3b$$

Assuming time dependency of the electromagnetic fields **H**, **E** as $\sim e^{i\omega t}$ where ω = 2πf (angular frequency), i $= \sqrt{-1}$, f = 1/T (frequency) and T is period, equations 3.3a and 3.3b give:

$$\nabla \times \boldsymbol{E} = -i\mu\omega\boldsymbol{H} \qquad\qquad 3.4a$$

$$\nabla \times \boldsymbol{H} = (\sigma + \varepsilon i\omega)\boldsymbol{E} \qquad\qquad 3.4b$$

Taking the curl of equation 3.3a and substituting equation 3.3b we get:

$$\nabla \times \nabla \times \boldsymbol{E} = -\mu\frac{\partial}{\partial t}(\nabla \times \boldsymbol{H}) = -\mu\sigma\frac{\partial}{\partial t}\boldsymbol{E} - \varepsilon\mu\frac{\partial^2 \boldsymbol{E}}{\partial t^2} \qquad\qquad 3.5$$

In a homogeneous conductive medium no charges are accumulated and the charge density η in equation (3.1d) is zero. Therefore 3.1d using 3.2b becomes:

$$\nabla \cdot \boldsymbol{E} = 0 \qquad\qquad 3.6$$

Using this and the vector identity definition

$$\nabla \times \nabla \times \boldsymbol{A} = \nabla(\nabla \cdot \boldsymbol{A}) - \nabla^2\boldsymbol{A} \qquad\qquad 3.7$$

equation (3.5) becomes:

$$\nabla^2\boldsymbol{E} = \mu\sigma\frac{\partial}{\partial t}\boldsymbol{E} + \varepsilon\mu\frac{\partial^2 \boldsymbol{E}}{\partial t^2} \qquad\qquad 3.8a$$

Following the same procedure (i.e. taking the curl of equation 3.3b and substituting equation 3.3a) we get a similar equation for **H** as:

$$\nabla^2 \boldsymbol{H} = \mu\sigma \frac{\partial H}{\partial t} + \varepsilon\mu \frac{\partial^2 H}{\partial t^2} \qquad\qquad 3.8b$$

These are equations that describe the behaviour of the electromagnetic field propagation in a homogeneous media. In a non-conductive medium, where σ = 0, equations 3.8a and 3.8b become wave equations:

$$\nabla^2 \boldsymbol{E} = \varepsilon\mu \frac{\partial^2 E}{\partial t^2} \ ; \ \nabla^2 \boldsymbol{H} = \varepsilon\mu \frac{\partial^2 H}{\partial t^2} \qquad\qquad 3.9$$

Describing the propagation of electromagnetic waves of velocity $v = (\sqrt{\varepsilon\mu})^{-1}$ and still assuming the time dependency of the electromagnetic fields as $\sim e^{i\omega t}$, equations 3.8a and 3.8b become:

$$\nabla^2 \boldsymbol{E} = (i\omega\mu\sigma - \omega^2\mu\varepsilon)\boldsymbol{E} \qquad\qquad 3.10a$$

and

$$\nabla^2 \boldsymbol{H} = (i\omega\mu\sigma - \omega^2\mu\varepsilon)\boldsymbol{H} \qquad\qquad 3.10b$$

by defining the wave number k:

$$k^2 = (i\omega\mu\sigma - \omega^2\varepsilon\mu) \qquad\qquad 3.11$$

equations 3.10a and 3.10b become Helmholtz equations:

$$\nabla^2 \boldsymbol{E} = k^2\boldsymbol{E} \ ; \ \nabla^2 \boldsymbol{H} = k^2\boldsymbol{H} \qquad\qquad 3.12$$

The absolute permeability, μ, is given by $\mu = \mu_r \mu_0$, where μ_r is relative permeability, μ_0 is permeability of free-space; and the electric permittivity, ε, is given by $\varepsilon = \varepsilon_r \varepsilon_0$, where ε_r is relative permittivity, ε_0 is permittivity of free-space. In the Earth, we usually have $\mu_r \simeq 1$ and magnetic permeability, μ, of rocks are assumed to be equal to the free-space value ($\mu_0 = 4\pi \times 10^{-7}$ H/m). The resistivity of subsurface rocks is usually in the range of ρ ≈ 1-10^4 Ωm (or σ ≈ 1-10^{-4}) and the frequency used in MT measurement is in the range of 10^{-4}-10^4 Hz. Taking the permittivity of free-space, $\varepsilon_0 = 8.85 \times 10^{-12}$ F/m and the relative dielectric permittivity in the range 1-100, the maximum value of the product $\omega \varepsilon$ in equation 3.11 is:

$(\omega\varepsilon)_{max} = 2\pi f \varepsilon_0 \varepsilon_r = 2\pi \cdot 10^4 \cdot 8.85 \times 10^{-12} \cdot 100 \approx 5 \cdot 10^{-5}$

Thus for σ > 10^{-4}, σ >> ωε; the propagation constant k reduces to:

$$k \simeq \sqrt{i\omega\mu\sigma} \qquad\qquad 3.13$$

which is called the quasi-static approximation. using this approximation, equations 3.10a and 3.10b reduce to:

$$\nabla^2 \boldsymbol{E} = i\omega\mu\sigma\boldsymbol{E} \qquad\qquad 3.14a$$

$$\nabla^2 \boldsymbol{H} = i\omega\mu\sigma\boldsymbol{H} \qquad\qquad 3.14b$$

Consider the plain electromagnetic wave of angular frequency ω and wave vector $\mathbf{k}_0$ incident at the surface of a homogeneous earth with resistivity $\rho=1/\sigma$ (Figure 3.2). The wave vector $\mathbf{k}_0$ makes the angle θ_i (angle of incident) with the z-axis. The refracted wave propagates into the half-space with wave vector $\mathbf{k}$ making the angle θ_t with the z-axis. Therefore, we have according to Snell´s law:
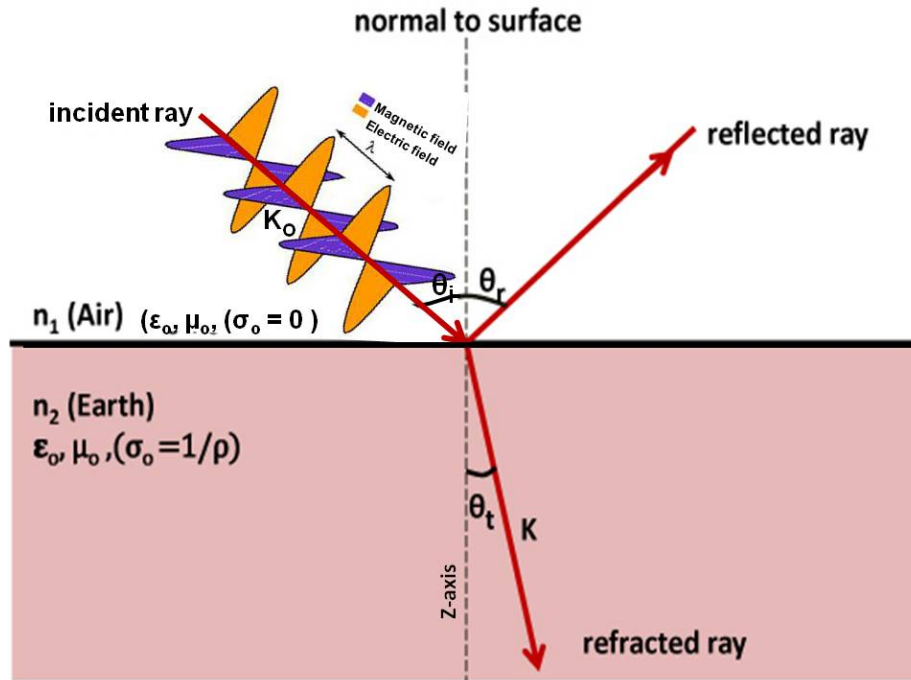
Figure 3.2. Snell's law. Refraction of EM field incident on the earth´s surface.

$$\frac{1}{v_0}\sin\theta_i = \frac{1}{v}\sin\theta_t \qquad\qquad 3.15$$

where v_0 and v are the velocities in the air and the half-space (from the phase velocity formula in eq. 3.33), respectively:

$$v_0 = \frac{1}{\sqrt{\varepsilon\mu}}; v = \sqrt{\frac{2\omega}{\mu\sigma}} \qquad\qquad 3.16$$

Then substituting v_0 and v from equation 3.16 into equation 3.15 and re-arranging we get:

$$\sin\theta_t = \sin\theta_i\sqrt{\frac{2\varepsilon\omega}{\sigma}} \qquad\qquad 3.17$$

Assuming that the resistivity of ground rocks, $\rho=1/\sigma < 10^4$ Ωm and the frequency less than 10^3 Hz ($\omega < 10^3$ Hz), then

$$\frac{2\varepsilon\omega}{\sigma} < 10^{-3}$$

As a result of this small number, θ_t is practically zero and the refracted wave in the earth has the wave vector **k** along the z-axis for all angles of incidence, θ_i.

Let us take a coordinate system with x, y and z axes pointing north, east and vertically downwards, respectively. From the assumption of a plane wave source field, when the wave is propagating along the +z direction (a vertically uniformly incident plane wave), there is no variation of electric and magnetic vectors with respect to x or y, i.e. $\partial/\partial x = \partial/\partial y = 0$. Therefore, in the coordinate system, equation (3.12) for the electric vector in the north and east directions and magnetic vector in the east direction can be rewritten as:

$$\frac{\partial^2 E_{x,y}}{\partial z^2} = k^2 E_{x,y} \qquad\qquad 3.18$$

$$\frac{\partial^2 H_y}{\partial z^2} = k^2 H_y \qquad\qquad 3.19$$

These equations (3.18 and 3.19) are ordinary differential equations and if we consider the electric field in the x-y direction ($E_{x,y}$) then equation 3.18 has the following general solution:

$$E_{x,y}(z,\omega) = A_{x,y}e^{kz} + B_{x,y}e^{-kz} \qquad\qquad 3.20$$

If we include the time factor exp(iωt), we obtain:

$$E_{x,y}(z,t) = A_{x,y}e^{(kz+i\omega t)} + B_{x,y}e^{-(kz-i\omega t)} \qquad\qquad 3.21$$

where A and B are constants, which are evaluated by applying boundary conditions. The first term in equation 3.21 represents the wave propagation in the negative z-direction and the second term in the positive z-direction. Since we are considering a homogeneous earth, $E_{x,y}$ vanishes as z → ∞. This condition leads us to have A = 0 so that equation 3.21 becomes:

$$E_{x,y}(z) = B_{x,y}e^{-(kz-i\omega t)} \qquad\qquad 3.22$$

For a plane electromagnetic wave, Faraday's law in equation 3.4a can be rewritten using the determinant presentation as:

$$\nabla \times \boldsymbol{E} = \begin{vmatrix} \boldsymbol{a}_x & \boldsymbol{a}_y & \boldsymbol{a}_z \\ \frac{\partial}{\partial x} & \frac{\partial}{\partial y} & \frac{\partial}{\partial z} \\ \boldsymbol{E}_x & \boldsymbol{E}_y & 0 \end{vmatrix} = -i\mu\omega(H_x\boldsymbol{a}_x + H_y\,\boldsymbol{a}_y) \qquad\qquad 3.23$$

where $\boldsymbol{a}_x$, $\boldsymbol{a}_y$, $\boldsymbol{a}_z$ are unit vectors along the directions of a set of Cartesian coordinates. This can be expanded as:

$$\left(0 - \frac{\partial E_y}{\partial z}\right)\boldsymbol{a}_x - \left(0 - \frac{\partial E_x}{\partial z}\right)\boldsymbol{a}_y + \left(\frac{\partial E_y}{\partial x} - \frac{\partial E_x}{\partial y}\right)\boldsymbol{a}_z = -i\mu\omega(H_x\boldsymbol{a}_x + H_y\,\boldsymbol{a}_y) \qquad 3.24$$

Because there is no variation of electric and magnetic vectors with respect to x or y, i.e. $\partial/\partial x = \partial/\partial y = 0$, equation 3.24 gives:

$$H_x = \frac{1}{i\mu\omega}\frac{\partial E_y}{\partial z} \qquad\qquad 3.25$$

$$H_y = -\frac{1}{i\mu\omega}\frac{\partial E_x}{\partial z} \qquad\qquad 3.26$$

Differentiating equation 3.22 with respect to z and with appropriate substitution into equations 3.25 and 3.26, we get the general solution to magnetic field in x and y-directions:

$$H_x(z) = -\frac{k}{i\omega\mu}\{B_y e^{-(kz - i\omega t)}\} \qquad\qquad 3.27$$

$$H_y(z) = \frac{k}{i\omega\mu}\{B_x e^{-(kz - i\omega t)}\} \qquad\qquad 3.28$$

The above derivations show that the **E** and **H** fields are orthogonal. For the homogeneous half-space, with conductivity σ and a normally incident plane wave, the orthogonal **E** and **H** fields are constant in direction and magnitude over planes perpendicular to the vertical, downward +z, direction of propagation.

The wave number, k, in equation 3.13 can be rewritten as:

$$k = \sqrt{i\omega\mu\sigma} = (1+i)\sqrt{\frac{\omega\mu\sigma}{2}} \qquad\qquad 3.29$$

Note that $(\sqrt{i} = \sqrt{2i/2} = \sqrt{(1 + 2i - 1)/2} = \sqrt{(1+i)^2/2} = (1+i)/\sqrt{2}$

Thus, k has a real and imaginary part. The real part is associated with the attenuation and the imaginary part is associated with the phase. Substituting the value of k from equation (3.29) into (3.22), the exponential of **E** and **H** can be expressed as:

$$e^{-\left(\left(\sqrt{\frac{\omega\mu\sigma}{2}} + i\sqrt{\frac{\omega\mu\sigma}{2}}\right)z - i\omega t\right)} = e^{-\sqrt{\frac{\omega\mu\sigma}{2}}z}e^{-i\sqrt{\frac{\omega\mu\sigma}{2}}z}e^{i\omega t} \qquad\qquad 3.30$$

In (3.30) the magnitude is given by exp $\left(-\sqrt{\frac{\omega\mu\sigma}{2}}z\right)$ and the phase factor by exp $\left(-i\sqrt{\frac{\omega\mu\sigma}{2}}z\right)$. The field attenuates exponentially and is retarded linearly in phase with increasing z.

3.1.4 Depth of Penetration

Continuing the discussion of the preceding section, we can now obtain a quantitative measure of the penetration depth of the wave in the conductive medium. Consider the wave that penetrates the conductive medium, i.e. the transmitted wave. Let z = 0 at the boundary of the conductive medium, so that z increases positively into the conductive medium. Equation 3.30 can be written in the form:

$$e^{-z/\delta}e^{-i\,(z/\delta)}e^{i\omega t} \hspace{5cm} 3.31$$

where $\delta = \sqrt{\dfrac{2}{\omega\mu\sigma}}$, has the dimension of a distance. At z = δ, the amplitude of the electric field has decreased by a factor of e^{-1}. Thus E_x decreases to 1/e (36.8%) of its initial value, while the wave penetrates to a distance δ. δ is called skin depth.

It can be seen that the amplitude decreases for higher conductivities and frequencies. Using that $\mu = \mu_0 = 1.2566 \times 10^{-6}$ H/m (in the earth, we have $\mu_r = 1$) and $\omega = 2\pi/T$, where T is the period of the field, we have:

$$\delta \approx 500\sqrt{\rho T} \quad [m] \hspace{5cm} 3.32$$

For a given resistivity distribution of the subsurface, the depth of penetration increases with increasing period. For a fixed period, the skin depth increases with increasing resistivity of the subsurface.

Phase velocity is given by the ratio ω/β. We have β = 1/δ, so that the phase velocity or the velocity of the propagating wave in the medium is:

$$v = \omega\delta = \sqrt{\dfrac{2\omega}{\sigma\mu}} \hspace{5cm} 3.33$$

3.2 Homogeneous Earth

Cagniard (1953), Keller and Frischknecht (1966) provide an excellent introduction to the theory of magnetotelluric fields for a plane layered earth, where each layer is homogeneous and isotropic. In such a medium an electromagnetic wave propagates so that the electric and magnetic field vectors are orthogonal, and the ratio of electric to magnetic field intensity (E$_x$/H$_y$) is a characteristic measure of the electromagnetic properties often called the characteristic impedance denoted by Z. It has the dimensions of resistance and combining equations 3.22 with 3.27 and 3.28, it can be written as:

$$Z = \dfrac{E_x}{H_y} = \dfrac{i\omega\mu}{k} = -\dfrac{E_y}{H_x} \hspace{4cm} 3.34$$

The impedance, Z, using the wave propagation constant, k for the quasi-static approximation, from equation 3.13 (k $=\sqrt{i\omega\mu\sigma}$) and equation 3.34 can be rewritten as:

$$Z = \dfrac{i\omega\mu}{\sqrt{i\mu\sigma\omega}} = \sqrt{i}\,\sqrt{\omega\mu\rho} = \sqrt{\omega\mu\rho}\;e^{i\pi/4}, \hspace{3cm} 3.35$$

This represents the Cagniard impedance and $\pi/4$ is the phase difference between E_x and H_y. If the earth is homogeneous and isotropic, then the true resistivity is related to the characteristic impedance using equation 3.35 through the relation:

$$\rho = \frac{1}{\omega\mu}|Z|^2 \qquad\qquad 3.36$$

This can be formulated using the magnetic field intensity **B**, which is related by the constitutive relationship in equation 3.2c, $B = \mu H$, where $\mu = 4\pi \times 10^{-7}$ H/m. The practical units for electric field, **E** is mV/km and for **B**, practical unit is nT (or 10^{-9} Tesla = 1 gamma). Therefore, using the practical units, equation 3.36 can be expressed as:

$$\rho = \frac{T}{2\pi\mu}\left|\frac{E_x 10^{-6}\mu}{B_y 10^{-9}}\right|^2 = \frac{T\mu}{2\pi}\left|\frac{E_x}{B_y}\right|10^6$$

or

$$\rho = 0.2T|Z|^2 = 0.2T\left|\frac{E_x}{B_y}\right|^2, \quad \text{and the phase is given as, } \phi = arg(Z) = \frac{\pi}{4} = 45° \quad 3.37$$

For a homogeneous earth, ρ and   are independent of T. For a non-homogeneous earth, these depend on T and we define apparent resistivity (ρ_a) and phase (ϕ_a) as:

$$\rho_a(T) = 0.2T|Z_0|^2 = 0.2T\left|\frac{E_x}{B_y}\right|^2, \text{and the phase, } \phi_a(T) = arg(Z_0) \neq 45° \qquad 3.38$$

where Z_0 = impedance at the surface

3.3 Layered earth

On the surface of a horizontally N-layered earth (Figure 3.3), the plane wave impedance is given by the recursive formula (Ward and Wannamaker, 1983) as:

$$\hat{Z}_N = Z_N = \frac{i\omega\mu_0}{k_N} \qquad\qquad \hat{Z}_{n-1} = Z_{n-1}\frac{\hat{Z}_n + Z_{n-1}\tanh(ik_{n-1}h_{n-1})}{Z_{n-1} + \hat{Z}_n\tanh(ik_{n-1}h_{n-1})} \qquad 3.39$$

where $Z_n = \frac{i\omega\mu_0}{k_n}$ is the intrinsic impedance of the nth layer, $k_n = \sqrt{(i\omega\mu_0\sigma_n)}$ and h_n is thickness of the nth layer; $\hat{Z}_n$ is impedance at the top of the nth layer and $\hat{Z}_1 = Z_0$ is the impedance at the surface.
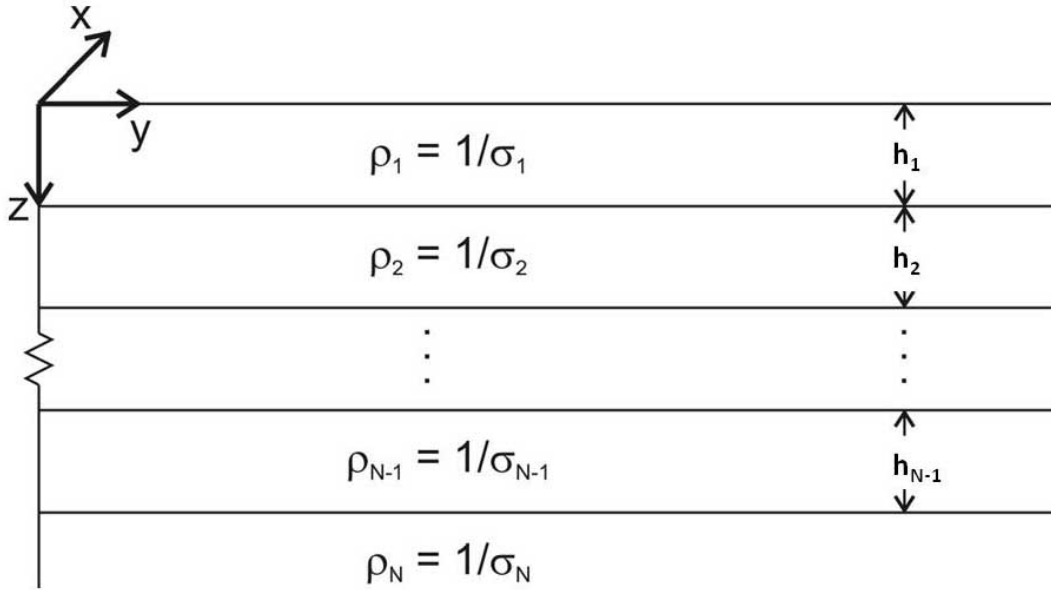
Figure 3.3. An N-layered half space earth model.

If we consider a two layered earth model of ρ_1 and ρ_2, equation 3.39 becomes:

$$Z_0 = \hat{Z}_1 = Z_1 \frac{\hat{Z}_2 + Z_1 \tanh(ik_1 h_1)}{Z_1 + \hat{Z}_2 \tanh(ik_1 h_1)}; \text{where } k_1 = \sqrt{(i\omega\mu_0/\rho_1)} = \sqrt{\frac{i2\pi\mu_0}{\rho_1 T}} \qquad 3.40$$

For large periods (T), $k_1 h \ll 1$, we have $\tanh(ik_1 h_1) \approx ik_1 h_1$ and since $\hat{Z}_2 = Z_2$ equation 3.40 can be rewritten as:

$$Z_0 = Z_1 \left[\frac{Z_2 + iZ_1 k_1 h_1}{Z_1 + iZ_2 k_1 h_1}\right] \qquad 3.41$$

For $\rho_1 \gg \rho_2$, that means we have a conductor at depth h_1 and $Z_1 \gg Z_2$. Then Equation 3.41 becomes:

$$Z_0 = Z_1 \left[\frac{Z_2 + iZ_1 k_1 h_1}{Z_1 + iZ_2 k_1 h_1}\right] \approx iZ_1 k_1 h_1 = \frac{i\omega\mu_0}{k_1} k_1 h_1 = -\omega\mu_0 h_1, \qquad 3.42$$

and $\quad \rho_a = \frac{1}{\omega\mu_0}|Z_0|^2 = \frac{1}{\omega\mu_0}|-\omega\mu_0 h_1|^2 = \frac{2\pi\mu_0 h_1^2}{T} \qquad 3.43$

Therefore the depth to the good conductor, h_1, can be calculated from ρ_a at longer periods, T, as:

$$h_1 = \sqrt{\frac{\rho_a T}{2\pi\mu_0}} \qquad 3.44$$

On $\log_{10}\rho_a$ vs. $\log_{10} T$ plots, equation 3.43 is a straight line with slope, -45, that is, $\log_{10}\rho_a = \log_{10}(2\pi\mu_0 h_1^2) - \log_{10} T$. These asymptotic descending lines are called "h lines" (Berdichevsky and Dmitriev, 1976).

For $\rho_1 \ll \rho_2$, that means we have an insulator at depth h_1 and $Z_1 \ll Z_2$ then equation 3.41 becomes:

$$Z_0 = Z_1 \left[\frac{Z_2 + iZ_1 k_1 h_1}{Z_1 + iZ_2 k_1 h_1} \right] \approx Z_1 \frac{1}{ik_1 h_1} = \frac{\omega \mu_0}{k_1^2} \frac{1}{h_1} = -\frac{i}{\sigma_1 h_1} = -\frac{i}{S} \qquad 3.45$$

where $S = \sigma_1 h_1$ is the conductance of the layer 1 and

$$\rho_a = \frac{1}{\omega \mu} |Z_0|^2 = \frac{1}{\omega \mu_0} \frac{1}{S^2} = \frac{T}{2\pi \mu_0} \frac{1}{S^2} \qquad 3.46$$

Therefore the conductance of layer 1 can be calculated from ρ_a at longer periods, T, as:

$$S = \sqrt{\frac{T}{2\pi \mu_0 \rho_a}} \qquad 3.47$$

On $\log_{10} \rho_a$ vs. $\log_{10} T$ plots, equation 3.46 is a straight line with slope, $+45°$, that is, $\log_{10} \rho_a = \log_{10} T - \log_{10}(2\pi \mu_0 S^2)$. These asymptotic ascending lines are called "S lines".

This means that if the slope of the ρ_a curve is not between -1 and +1 (between -45° and +45°), something is wrong with the data.

3.4 Magnetotelluric Transfer functions

Magnetotelluric transfer functions or MT responses are functions that relate the registered electromagnetic field components at a given frequencies. These functions depend only on the electrical properties of the material and frequency not on the electromagnetic sources as long as the source fields can be taken as plane waves. Hence, they characterize the resistivity distribution of the underlying materials according to the measured frequency.

The magnetotelluric transfer functions which are briefly discussed in the following subsections are the Impedance Tensors and the Geomagnetic Transfer functions.

3.4.1 Impedance tensor

The impedance tensor describes the relation between the orthogonal electric and magnetic fields of a given frequency. In matrix form this is given by

$$\begin{pmatrix} E_x \\ E_y \end{pmatrix} = \begin{pmatrix} Z_{xx} & Z_{xy} \\ Z_{yx} & Z_{yy} \end{pmatrix} \begin{pmatrix} H_x \\ H_y \end{pmatrix} \qquad 3.48$$

Or the electric and magnetic field spectra are linearly related as:

$$\left. \begin{array}{l} E_x(\omega) = Z_{xx}(\omega) H_x(\omega) + Z_{xy}(\omega) H_y(\omega) \\ E_y(\omega) = Z_{yx}(\omega) H_x(\omega) + Z_{yy}(\omega) H_y(\omega) \end{array} \right\} \qquad 3.49$$

$$\boldsymbol{E} = \hat{\boldsymbol{Z}} \boldsymbol{H} \text{ or } \boldsymbol{H} = \hat{Z}^{-1} \boldsymbol{E} = \hat{Y} \boldsymbol{E}$$

where Z_{xy} and Z_{yx} are called the principal impedances while Z_{xx} and Z_{yy} the supplementary ones (contributions from parallel components of the electric and magnetic field), $\hat{Y}$ is the admittance which is the inverse of the impedance tensor $\hat{Z}$.

3.4.2 Geomagnetic transfer functions

The geomagnetic transfer function, also known as the tipper vector or Tipper, $\mathcal{T}$ is a dimensionless complex vector showing the relationship between the vertical and the two horizontal components of the magnetic field, i.e.

$$H_z(\omega) = \mathcal{T}_{zx}H_x(\omega) + \mathcal{T}_{zy}H_y(\omega) \tag{3.50}$$

For a homogeneous or 1D Earth, there is no induced vertical magnetic field H_z, and hence the transfer functions ($\mathcal{T}_{zx}$, $\mathcal{T}_{zy}$) are zero. By contrast, close to a vertical boundary between low and high conductivity structures (for example, at the boundary between ocean and land), there is an induced H_z field.

The tipper vector can be decomposed into two real vectors in the horizontal xy plane. These real vectors are called inductions arrows. They are used to infer the presence of lateral variations in conductivity.

There exist two representations of the real induction arrows which we call reversed (Parkinson convention, Parkinson, 1959) or non-reversed (Schmucker or Wiese convention). In the *Wiese convention*, the vectors point *away* from lateral increase in electrical conductivity (Wiese, 1962). The arrows have a real (in-phase) and quadrature (out-of-phase) part. Length of the real (M_r) and quadrature (M_q) arrows are given by:

$$M_r = \left(\Re\mathcal{T}_{zx}{}^2 + \Re\mathcal{T}_{zy}{}^2\right)^{1/2} \tag{3.51a}$$
$$M_q = (\Im\mathcal{T}_{zx}{}^2 + \Im\mathcal{T}_{zy}{}^2)^{1/2} \tag{3.51b}$$

Where $\Re$ and $\Im$ are the real and imaginary parts of tipper, respectively.

Orientation of the arrows, clockwise positive from x-direction (usually geomagnetic north), is similarly determined by:

$$\alpha_r = \tan^{-1}\left(\frac{\Re\mathcal{T}_{zy}}{\Re\mathcal{T}_{zx}}\right) \tag{3.52a}$$

$$\alpha_q = \tan^{-1}\left(\frac{\Im\mathcal{T}_{zy}}{\Im\mathcal{T}_{zx}}\right) \tag{3.52b}$$

3.5 Dimensionality of MT transfer functions

The MT transfer functions, Z, and particularly the relationship between their components, is reduced to specific expressions depending on the spatial distribution of the electrical conductivity being imaged. These spatial distributions, known as geo-electric dimensionality, can be classified as 1D, 2D or 3D.

3.5.1 1D earth case

For 1D Earth, the conductivity distribution varies only with depth; as a result the MT transfer functions are independent of the orientation of the measured axes. The diagonal elements of the impedance tensor Z_{xx} and Z_{yy} are zero and the off-diagonal elements Z_{xy} and Z_{yx} are equal in magnitude but opposite in sign (see equation 3.34).

The impedance tensor in equation 3.48 can be presented here as:

$$Z_{1D} = \begin{pmatrix} 0 & Z_{xy} \\ -Z_{xy} & 0 \end{pmatrix} \qquad\qquad 3.53$$

And the corresponding apparent resistivity and phase are defined as:

$$\rho_a = \frac{1}{\mu\omega}|Z|^2 \text{ and } \phi_a = tan^{-1}\left(\frac{Im\ Z}{Re\ Z}\right) \qquad\qquad 3.54$$

3.5.2 2D earth case

For a 2D earth, conductivity is constant along one horizontal direction but varies in the other horizontal direction and with depth. The diagonal elements of the impedance tensor Z_{xx} and Z_{yy} are now equal in magnitude but opposite in sign, while the off-diagonal elements Z_{xy} and Z_{yx} differ, i.e.:

$$\left.\begin{matrix} Z_{xx} = -Z_{yy} \\ Z_{xy} \neq -Z_{yx} \end{matrix}\right\} 2D$$

The direction along which the conductivity is constant is known as the geoelectrical strike or electromagnetic strike. We can show that if the x- and y-directions are parallel and perpendicular to the strike, respectively, the diagonal elements of the impedance tensor Z_{xx} and Z_{yy} are again zero, and the impedance tensor can thus be represented as:

$$Z_{2D} = \begin{pmatrix} 0 & Z_{xy} \\ Z_{yx} & 0 \end{pmatrix} \qquad\qquad 3.55$$

where $Z_{xy} = Z_{TE} = \frac{E_x}{H_y}$ and $Z_{yx} = Z_{TM} = \frac{E_y}{H_x}$

For 2D electrical resistivity structure (Figure 3.4), Maxwell's equations separate (decouple) into two modes. In one mode, electric field parallel to the electric strike depends only on magnetic field components perpendicular to the strike (**E**-polarization, referred to as Transverse Electric (TE) mode) and in the other mode, electric field perpendicular to strike depends only on magnetic fields parallel to the electric strike (**B**-polarization, referred to as Transverse Magnetic (TM) mode).

The **E**-polarization in terms of the electromagnetic field components E_x, B_y and B_z from equation 3.1a is given as:

$$
\left.\begin{array}{l}
\dfrac{\partial E_x}{\partial y} = \dfrac{\partial B_z}{\partial t} = i\omega B_z \\[2mm]
\dfrac{\partial E_x}{\partial z} = \dfrac{\partial B_y}{\partial t} = -i\omega B_y \\[2mm]
\dfrac{\partial B_z}{\partial y} - \dfrac{\partial B_y}{\partial z} = \mu\sigma E_x
\end{array}\right\} \; \boldsymbol{E-polarization}
\qquad 3.56
$$

The **B**-polarization in terms of electromagnetic field components can also be described as:

$$
\left.\begin{array}{l}
\dfrac{\partial B_x}{\partial y} = -\mu\sigma E_z \\[2mm]
\dfrac{\partial B_x}{\partial z} = \mu\sigma E_y \\[2mm]
\dfrac{\partial E_z}{\partial y} - \dfrac{\partial E_y}{\partial z} = -i\omega B_x
\end{array}\right\} \; \boldsymbol{B-polarization}
\qquad 3.57
$$
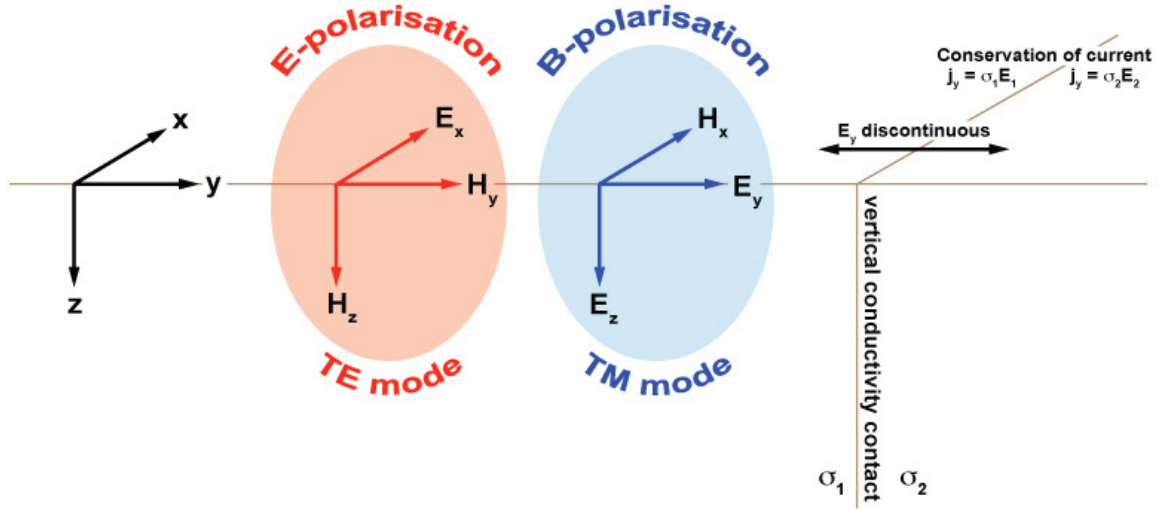
Figure 3.4. Simple 2D model and the concept of polarizations in magnetotellurics.

Figure 3.4 shows a simple 2D model composed of quarter-spaces with two zones of different conductivities, σ_1 and σ_2, on each side of an infinite planar boundary in the strike direction (the x-direction). The current density (j_y) across the boundary is given by:

$$ j_y = \sigma E_y \qquad\qquad 3.58 $$

Conservation of current across the contact, where the conductivity changes from σ_1 to σ_2 leads to y-component of the electric field (E_y) to be discontinuous. All other components of the electromagnetic field are continuous across the boundary. From equation (3.58) the magnitude of discontinuity in E_y and therefore Z_{yx} is σ_2/σ_1 and the magnitude of the corresponding apparent resistivity, ρ_{yx} perpendicular to the strike will be $(\sigma_2/\sigma_1)^2$. Figure 3.5 shows the variations of TE and TM modes across the discontinuity. In TE mode, E_x and H_z are continuous, i.e. they vary smoothly across the discontinuity. In this case, ρ_{xy} which is proportional to E_x/H_y is smoothly varying across a discontinuity. While in TM mode, H_x and E_z component are continuous across the discontinuity but E_y is discontinuous, and so ρ_{yx} which is proportional to E_y/H_x is discontinuous. As a consequence of the discontinuous behaviour exhibited by ρ_{yx}, **B**-polarization resistivities (TM-mode) tend to resolve lateral conductivity variations better than **E**-polarization resistivities (TE-mode). However, the **E**-

polarization has an associated vertical magnetic field. Vertical magnetic fields are generated by lateral conductivity gradients and boundaries, and spatial variations of the radio H_z/H_y can be used to diagnose lateral conductivity contrasts from the **E**-polarization (explained in sections 3.4.2 and 5.3).
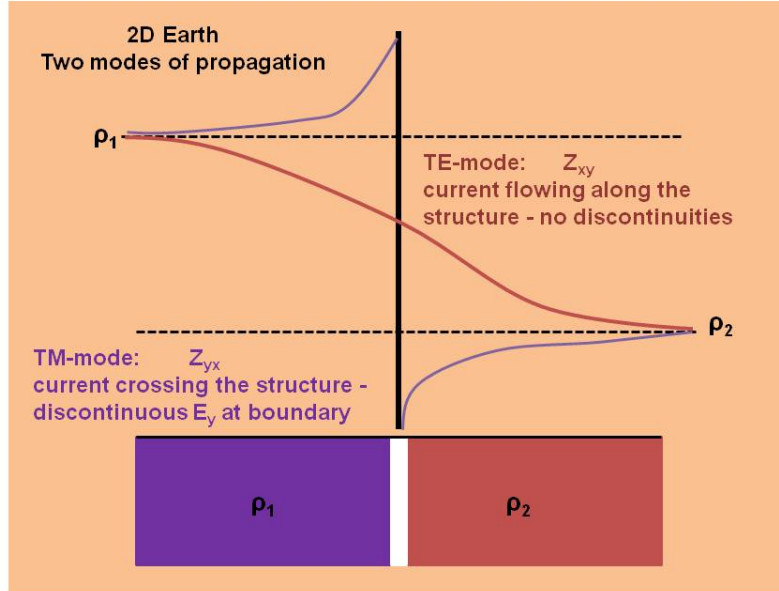
Figure 3.5. Transverse magnetic (TM) and transverse electric (TE) modes in magnetotellurics.

In the 2D Earth, measurements are in general not performed in the strike direction, because the geological structure might not be known. Consequently, the measuring axes generally don´t coincide with the axes parallel and perpendicular to geologic strike. However, it is possible to rotate the measuring axes mathematically by an angle α in the horizontal plane, so the diagonal components of the impedance tensor becomes zero and the new x´ axis is parallel to the geological strike (see the procedures of rotation in section 3.7).

3.5.3 3D earth case

This is the most general type of geo-electrical structure. Here the conductivity changes along all directions ($\sigma = \sigma(x,y,z)$), therefore, in this case Maxwell´s equations cannot be separated into two modes.

The MT transfer functions take the general form with all components non-zero. The impedance tensor in equation 3.48 is presented as:

$$Z_{3D} = \begin{pmatrix} Z_{xx} & Z_{xy} \\ Z_{yx} & Z_{yy} \end{pmatrix}$$
3.59

There is no rotational direction through which the diagonal elements of the impedance tensor or any component of the tipper vector can vanish.

3.6 Galvanic Distortion on MT Data

In MT measurements, small resistivity anomalies or heterogeneities can lead to perturbations of the **E** and **B** fields. Depending on the depth and size of the anomaly and frequency band used, the anomaly has an inductive and/or galvanic effect which adds to the MT response of the background conductivity of the medium. These heterogeneities can be much smaller than the targets of interest or are within the skin depth at the highest frequency. In the case that these heterogeneous bodies are of the same proportions as the interest depth, they can be modelled in 3D environment.

Inductive distortion is generated by current distribution, which has a small magnitude and decreases strongly with increasing period. Under the condition $\sigma >> \omega\varepsilon$ (quasi-static approximation, see section 3.1.3) inductive distortion can be ignored (Berdichevsky and Dmitriev, 1976).

Galvanic distortion is caused by charge distributions accumulated on the surface of shallow bodies, which produce anomalous electric field. This anomalous electric field can be of the same order of magnitude as the field of interest and is frequency independent (Bahr, 1988; Jiracek, 1990). Hence the galvanic distortion is treated as the existence of an anomalous electric field, $\mathbf{E}_a$.

The effects of galvanic distortion introduce an unknown multiplicative factor, independent of frequency in the apparent resistivity or constant shift on log-scale (Pellerin and Hohmann, 1990). This is known as *Static shift,* and does not affect the phase. There is no general analytical or numerical way to model the cause of static shift and thus correct it by using MT itself. Different types of correction procedures have been proposed, such as, transient EM methods (Sternberg et al*.,* 1988; Pellerin and Hohmann 1990, Árnason, 2008), laterally homogeneous layer constraints from MT data over a large region (Jones, 1988); utilization of conductivity distribution charts over the region (Demidova et al*.,* 1985), shallow resistivity soundings (Romo et al*.,* 1997), etc. The most reliable and commonly used remedy for static shift is the Transient Electromagnetic method, TEM (see section 5.4 for details of the method).

3.7 Rotation of Impedance Tensors

Even if the earth is ideally two dimensional, we usually don´t know the geoelectric strike. As a result our measuring axes generally don´t coincide with axis parallel and perpendicular to geoelectric strike. Therefore, in either anisotropic earth or inhomogeneous two dimensional structures, an attempt is always made to eliminate Z_{xx} and Z_{yy} by proper choice of coordinate systems. This leads to the determination of the strike of two dimensional structures and the nature of anisotropy in anisotropic earth. However, if the conductivity tensor is not symmetric, the diagonal elements of the impedance tensor don´t vanish. A compromise is made by trying to obtain the minimum value of the diagonal elements.

Here it is briefly described how to rotate the impedance tensor elements from the measurement axes (X-Y) to the principal anisotropy axes (X'-Y') by an angle α in a clockwise direction as shown in Figure 3.6. The impedance can be rotated through an angle α from the measurement direction to a new coordinate system according to:
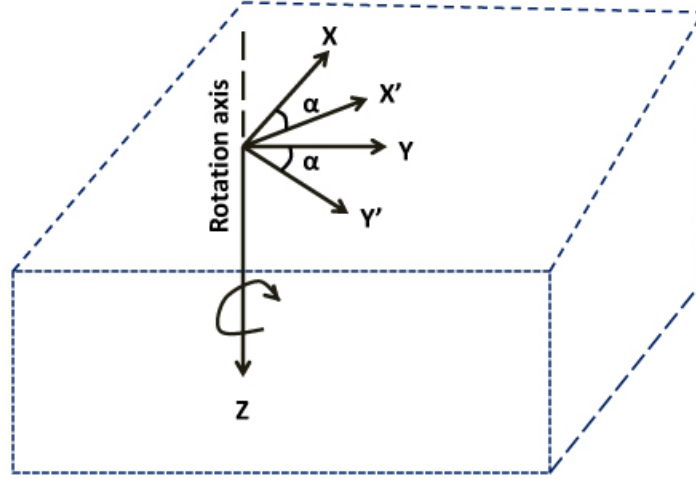
Figure 3.6. Rotation of coordinates of impedance tensor by angle α.

$$Z' = \boldsymbol{R}_\alpha Z \boldsymbol{R}_\alpha^T \qquad\qquad 3.60$$

Where $R\alpha = \begin{pmatrix} \cos\alpha & \sin\alpha \\ -\sin\alpha & \cos\alpha \end{pmatrix}$ is the rotation operator and R^T_α is the transpose of R_α (T stands for transpose), given as:

$$\boldsymbol{R}_\alpha^T = \begin{pmatrix} \cos\alpha & -\sin\alpha \\ \sin\alpha & \cos\alpha \end{pmatrix} \qquad\qquad 3.61$$

Z' in equation 3.60 can be expanded as:

$$\begin{bmatrix} Z'_{xx} & Z'_{xy} \\ Z'_{yx} & Z'_{yy} \end{bmatrix} = \begin{bmatrix} \cos\alpha & \sin\alpha \\ -\sin\alpha & \cos\alpha \end{bmatrix} \begin{bmatrix} Z_{xx} & Z_{xy} \\ Z_{yx} & Z_{yy} \end{bmatrix} \begin{bmatrix} \cos\alpha & -\sin\alpha \\ \sin\alpha & \cos\alpha \end{bmatrix} \qquad\qquad 3.62$$

Or:

$$\left.\begin{aligned} Z'_{xx} &= Z_{xx}\cos^2\alpha + (Z_{xy} + Z_{yx})\sin\alpha\cos\alpha + Z_{yy}\sin^2\alpha \\ Z'_{xy} &= Z_{xy}\cos^2\alpha + (Z_{yy} - Z_{xx})\sin\alpha\cos\alpha - Z_{yx}\sin^2\alpha \\ Z'_{yx} &= Z_{yx}\cos^2\alpha + (Z_{yy} - Z_{xx})\sin\alpha\cos\alpha - Z_{xy}\sin^2\alpha \\ Z'_{yy} &= Z_{yy}\cos^2\alpha - (Z_{xy} + Z_{yx})\sin\alpha\cos\alpha + Z_{xx}\sin^2\alpha \end{aligned}\right\} \qquad 3.63$$

In one dimensional isotropic model (Cagniard, 1953), the diagonal elements $Z_{xx} = Z_{yy} = 0$ and the off-diagonal elements, $Z_{xy} = -Z_{yx}$. Therefore, the above expression reduces to:

$$Z'_{xx} = Z'_{yy} = 0, \ Z'_{xy} = Z_{xy} \ and \ Z'_{yx} = Z_{yx}$$

and we see that the impedance tensor is independent of the measurement axis.

Sharka and Menvielle (1997) provided several independent real valued rotational invariants based on three complex magnitudes traditionally used in MT:

$$1. \text{ the trace}: S_1 = Z_{xx} + Z_{yy}$$
$$\left.2. \text{ the differnce between off} - \text{diagonal elements}: D_2 = Z_{xy} - Z_{yx}\right\} \quad 3.64$$
$$3. \text{ the determinant}: \det Z = Z_{xx}Z_{yy} - Z_{xy} Z_{yx}$$

S_1 and D_2 are two of the four modified impedances (Vozoff, 1991), each one containing two rotational real valued invariants: Re (S_1), Im (S_1) and Re (D_2), Im (D_2), respectively. Other sets of invariants can be defined as a function of these basic invariants. The rotational invariants have been and still are widely used to study particular properties of the MT tensor.

In practice, the minimum values of Z'_{xx}, Z'_{yy}, are determined for $\alpha = 0°$ to $90°$ and in other quadrants they would show repetitions. The most common approximation is based on the maximization of the off-diagonal components of the MT tensor or minimization of the diagonal ones, using the sum of the squared modules of these components (Vozoff, 1972):

$$\left(|Z'_{xx}|^2 + |Z'_{yy}|^2\right) = minimum \qquad 3.65$$

which automatically implies that:

$$\left(|Z'_{xy}|^2 + |Z'_{yx}|^2\right) = maximum \qquad 3.66$$

The resulting strike angle is known as Swift angle (Swift, 1967) and it is presented as:

$$\tan(4\alpha) = \frac{(Z_{xx}-Z_{xy})(Z_{xy}+Z_{yx})^* + (Z_{xx}+Z_{yy})^*(Z_{xy}+Z_{yx})}{|Z_{xx}-Z_{yy}|^2 - |Z_{xy}+Z_{yx}|^2} \qquad 3.67$$

where $*$ means the complex conjugate. Note that in solving equation 3.67, means that the strike angle α, has $90°$ ambiguity.

In this case, the apparent resistivity and phase relationship with rotated impedances are expressed as:

$$\rho'_{ax} = 0.2T|Z'_{xy}|^2, \phi'_{xy} = \arctan\left(\frac{ImZ'_{xy}}{ReZ'_{xy}}\right) \qquad 3.68a$$

$$\rho'_{ay} = 0.2T|Z'_{yx}|^2, \phi'_{yx} = \arctan\left(\frac{ImZ'_{yx}}{ReZ'_{yx}}\right) \qquad 3.68b$$

4 Field measurement, Instrument and Data processing

4.1 Field measurement and Instrumentation

In Alid area the MT data acquisition was done by measuring the input fields, two horizontal magnetic components H_x and H_y, two horizontal electrical fields, E_x and E_y and a vertical magnetic component, H_z (X-direction is magnetic north which is 2° east of true north). The horizontal components of the electric field were measured on the surface of the earth using two orthogonal pairs of non-polarizable porous pot electrodes containing $PbCl_2$ solution mud. E_x and E_y are determined by measuring the potential difference, ΔV, between the pairs of electrodes, which gives E = ΔV/d where d is distance of separation between the pairs of electrodes. The pods were connected to the data logger by cables. The electrode spacing was originally 50 meters, but later increased up to 125 meters in order to improve the data quality. The electrodes were buried several tens of centimetres into the ground; and bentonite used to maintain stable electrical contact with the ground.

The horizontal components and the vertical component of the magnetic field were measured on the surface of the earth by magnetic sensors (induction coils). The two horizontal magnetic coils, were buried to reduce the noise and the effect of the daily temperature changes. The vertical magnetic field, H_z was measured by putting the induction coil vertically, 90° in the ground and bury it as much as possible. The field layout is shown in Figure 4.1.
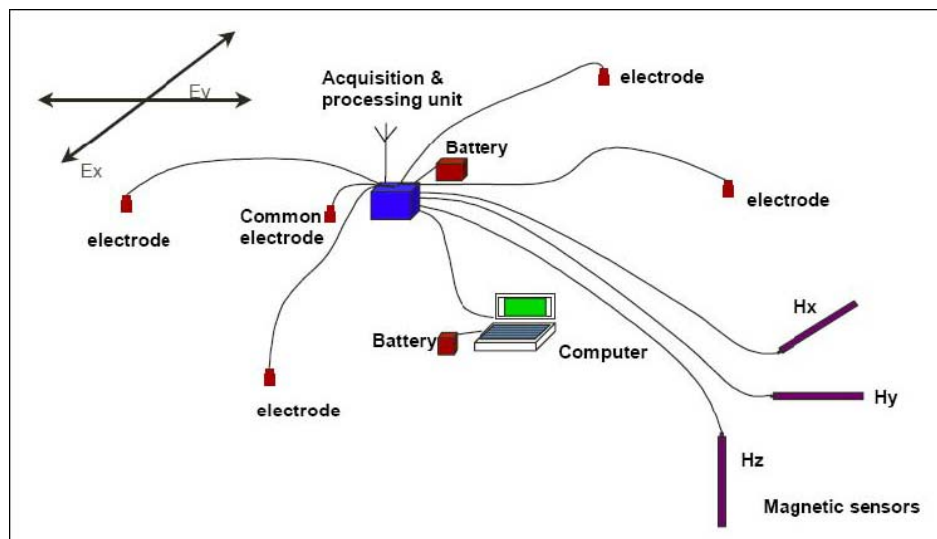
Figure 4.1. Field layout of a 5-channel MT data acquisition system (courtesy of Geosystem srl).

MT data acquisition system from Phoenix Geophysics in Canada was used for this study (Figure 4.2). The MTU data logger, which is the heart of the system, controls the data recording processes and converts the analogue signal to digital format. The MTU data

logger, through its GPS antenna is synchronized by time signal broadcasted from satellite GPS. These MTUs are light weight and can easily be carried to remote locations.

For the purpose of MT static shift correction (see section 5.4), TEM soundings were performed at each MT site. For the TEM resistivity survey, the PROTEM digital receiver and TEM-67 transmitter of Geonics Ltd. were used.

Figure 4.2. Phoenix V-5 2000 MT system (taken from http://www.phoenix-geophysics.com/home).

The MT data in this study were collected by three MT units. To increase the signal to noise ratio (see details further in section 4.2) the fourth unit was used as a remote reference stationed at about 10 km away from the nearest local site. The three units were deployed each day and picked up the next day giving approximately 16-20 hours of recording. Three of the MT units are a 5 component unit (E_x, E_y, H_x, H_y and H_z) and one is a two component unit, measuring the electric field only (E_x and E_y). The two component unit is always setup close to a nearby 5 component site (~1 km) and the magnetic field from that site is used for analyzing the result at the two component site, assuming the magnetic field is homogeneous locally. In the middle of the field work period, one of the 5 component MT unit was unable to measure the magnetic field and was used as two component unit for the rest of the survey time. A total of 52 soundings were measured in a grid fashion (the location of the MT and TEM stations is shown in Figure 4.3).
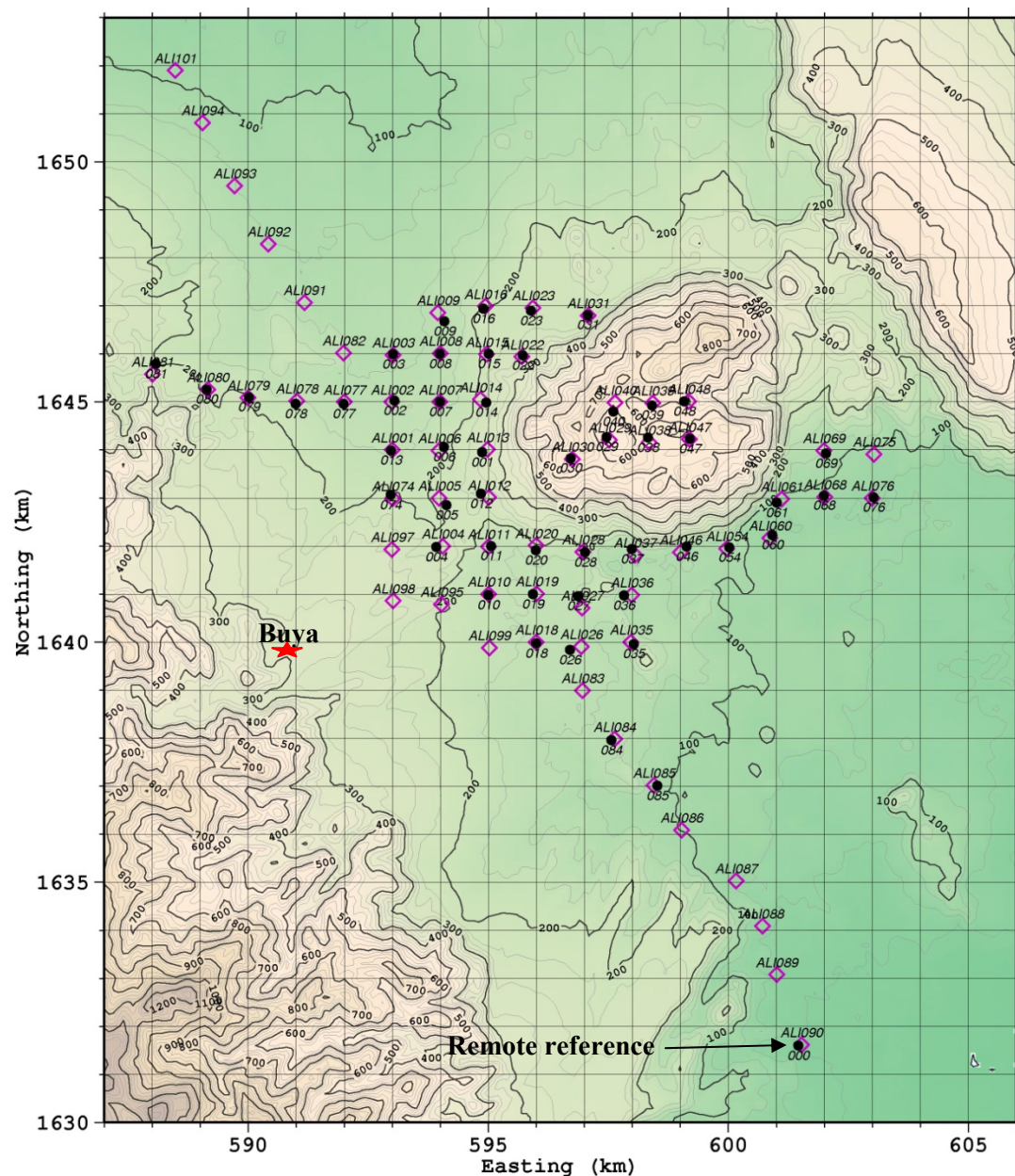
Figure 4.3. Location of MT (black dots) and TEM (purple diamond) soundings. The red star is Buya, a village where the field crew was camping.

4.2 Data processing (Time Series Processing)

The MT transfer functions are obtained from time series processing of the acquired data. The electric and magnetic field time-variations of the MT data are measured as a function of time. Time-series data were downloaded from the MTU units of each site and inspected for the quality of the data using a programme called Synchro-Time Series Viewer. This programme allows viewing and printing graphical presentations of the raw time-series data, power spectra derived from the time-series data and coherency between pairs of orthogonal electric and magnetic components. An example of time series record is shown in (Figure 4.4). The electric field in the x direction (E_x) should correlate with magnetic field in y direction (H_y), and similarly E_y correlates with H_x.
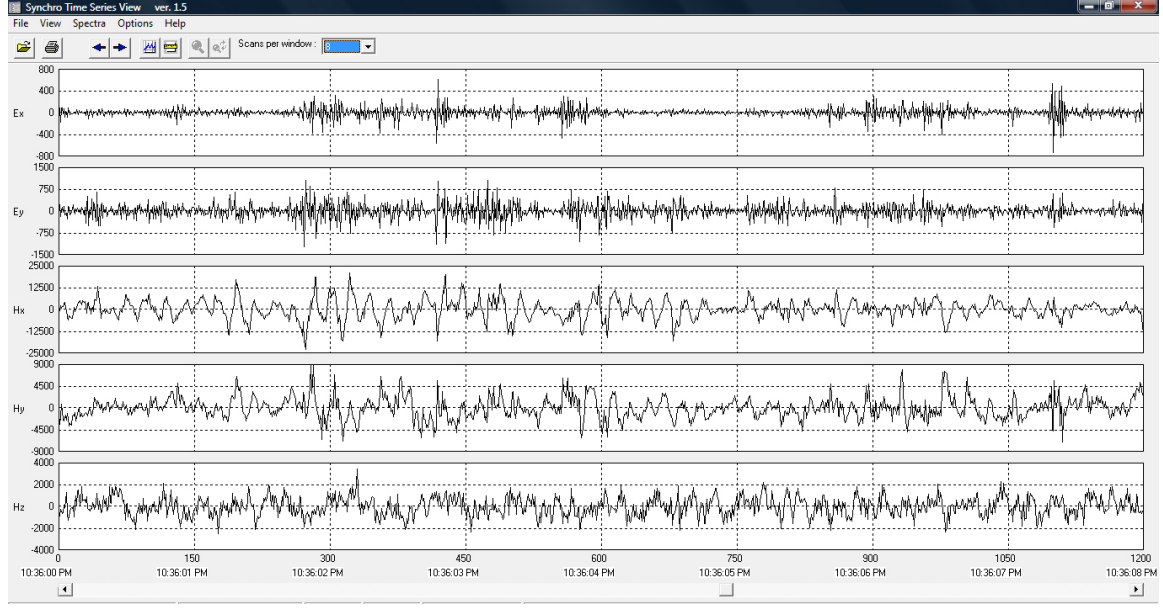
Figure 4.4: Time series data acquired by the 5-channel MT data acquisition system at Alid Geothermal area (sounding 010). Only part of the measured data is shown.

As the measured data contains noise, the main purpose of data processing is to extract sets of smooth, repeatable earth response functions from time series signals. Data processing in geophysics deals with reducing the noise from the measured data and increasing the signal-to-noise ratio. It includes the processing or reduction of the collected bulk data to a new data set that is ready for numerical modelling.

Although a former dataset of processed files, Electrical Data Interchange (EDI) (SEG, 1991) for all the sites exists at ÍSOR (Eysteinsson et al., 2009), reprocessing of the time series was performed. The aim of the reprocessing was to obtain a better knowledge of the time series processing; similar EDI files were obtained and used for interpretation.

MT data quality improved spectacularly as a result of two developments, digital recording and the remote reference (RR) method (Gamble et al., 1979).

Using the programme SSMT2000, provided by Phoenix Geophysics (Phoenix Geophysics, 2005); Fourier Transforms were produced from the raw time series data. The process begin by visual inspection of the measured data. The programme offers an option of editing several site parameters. Each station is checked and corrected for name, instrument channels, measurement direction, distance between the electrodes and other information from the field crew layout sheet. The time interval is initially chosen for performing the FFT, first calculating the Fourier coefficients and later reprocess the Discrete Fourier Transform into crosspowers.

Auto-spectra density, in the frequency band (f_{j-m}, f_{j+m}) around the central frequency, f_j is calculated by (see e.g. Vozoff, 1991):

$$\langle A(f_j) \rangle = \sqrt{\frac{1}{2m+1} \sum_{k=j-m}^{j+m} A_k A^*_k} = \langle A_j A^*_j \rangle^{1/2} \quad (* \text{ means complex conjugate}) \qquad 4.1$$

where A is the Fourier transform elements of one of the five field components. In the same way, we can calculate the crosspower density at f_j of two channels, say A and B as:

$$\langle A(f_j) \cdot B(f_j) \rangle = \sqrt{\frac{1}{2m+1} \sum_{k=j-m}^{j+m} A_k B^*{}_k} = \langle A_j B^*{}_j \rangle^{1/2} \qquad 4.2$$

The coherency of the two channels can be defined as:

$$coh(A_j, B_j) = \frac{1}{2m+1} \sum_{k=j-m}^{j+m} \frac{|\langle A_k B^*{}_k \rangle|}{\sqrt{\langle A_k A^*{}_k \rangle \langle B_k B^*{}_k \rangle}} = coh(A,B)_j \qquad 4.3$$

which is between 0 and 1.

Estimation of MT transfer functions

In the MT transfer functions from the linear relationship of electric and magnetic field spectra of the impedance tensor in equations 3.49, there are only two equations with four unknown impedance values. It is clear that for this underdetermined system; at least two independent equations are needed in the frequency domain:

$$E_x(\omega) = Z_{xx}(\omega)H_x(\omega) + Z_{xy}(\omega)H_y(\omega) \qquad 4.4a$$
$$E_y(\omega) = Z_{yx}(\omega)H_x(\omega) + Z_{yy}(\omega)H_y(\omega) \qquad 4.4b$$

Measured electric and magnetic fields in equations 4.4a and 4.4b contain measurement noise and because of plane wave source field approximation, that introduce uncertainties in the impedance tensor. It is statistically desirable to have many record sets which allow averaging to reduce the noise. In each frequency band, each equation has crosspower generated in the frequency domain by multiplying the impedances in equations (4.4a, b) by the complex conjugates of the magnetic spectra, $H_x{}^*$ and $H_y{}^*$ in turn, giving four independent equations as follows:

$$\left.\begin{aligned}
\langle E_x(\omega)H_x{}^*(\omega) \rangle &= Z_{xx}(\omega)\langle H_x(\omega)H_x{}^*(\omega) \rangle + Z_{xy}(\omega)\langle H_y(\omega)H_x{}^*(\omega) \rangle \\
\langle E_x(\omega)H_y{}^*(\omega) \rangle &= Z_{xx}(\omega)\langle H_x(\omega)H_y{}^*(\omega) \rangle + Z_{xy}(\omega)\langle H_y(\omega)H_y{}^*(\omega) \rangle \\
\langle E_y(\omega)H_x{}^*(\omega) \rangle &= Z_{yx}(\omega)\langle H_x(\omega)H_x{}^*(\omega) \rangle + Z_{yy}(\omega)\langle H_y(\omega)H_x{}^*(\omega) \rangle \\
\langle E_y(\omega)H_y{}^*(\omega) \rangle &= Z_{yx}(\omega)\langle H_x(\omega)H_y{}^*(\omega) \rangle + Z_{yy}(\omega)\langle H_y(\omega)H_y{}^*(\omega) \rangle
\end{aligned}\right\} \qquad 4.5$$

The tipper is also found by solving the geomagnetic transfer functions in equation 3.50:

$$H_z(\omega) = \mathcal{T}_{zx}H_x(\omega) + \mathcal{T}_{zy}H_y(\omega) \qquad 4.6$$

That is, the crosspowers of H_z are taken with H_x and H_y to give two equations in T_{zx} and T_{zy},

$$\left.\begin{aligned}
\langle H_z(\omega)H_x{}^*(\omega) \rangle &= \mathcal{T}_{zx}\langle H_x(\omega)H_x{}^*(\omega) \rangle + \mathcal{T}_{zy}\langle H_y(\omega)H_x{}^*(\omega) \rangle \\
\langle H_z(\omega)H_y{}^*(\omega) \rangle &= \mathcal{T}_{zx}\langle H_x(\omega)H_y{}^*(\omega) \rangle + \mathcal{T}_{zy}\langle H_y(\omega)H_y{}^*(\omega) \rangle
\end{aligned}\right\} \qquad 4.7$$

Solving equations 4.5 and 4.7 yield the following six expressions as a function of the cross- and auto-powers of the EM fields:

30

$$Z_{xx} = \frac{\langle E_x H_x{}^* \rangle \langle H_y H_y{}^* \rangle - \langle E_x H_y{}^* \rangle \langle H_y H_x{}^* \rangle}{\langle H_x H_x{}^* \rangle \langle H_y H_y{}^* \rangle - \langle H_x H_y{}^* \rangle \langle H_y H_x{}^* \rangle} \qquad \text{4.8a}$$

$$Z_{xy} = \frac{\langle E_x H_x{}^* \rangle \langle H_x H_y{}^* \rangle - \langle E_x H_y{}^* \rangle \langle H_x H_x{}^* \rangle}{\langle H_y H_x{}^* \rangle \langle H_x H_y{}^* \rangle - \langle H_y H_y{}^* \rangle \langle H_x H_x{}^* \rangle} \qquad \text{4.8b}$$

$$Z_{yx} = \frac{\langle E_y H_x{}^* \rangle \langle H_y H_y{}^* \rangle - \langle E_y H_y{}^* \rangle \langle H_y H_x{}^* \rangle}{\langle H_x H_x{}^* \rangle \langle H_y H_y{}^* \rangle - \langle H_x H_y{}^* \rangle \langle H_y H_x{}^* \rangle} \qquad \text{4.8c}$$

$$Z_{yy} = \frac{\langle E_y H_x{}^* \rangle \langle H_x H_y{}^* \rangle - \langle E_y H_y{}^* \rangle \langle H_x H_x{}^* \rangle}{\langle H_y H_x{}^* \rangle \langle H_x H_y{}^* \rangle - \langle H_y H_y{}^* \rangle \langle H_x H_x{}^* \rangle} \qquad \text{4.8d}$$

$$\mathcal{T}_{zx} = \frac{\langle H_z H_x{}^* \rangle \langle H_y H_y{}^* \rangle - \langle H_y H_x{}^* \rangle \langle H_z H_y{}^* \rangle}{\langle H_x H_x{}^* \rangle \langle H_y H_y{}^* \rangle - \langle H_y H_x{}^* \rangle \langle H_x H_y{}^* \rangle} \qquad \text{4.8e}$$

$$\mathcal{T}_{zy} = \frac{\langle H_z H_y{}^* \rangle \langle H_x H_x{}^* \rangle - \langle H_z H_x{}^* \rangle \langle H_x H_y{}^* \rangle}{\langle H_x H_x{}^* \rangle \langle H_y H_y{}^* \rangle - \langle H_y H_x{}^* \rangle \langle H_x H_y{}^* \rangle} \qquad \text{4.8f}$$

In estimating the Z_{ij} as in the above equations, crosspowers could of coarse be taken with the conjugates of the electric field ($E_x{}^*$ and $E_y{}^*$) instead of $H_x{}^*$ and $H_y{}^*$.

Remote-reference estimates

All of the equations 4.8 contain auto-powers of the magnetic field and the problem with above procedure is the biasing effect of noise. The coherent noise present in the data at a single site will cause the impedance estimate, Z_{ij}, to be biased. The remote reference method (Goubau et al., 1979; Gamble et al., 1979; Clarke et al., 1983) is designed to overcome such environmental noise. It involves deploying additional remotely recording sensors (usually magnetic) at a site completely outside of the influence of cultural noise at the local soundings. The uncontaminated (natural) part of the induced field can be expected to be coherent over longer distances, whereas noise is generally random and incoherent. Therefore, by measuring selected electromagnetic components at both local and remote sites, bias effects arising from the presence of noise that is uncorrelated between sites can be removed. The distance between local and remote sites needs to be large enough that the sources of noise are incoherent. In this study, the remote reference (RR) was located about 10 km away from the measurement area.

Multiplying the linear relationship of electric and magnetic field spectra of the impedance tensor in equation 4.4a, b with the remote site components, $R_x{}^*$ and $R_y{}^*$ and averaging over a number of determinations, the pairs of simultaneous equations for impedance can be solved to get the following remote reference estimates of the impedance tensor elements Z_{ij} as follows:

$$Z_{xx} = \frac{\langle E_x R_x{}^* \rangle \langle H_y R_y{}^* \rangle - \langle E_x R_y{}^* \rangle \langle H_y R_x{}^* \rangle}{\langle H_x R_x{}^* \rangle \langle H_y R_y{}^* \rangle - \langle H_x R_y{}^* \rangle \langle H_y R_x{}^* \rangle} \qquad \text{4.9a}$$

$$Z_{xy} = \frac{\langle E_x R_x{}^* \rangle \langle H_x R_y{}^* \rangle - \langle E_x R_y{}^* \rangle \langle H_x R_x{}^* \rangle}{\langle H_y R_x{}^* \rangle \langle H_x R_y{}^* \rangle - \langle H_y R_y{}^* \rangle \langle H_x R_x{}^* \rangle} \qquad \text{4.9b}$$

$$Z_{yx} = \frac{\langle E_y R_x{}^* \rangle \langle H_y R_y{}^* \rangle - \langle E_y R_y{}^* \rangle \langle H_y R_x{}^* \rangle}{\langle H_x R_x{}^* \rangle \langle H_y R_y{}^* \rangle - \langle H_x R_y{}^* \rangle \langle H_y R_x{}^* \rangle} \qquad\qquad 4.9c$$

$$Z_{yy} = \frac{\langle E_y R_x{}^* \rangle \langle H_x R_y{}^* \rangle - \langle E_y R_y{}^* \rangle \langle H_x R_x{}^* \rangle}{\langle H_y R_x{}^* \rangle \langle H_x R_y{}^* \rangle - \langle H_y R_y{}^* \rangle \langle H_x R_x{}^* \rangle} \qquad\qquad 4.9d$$

where R_x and R_y denote the magnetic components, H_x and H_y of the remote reference station, respectively. It is also possible to use the electric fields, E_x and E_y of the remote reference as the R_x and R_y in equation 4.9. But it is more common to use the magnetic field because horizontal magnetic field is thought to be less susceptible to polarization, and is less contaminated by noise than the electric field. An important property of RR procedure is that it also provides estimates of noise spectrum in each channel (Gamble et al., 1979). This makes it possible to estimate the noise in each of the impedance elements at each frequency.

But in many circumstances with high noise effects, the resulting crosspowers may not be as smooth as desired. Therefore, manual editing in the MT-Editor programme of the stacked apparent resistivity values for each frequency will help produce reasonable results and smoother curves.

The MT-Editor is a window based programme that takes as input crosspower files created by SSMT2000. It merges the crosspowers and displays its calculations graphically. This allows us to view the different characteristics of the soundings, such as apparent resistivity, phase, impedance, strike direction, coherence and so on across the full frequency range that was acquired. MT-Editor also offers the removal of individual crosspowers from the calculations, allowing poor quality data to be edited out. The edits are made by changing a mask, not by deleting the data (Phoenix Geophysics, 2005), so it is easy to restore individual crosspowers or revert to the initial view. The programme includes an auto-edit capability that quickly masks crosspowers that lie too far from the mean, often saving considerable time in the editing process.

The output of MT-Editor (edi file) was then run through a programme called edi2edi made at ÍSOR which calculates various MT parameters (not calculated in MT-Editor) and produces the result in the standard of the Electrical Data Interchange (EDI) which is ready for interpretation. Two examples of processed MT data in terms of magnitude and phase of impedance elements from Alid geothermal area are presented in Figure 4.5 (impedance elements of each MT site including determinant impedance are presented in Appendix 3 in the report by Eysteinsson et al., 2009). The apparent resistivity and phase curves calculated from these impedance elements, according to equation 3.38 are presented in Figure 4.6 (plot of apparent resistivity and phase of MT data including other parameters: Skew, ellipticity, tipper, Zstrike, coherency etc for each site are presented in Appendix 4 in the report by Eysteinsson et al., 2009).
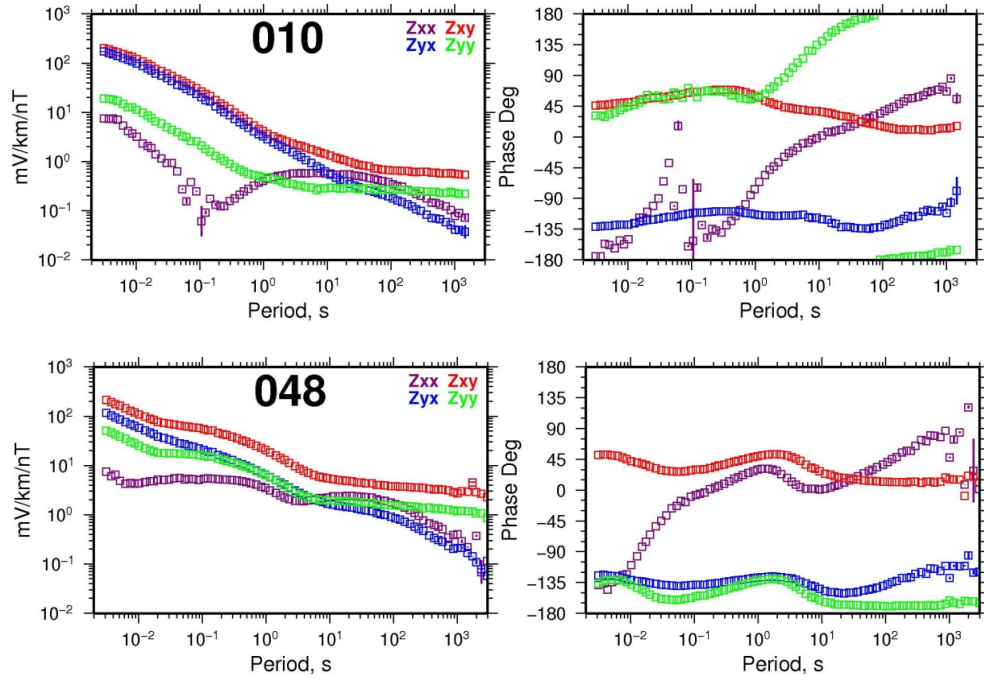
Figure 4.5: Impedance elements from Alid MT sites, 010 and 048 with the amplitudes on the left and the phases on the right. Diagonal elements are in purple (Z$_{xx}$) and green (Z$_{yy}$), while the off diagonal elements are in red (Z$_{xy}$) and blue (Z$_{yx}$).
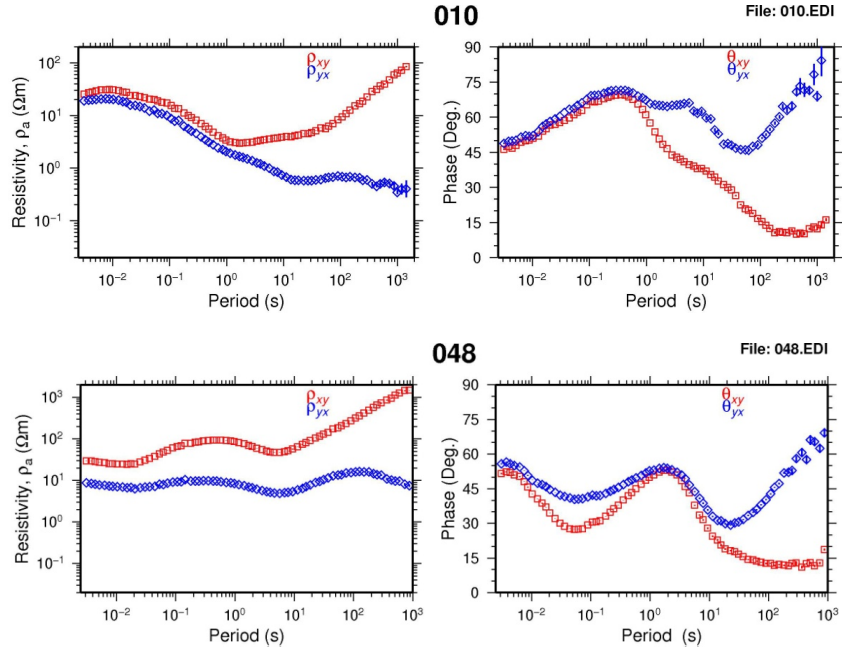
Figure 4.6: Apparent resistivity and phase curves in the measured direction (xy-NS and yx-EW). The apparent resistivity and phase curves are calculated from the impedance elements in Figure 4.5.

5 MT data Analysis from Alid Geothermal field, Eritrea

The first steps when interpreting MT data are: (1) to understand the inherent dimensionality of the data, (2) to determine the appropriate strike direction for interpretation, and (3) to remove, as much as possible, the effects caused by local near-surface resistivity inhomogeneities. The pitfalls inherent in interpreting MT data with inappropriate dimensionality assumptions have been described by many authors over the last several decades. One dimensional interpretation of 2D data is known to introduce among other artifacts "false conducting layers" (Berdichevsky and Dmitriev, 1976). Two dimensional interpretation of 3D data can lead to underestimates of the total conductance (Wannamaker et al., 1984, Martinelli et al., 2000). Interpretation in an incorrect coordinate system (if data are not rotated to a proper geo-electric strike) will yield erroneous structure in the model. Finally, near-surface resistivity features distort the regional responses that, if not removed, will also give inaccurate information about the subsurface.

5.1 Dimensionality analysis of the MT soundings

An important procedure in the analysis of MT data, which is very useful for interpretation, is to examine whether the impedance tensors and tippers at each site are consistent with a 1D or 2D structure or whether they indicate a structure with a more complex 3D form. Various techniques have been developed to determine the dimensionality of the electrical conductivity structure. Some of the main parameters from which information about the dimensionality is obtained are *skew*, *polar diagrams*, *Tipper magnitude* and *ellipticity*.

The Swift's skew (κ) of the impedance tensor (Swift, 1967) is a rotationally invariant parameter which defined by:

$$\kappa = \left| \frac{Z_{xx} + Z_{yy}}{Z_{xy} - Z_{yx}} \right| \qquad\qquad 5.1$$

If the data are noise free then for one dimensional structure, Z_{xx} and Z_{yy} are zero but Z_{xy} and Z_{yx} are non-zero and unequal; hence, $\kappa = 0$. In practice, when $\kappa < 0.1$ and the impedance (apparent resistivities and phase) in the two orthogonal directions are equal, the subsurface structure is treated as 1D. If the skew is small and the apparent resistivities are different, then a 2D assumption is made. When the skew is large exceeding 0.25–0.3, then 3D effects are assumed to be strong (Vozoff, 1991). For sites with appropriate symmetry relative to the 3D structure, it can have lower values (Groom and Bailey, 1989). Figure 5.1, shows plots of skew for 11 MT soundings evenly distributed over the study area, which are considered as examples to represent the present study area and Figure 5.2 shows pseudo-sections of skew values from two sections across and along the rift. The skew is > 0.25 for periods > 10 s. These high skews are an indication of either 3D resistivity structures or high level of noise. Man made electrical noise, such as power lines, moving vehicles and trains can have a negative effect on MT data quality. As the survey area (Alid) is remotely isolated from all such cultural noise sources, their effect is considered to be negligible. Therefore, the high value of the skew is believed to show 3D resistivity structure at depth. In general, the skew increases with increasing period as the response become more sensitive to regions at greater depth and greater distance from the site. From these high

values of skew in Alid geothermal area, 3D modelling approach would be the best way to understand the structure of the area.
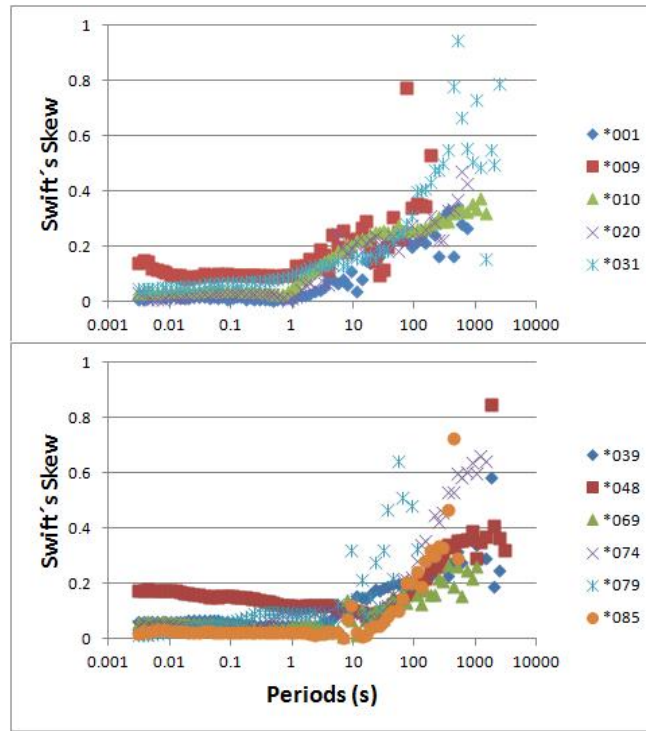
Figure 5.1. Swift's skew values for 11 sites. The sites are evenly distributed in the study area. Plots of Swift's skew values for each MT soundings are presented in Appendix 4 in the report by Eysteinsson et al., 2009).
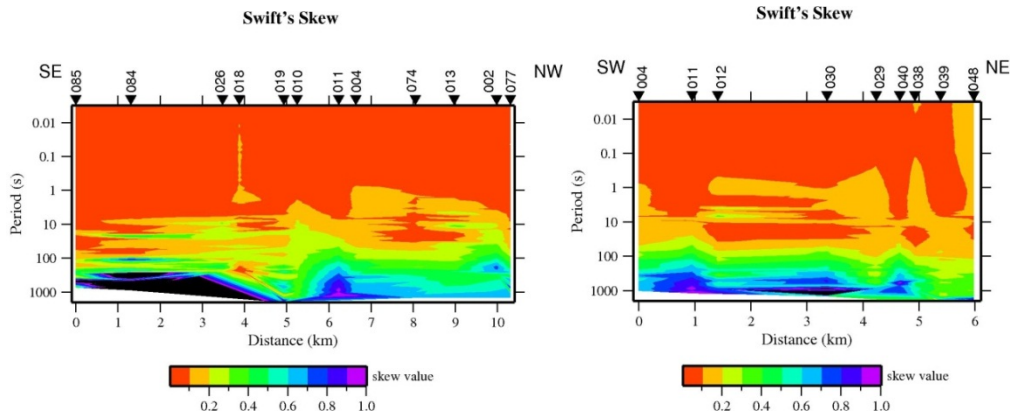
*Figure 5.2. Pseudo-sections of skew values of two profiles: along the rift axis (left) and across the rift axis (right).*

Another dimensionality parameter which is defined by the ratio of the impedance tensor similar to the skew but now variant with rotation is the ellipticity (*E*) and is defined by:

$$E(\alpha) = \left| \frac{Z_{xx}(\alpha) - Z_{yy}(\alpha)}{Z_{xy}(\alpha) + Z_{yx}(\alpha)} \right| \quad \text{(where } \alpha \text{ is angle of rotation)} \quad \quad 5.2$$

For noiseless data, its value will be zero for 1D structure and for 2D case it will also be zero provided that the x or y axis is along the geo-electric strike direction. Figure 5.3 shows ellipticity values from the same MT soundings as discussed above for the skew parameter after rotating the data to the main geo-electric strike (N35°W).
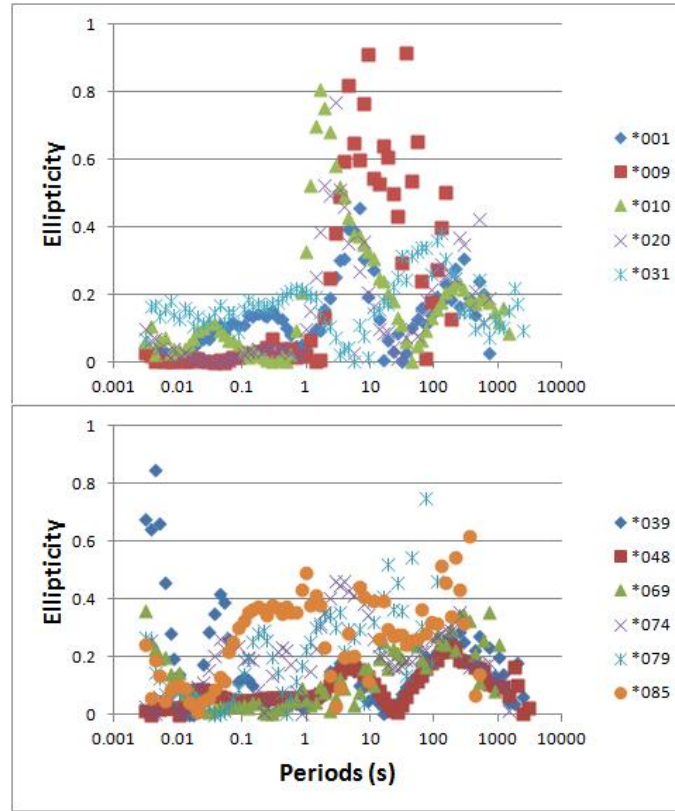
Figure 5.3. Ellipticity values for 11 sites. The sites are evenly distributed in the study area. Plots of ellipticity for each MT soundings are presented in Appendix 4 in the report by Eysteinsson et al., 2009).

The ellipticity values are high for periods > 10 s and for site 039, the value is high even for at short periods. These high ellipticities similar to the skews are an indication of a strong non-1D resistivity response to the geological structures.

Tipper magnitude (T) is a measure of the "tipping" of the magnetic field out of the horizontal plane (Vozoff, 1991). It is zero for a 1D earth. In general, for a multidimensional earth the vertical magnetic component is equal to $T_xH_x + T_yH_y$ (see eq. 3.50), where T represents the tipper. Tipper magnitude is defined by:

$$|T| = \sqrt{|T_x|^2 + |T_y|^2}$$, Tipper becomes large as the structure becomes strongly non-1D. An example of tipper magnitude from Alid area (sounding 078) is shown in Figure 5.4.
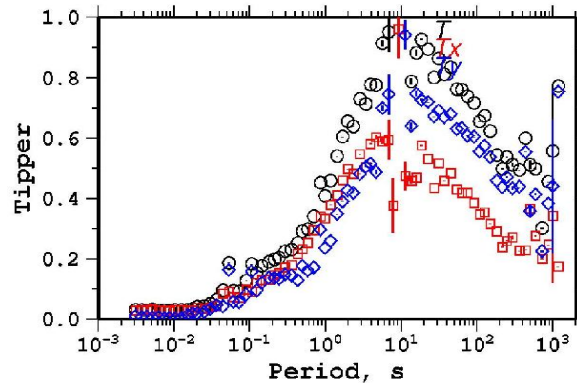
Figure 5.4. Tipper magnitude from sounding 078, Alid Geothermal area. Red points are T_x, blue points are T_y and black points are total tipper (T). Plots of tipper values for each MT soundings are presented in Appendix 4 in the report by Eysteinsson et al., 2009).

The figure shows that tipper is greater than 0.2 for periods > 1 s showing a strongly non-1D resistivity structure below the sounding site.

The fourth parameter which provides a measure of the MT data dimensionality is impedance polar plots (Reddy et al., 1977). Polar diagrams are plots of $|Z_{xy}|$ and $|Z_{xx}|$ for a rotation from 0 to 360° at a particular frequency. Such plots from 1D data show circles of $|Z_{xy}|$ and $|arg Z_{xy}|$ with a radii $|Z|$ and $|arg Z|$ and invariant with rotation; while polar diagrams for $|Z_{xx}|$ collapse to a point or minimal. For 2D resistivity structures, the principal impedance polar diagrams elongate either parallel or perpendicular to strike direction. Also for 2D structures the additional impedance polar diagrams from $|Z_{xx}|$ attain the shape of a symmetric cloverleaf while for 3D resistivity structure, these polar diagrams become elongated in one direction and their amplitudes are comparable to those of principal impedances, an example of these cases is presented in Figure 5.5a. Based on the analysis of polar diagrams, most of the sites from Alid show that the resistivity structure at longer periods is three dimensional and one dimensional for shorter periods. An example of polar diagrams from Alid MT data (soundings 019 and 078) with 1D and 3D structures at 40 Hz (0.025 s) and 0.00229 Hz (436 s) is shown in Figure 5.5b.
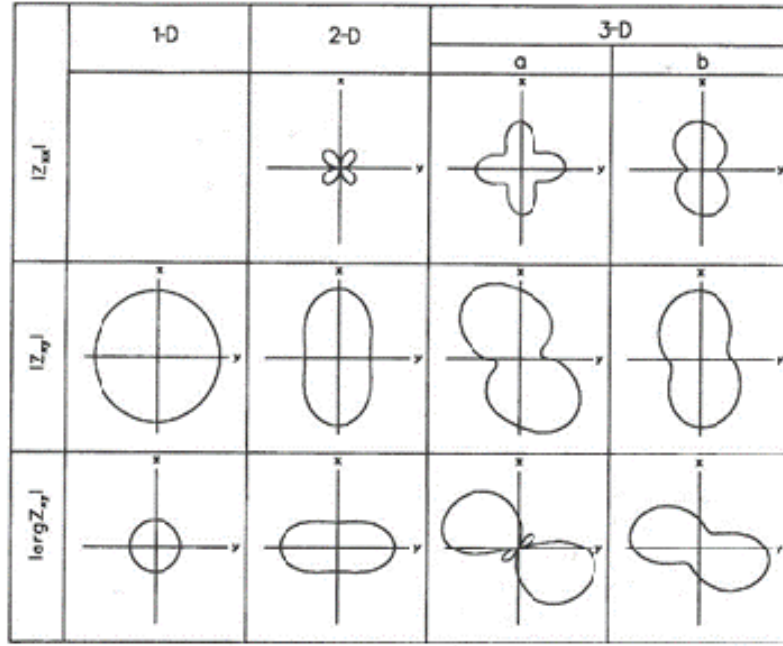
(a)
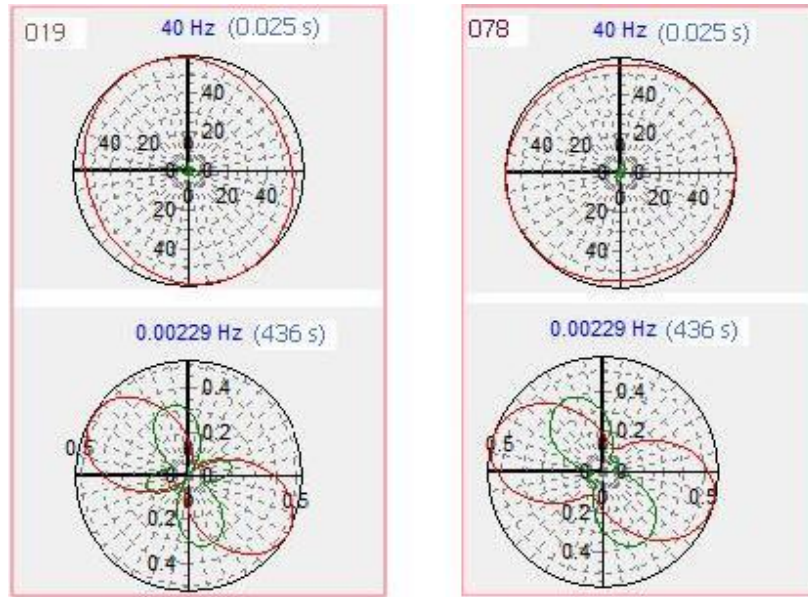
(b)

Figure 5.5. (a) examples of polar diagrams of impedance tensor, taken from Berdichevsky and Dmitriev, 2002 showing 1D, 2D and 3D form of the polar plots; and (b) examples of polar diagrams of impedance tensor from Alid MT data for soundings 019 and 078 at 40 Hz (0.025 s) and 0.00229 Hz (436 s). Red plots are polar diagrams of Z_{xy} and green plots are polar diagrams of Z_{xx}. Numbers on top left of each polar diagram are sounding names.

Polar diagrams of sounding points 019 and 078 indicate that there is a 1D resistivity structure below the measurement sites at the depth probed by the high frequency (040 Hz) and a 3D resistivity structure at the depth probed by the low frequency (0.0229 Hz).

5.2 MT responses as a measure of dimensionality

The impedance tensor contains information on the subsurface resistivity structure. Examples of impedance tensors from two MT sites from Alid geothermal area are presented in Figure 4.5. The diagonal elements of the impedance tensor (Z_{xx} and Z_{yy}) for sounding 010 are non zero but are much lower in magnitude than the off diagonal elements up to about 1 s. The off diagonal impedance elements (Z_{xy} and Z_{yx}) are of similar magnitude, indicating a 1D resistivity structure at short periods (or at shallow depth). At deeper levels or for long periods, greater than 10 s, almost all the impedance elements are of the same order of magnitude. This indicates that there is a higher degree of three dimensionality in the resistivity structure in the subsurface below the measurement site. All the impedance elements for sounding 048 seem to be slightly different in magnitude except for the diagonal element (Z_{xx}) which is lower by about an order of magnitude than the rest of the impedance elements for periods up to 1 s, and the main impedance elements (off diagonal) are observed to split for all the period range.

Small inhomogeneous bodies near the surface cause distortions in the electromagnetic fields. The anomalous body has galvanic effects which add to the MT response of the background conductivity of the medium by shifting the resultant resistivity curves (on log-scale) and causes serious interpretational errors in the data (see section 3.6 for details of galvanic effects, and section 5.4 for static shift). These galvanic effects are independent of frequency and static shift does not have any effect on phase curves.

Apparent resistivity and phase curves for both soundings in Figure 4.5 are presented in Figure 4.6. When the static shift was considered for sounding 048 (for both xy and yx apparent resistivity curves), by inverting them separately with a TEM sounding of the same site or close by, the xy apparent resistivity curve was severely shifted by a factor of 4 while the yx curve remained un-shifted. The phase curves for the two modes (xy and yx) of sounding 048 in Figure 4.6 are splitting even at short periods. The splitting nature of the phase curves which are not affected by static shift is an indicative of two or three dimensionality; therefore, the resistivity curves are affected by the combination of both galvanic distortion and three dimensional nature of the subsurface.

Figure 5.6 shows pseudo-sections of MT apparent resistivity and phase responses for TE and TM modes in two profiles, one across the rift axis Figure 5.6a (data rotated with X in N35°W) and the other along the rift axis Figure 5.6b (data rotated with X in N55°E). Much information about the general resistivity distribution of the area and dimensionality can be gained from these pseudo-sections. The phase response is related to the resistivity gradient, and phase values close to 45° indicate that the resistivity is relatively uniform with depth. Phase values exceeding 45° indicate a decrease of resistivity with depth, whereas values < 45° indicate an increase in resistivity with depth.

The figure shows that, generally the apparent resistivity and phase of TE and TM modes curves do split greatly for all the sites with periods > 1s. Differences between these two mode responses provide an indication of the presence of significant non-1D structures.
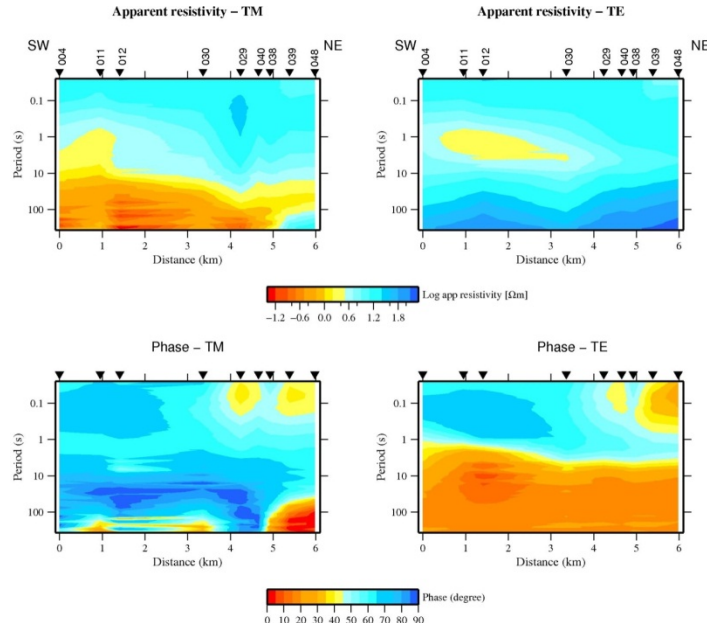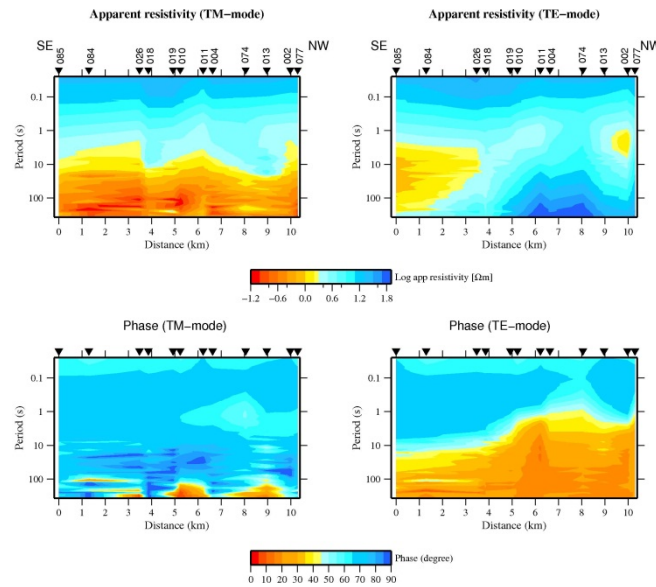
Figure 5.6. Pseudo sections of TM and TE apparent resistivity and phase modes from Alid MT data. (a) Across the rift axis (data rotated with X in N35°W), (b) along the rift axis (data rotated with X in N55°E).

5.3 Strike direction analysis

Prior to 2 or 3 dimensional inversion of MT data, knowledge of the orientation of the geo-electrical strike of the data is a precondition, so that a proper rotation of the data to the direction of the general electrical strike can be done. Strike direction can be found by making strike direction analysis of the MT data.

Zstrike or the Swift angle gives the electrical strike. It is the horizontal rotation which maximizes the off-diagonal elements of the MT tensor and minimizes the diagonal ones, using the sum of the squared modules of these components (see equations 3.65 and 3.66). For periods greater than 10 s, the main electric strike is found to be N35°W for most of the Alid MT sites which is parallel to the rift direction as can be observed from the geology of the area (Figure 2.2). The Swift strike has 90° ambiguity (see equation 3.67) and the strike direction can´t be determined using MT impedance data alone. This ambiguity can be resolved by the information from tipper vector if vertical magnetic field (H_z) is available. Additional information such as local geology might help to overcome this ambiguity. Figure 5.7 shows rose diagrams of strike directions (Zstrike) for periods greater than 10 seconds for all the MT sites. At higher frequencies, the strike direction is poorly defined due to the local resistivity variations at each site.
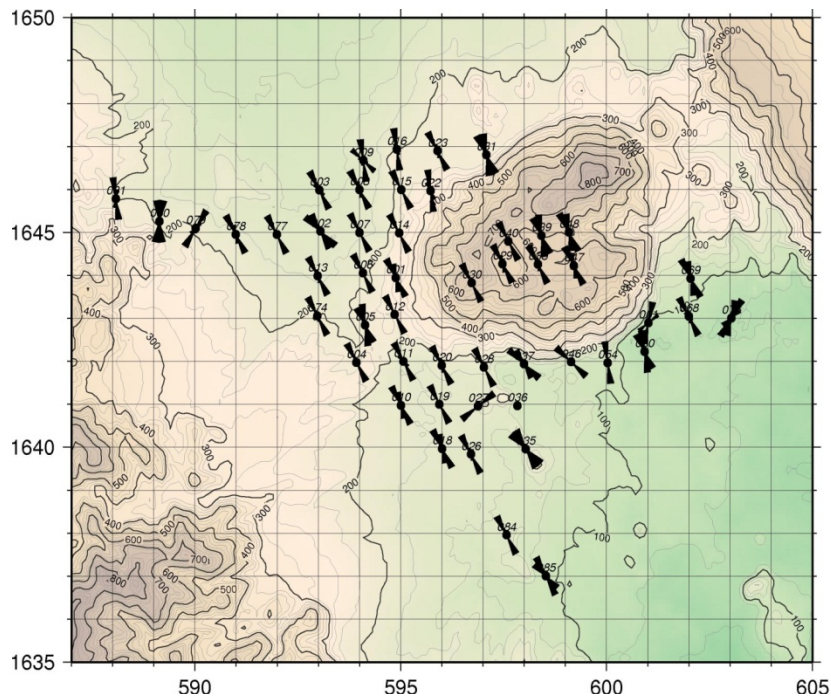
Figure 5.7. Rose diagram of Zstrike directions for periods greater than 10 s, for all MT sites.

The magnetic transfer function (or tipper, discussed in section 5.1) is a response which relates the vertical component of the magnetic field to the two horizontal components (Vozoff, 1991). This response is often displayed graphically in the form of induction arrows. Since vertical magnetic fields are generated by lateral conductivity gradients, induction arrows can be used to infer the presence or absence of lateral variations in conductivity. These vectors, as they are independent of the MT impedance tensor, can provide valuable constraints on the dimensionality and strike analysis of the data.

Figure 5.8 shows the real part (blue) and imaginary part (red) of the arrows for a period of 100 seconds (approximately 3-6 km depth considering the resistivity of the area on the average is around 0.36-1.44 Ωm) from Alid MT sites where vertical magnetic component (H_z) was measured. In this report, the Wiese convention was used in which the real

induction arrows (blue) point away from the conductive zone. The figure shows that the conductor is along the main rift axis below and around Mt. Alid.
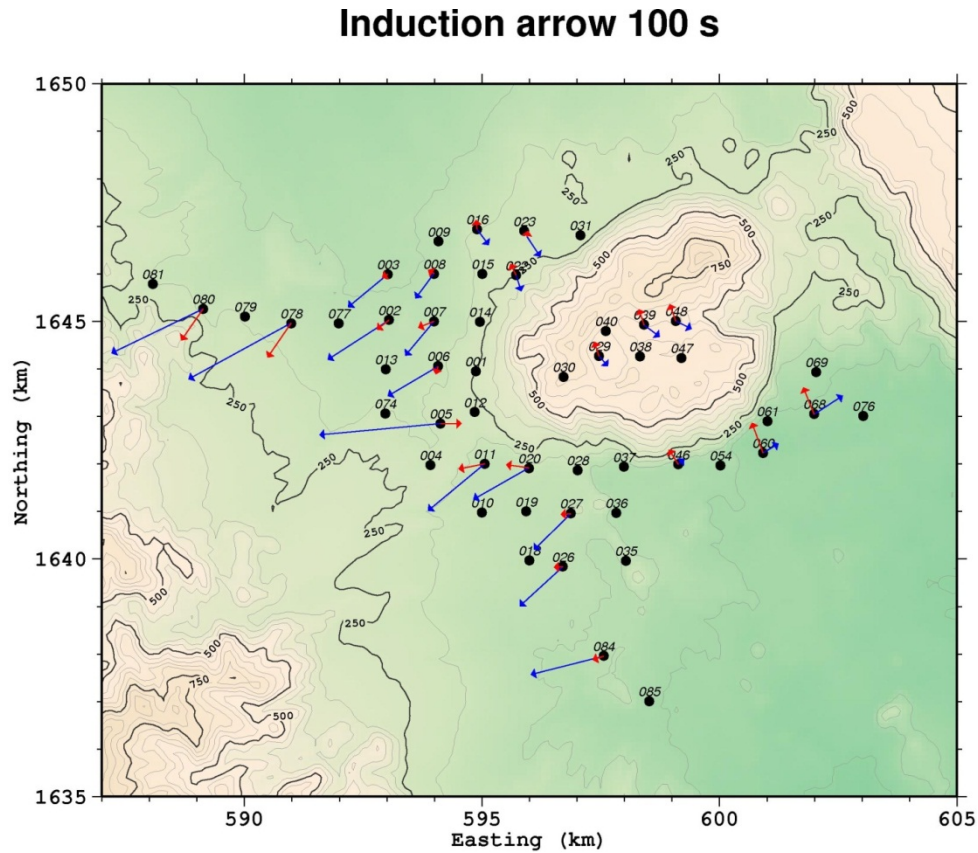
Figure 5.8. Induction arrows for Alid MT data (where H_z was measured), real part (blue) and imaginary part (red).

5.4 Static shift problem and its remedy

Near surface resistivity inhomogeneities and rough topography can severely distort magnetotelluric (MT) apparent resistivity data, thereby limiting interpretational accuracy. This results in an unknown scale factor or static shift factor (S) of the MT apparent resistivity, which is independent of frequency. The galvanic distortion effect is due to an electric field generated from boundary charges on near surface inhomogeneities, and persists throughout the entire MT recording stage. Static shifts are manifested in the data as vertical, parallel shifts of log-log apparent resistivity sounding curves, the phase being unaffected.

If the static shift is not accounted for prior to MT modelling or inversion, then the resistivity value determined will be offset by an amount equal to S, whilst the depth at which an anomaly resides at, will be shifted by the square root of the scaling factor (S). If the recording electrode(s) is situated directly above a localized high resistivity, then the MT apparent resistivity curve will be shifted upwards, whereas for electrode(s) located within a conductive body causes downward shift (Figure 5.9).

Figure 5.9. Theoretical sketches of MT apparent resistivity curves distorted by static shift. Electrodes located within high resistivity can cause upward shift (top red curve), whereas location within a conductive body causes downward shift (bottom green curve). Middle broken curves are static shift corrected with a TEM sounding (blue curve) located at the same site.

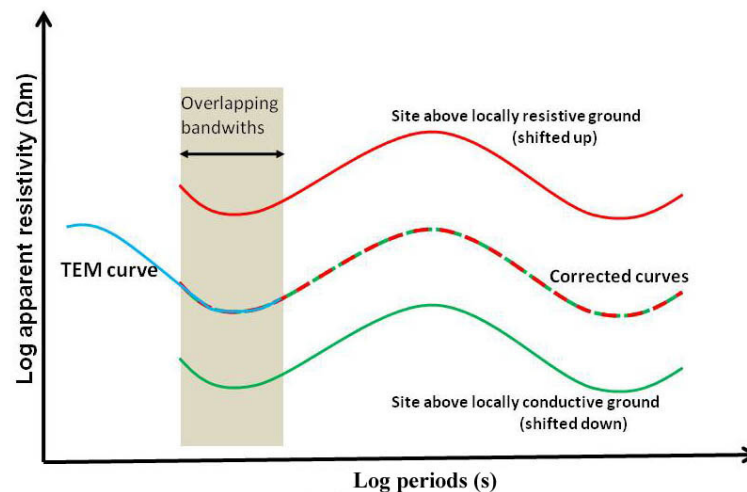The MT static shift cannot be determined directly from conventionally recorded MT data at a single site. Several attempts have been made to correct the static shift and one of the methods is a controlled source measurement of the magnetic field (Sternberg et al., 1988; Pellerin and Hohmann, 1990; Árnason, 2008). Using central-loop TEM data acquired at the same location provides a natural remedy for the MT static shift. This is because TEM is less sensitive to near surface resistivity variations at late times as it records the secondary magnetic field and the magnetic field is not affected by charge accumulations at the boundaries of shallow resistivity heterogeneities.

Central-loop TEM sounding as a remedy for MT static shift problem

In the central-loop TEM sounding method, a current in the ground is induced by a time-varying magnetic field of a controlled magnitude generated by a source loop. A loop of wire is placed on the ground and a constant magnetic field of known strength is built up by transmitting a constant current into the loop (Figure 5.10a, b). The current is then abruptly turned off. The decaying magnetic field induces electromotive force in the ground (Figure 5.10b-middle).

The induced current initially concentrates below the transmitter loop (Figure 5.10c-top) but then the currents will diffuse down and away from the transmitter (Figure 5.10c-bottom). The current distribution in the ground generates a secondary magnetic field decaying with time. The decay rate of the secondary magnetic field is monitored by measuring the voltage induced in a receiver coil at the centre of the transmitting loop in logarithmically distributed time gates (Figure 5.10b-bottom). The current distribution and the decay rate of the secondary magnetic field depend on the resistivity structure of the earth. The decay rate, recorded as a function of time after the current in the transmitter loop is turned off, can, therefore, be interpreted in terms of the subsurface resistivity structure (Árnason, 1989).
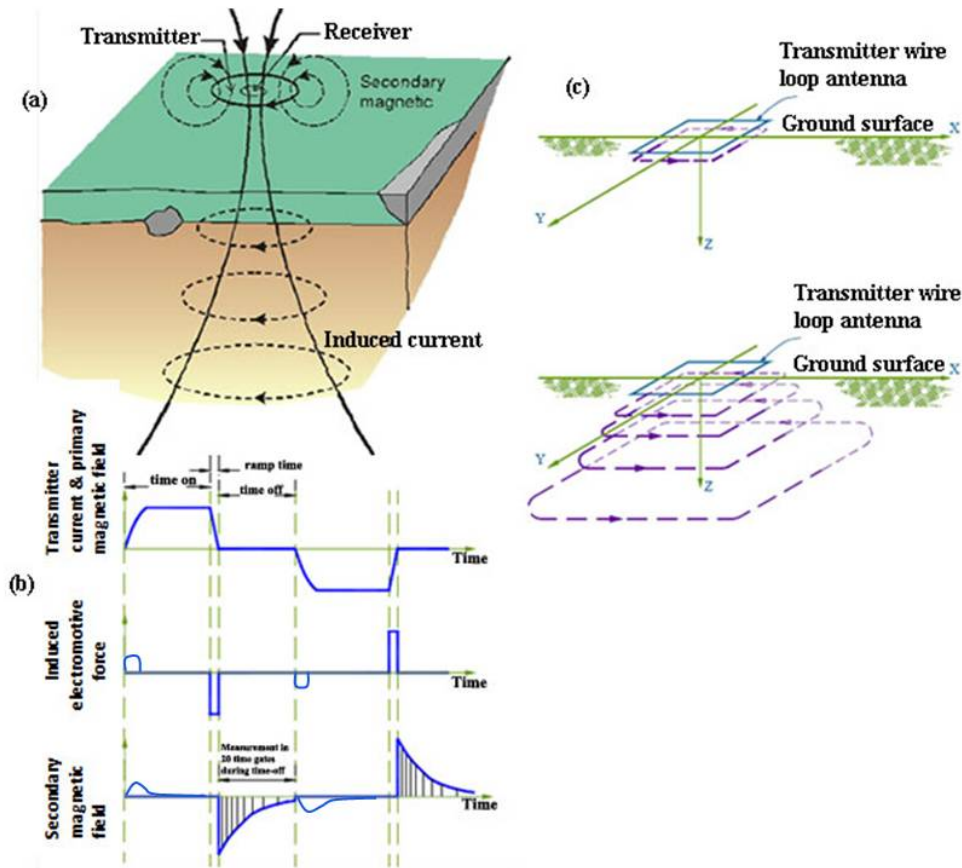
Figure 5.10. Central loop TEM configuration (taken from Hersir and Björnsson, 1991)(a), TEM waveforms (b), TEM eddy current flow: immediately after current turn-off (top) and at late times (bottom) (modified from Rowland, 2002 after McNeill, 1990).

In this study, TEM data were collected using PROTEM digital receiver and a TEM-67 transmitter from Geonics Ltd. in Canada. The sounding data were made by transmitting current into a big transmitter wire loop with an effective area of 90,000 m^2 (300 m × 300 m) and the response was measured by a receiver loop, a small coil with an effective area of 100 m^2, placed at the center of the transmitter loop (Figure 5.10a). The maximum transmitted current was usually in the range of 18-22 A, transmitted at the high frequency of 25 Hz, and low frequency of 2.5 Hz. For each frequency, 20 measuring time gates are evenly spaced on log-scale from 0.09 to 7 ms for the high frequency and 0.9 to 70 ms for the low frequency after the current turn off. Repeated transients are stacked and stored in the computer memory of the receiver and later downloaded to a personal computer ready for further processing.

The TemX programme was used to read raw data files downloaded from the PROTEM receiver (Árnason, 2006b). The TemX programme calculates averages and standard deviations for repeated transient voltage measurements and calculates late time apparent resistivity as a function of time. It also offers rejecting noisy readings through graphical-user interface (GUI).

44

The resulting TEM data were then 1D jointly inverted with an MT sounding at the same site to be shift corrected (for this project, previously processed TEM data were used, Eysteinsson et al., 2009). In the 1D joint inversion, a shift multiplier, S, is taken as an unknown parameter along with the 1D resistivity model. In the inversion, S and the model parameters are adjusted to fit both data sets simultaneously.

An example of 1D inversion of MT data only (without TEM data) and a joint inversion of MT and TEM data is shown in Figure 5.11. The MT apparent resistivity and phase data are shown as blue squares and blue circles, respectively and the corresponding TEM apparent resistivity data are shown by red diamonds. The response of the joint MT/TEM inversion model is shown by purple line and the responses of the resulting model from the inversion of the un-shifted MT apparent resistivity and phase data is shown by the green apparent resistivity curve. The 1D models are shown in the right panel, the model in purple colour being for the joint inversion and the model in green being for the inversion of the un-shifted MT data. The shift multiplier is 0.36 (upper right hand corner of the apparent resistivity panel). Original calculated MT apparent resistivity has to be divided by this shift multiplier so that it is consistent with the TEM sounding.
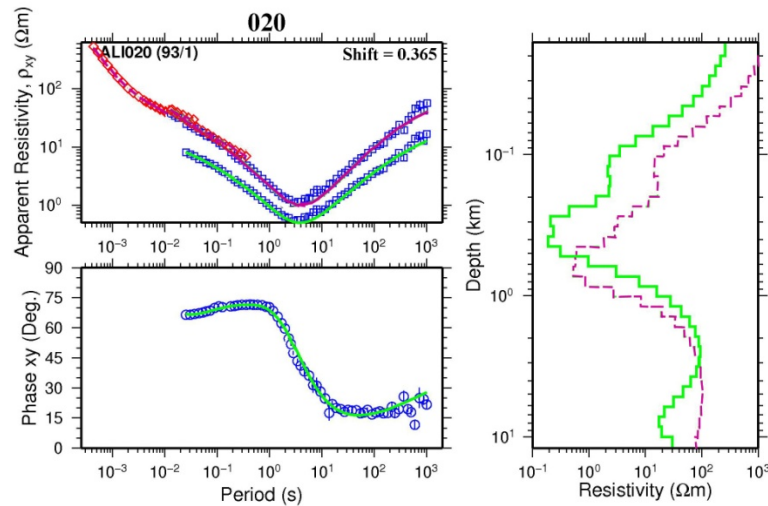
Figure 5.11. An example of 1D Occam inversion of MT data (xy – mode). The un-shifted MT data is shown by blue apparent resistivity squares (upper left and lower curve) and the phase by blue circles (lower left). Inversion result of the unshifted data resulted in the green model to the right and its response is shown by the green curve on the left. The joint inversion of MT and TEM data (red diamonds) resulted in the upper apparent resistivity curve with a shift factor of 0.365 and the purple resistivity model to the right, its response is shown by the purple apparent resistivity curve on the upper left figure. Note the phase response is the same for both models.

6 Multidimensional Inversion of MT Data from Alid Geothermal Area

6.1 1D INVERSION

As described in the previous chapter, information from the data analysis indicates that the MT data from Alid geothermal area are highly three dimensional mainly at longer periods. Therefore, 3D inversion is expected to give a better idea about the resistivity distribution of the area. However, 1D inversion is straightforward in usage and fast enough in obtaining the resistivity distribution of layers as a function of depth for a quantitative interpretation of the MT data. 1D inversion was performed of the data using an inversion programme called TEMTD (Árnason, 2006a).

6.1.1 Overview of the TEMTD programme

The TEMTD programme can perform 1D inversion both for TEM and MT data separately as well as jointly. For TEM inversion alone, the programme assumes that the source loop is a square loop and that the receiver coil/loop is at the centre of the source loop (see section 5.4 for TEM configuration). The current wave form is assumed to be a half-duty bipolar semi-square wave with exponential current turn-on and linear current turn-off. The programme also uses GNUPLOT graphics programme for graphical display during the inversion process.

The programme TEMTD solves forward and inverse problems. The inversion problem is to determine those model parameters which give the model response close to the measured response. The forward problem calculates the response from given model parameters. The model response depends non-linearly on the model parameters, the inversion algorithm used in the programme is the non-linear least-square inversion of the Levenberg-Marquardt type (Levenberg, 1944; Marquardt, 1963). The misfit function is the root-mean-square difference between measured and calculated values (χ^2), weighted by the standard deviation of the measured values.

The programme offers the possibility of keeping models smooth, both with respect to resistivity variations between layers (logarithm of conductivities) and layer thicknesses (logarithm of ratios of depth to top and bottom of layers). The damping can be done both on first derivatives which counteracts sharp steps in the model and on the second derivatives which counteracts oscillations in the model values. The actual function that is minimised is not just the weighted root-mean-square misfit, χ^2, but the potential:

$$Pot = \chi 2 + \alpha \cdot DS1 + \beta \cdot DS2 + \gamma \cdot DD1 + \delta \cdot DD2 \qquad 6.1$$

Where DS1 and DS2 are the first and second order derivatives of log conductivities in the layered model, and DD1 and DD2 are the first and second order derivatives of the logarithms of the ratios of layer depths. The coefficients α, β, γ and δ are the relative contributions of the different damping terms and are controlled by the user.

The programme can also be used to perform minimum structure (Occam) inversion (see e.g., Constable et al., 1987). In this case the thicknesses of layers are kept fixed, equally spaced on log scale, and the conductivity distribution is forced to be smooth by adjusting α and β in equation 6.1 (damping of layer thickness is ignored in this case and the number of layers can be large). In the joint inversion, in addition to the layered model parameters, one additional parameter, static shift multiplier (see section 5.4 for details of static shift correction), which is needed to fit both the TEM and MT data with the same model is also inverted for.

6.1.2 1D MT/TEM joint inversion

Because of the tensor nature of the MT data, there are five possible parameters to be inverted for 1D inversion. These are:

- the rotational dependent apparent resistivity and phase (xy and yx modes)

- Determinant, given by the equation: $Z_{det} = \sqrt{Z_{xx}Z_{yy} - Z_{xy}Z_{yx}}$

- Arithmetic mean given by the equation: $Z_{ave} = \frac{Z_{xy} - Z_{yx}}{2}$

- Geometric mean given by the equation: $Z_{gme} = \sqrt{-Z_{xy}Z_{yx}}$

The last three are rotationally invariant while the xy and yx parameters are rotationally dependent. A plot of all of these five MT data parameters in terms of apparent resistivity and phase for sites 010 and 040 from Alid is shown in Figure 6.1. If the area is of a complicated resistivity structure as in Alid, then all the five parameters will generally give different resistivity models. It is hard to know which of these parameters is suitable for 1D inversion. However, based on model calculations for 2D and 3D models (Park and Livelybrook, 1989; Ranganayaki, 1984; Ingham, 1988) the determinant is commonly used. Regardless of the true dimensionality of the MT data, 1D inversion of the rotationally invariant, particularly the determinant data provides a good overview of the subsurface resistivity distribution. In this study the rotational invariant determinant apparent resistivity and phase were inverted to yield a 1D layered model for each site in the hope that this would provide a useful approximation to the 3D complex resistivity structures. 1D inversion of either the xy or yx modes would give different result.
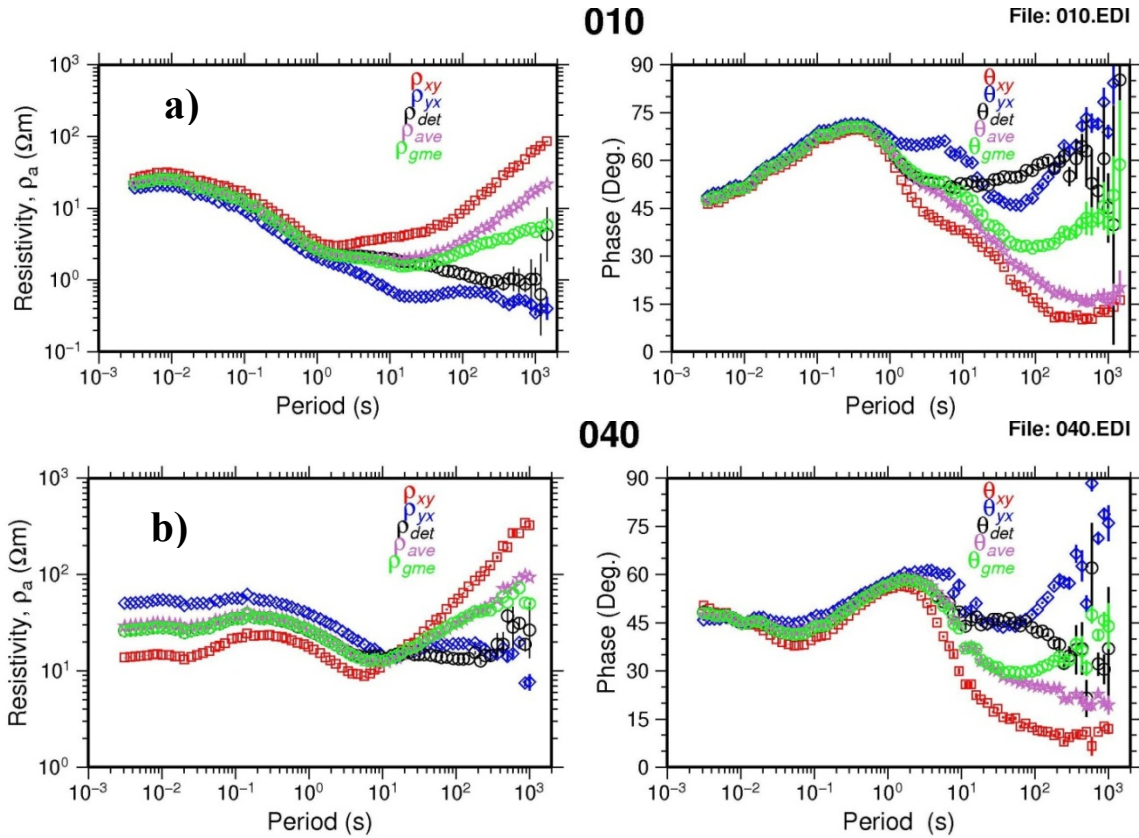
Figure 6.1. Apparent resistivity and phase of the five parameters derived from the impedances for sounding 010 (a) and sounding 040 (b).

As discussed in section 5.4, the apparent resistivities and phases (xy and yx modes) of the measured responses in Figure 6.1a for site 010, are observed to split apart for long periods (> 1 s). This splitting nature is an indication of a non-one dimensionality. But the splitting nature of the apparent resistivity modes (xy and yx) at site 040 (Figure 6.1b) for periods less than 1s is an indication of static shift (at least one of the modes is highly shifted); the two modes of the phases are not splitting at that period. This is because the phase curves are not affected by static shift.

To overcome the static shift problem as mentioned in the previous chapter, all the MT data were jointly inverted with TEM data from the same location (or at least within a few tens of meters). Figure 6.2 shows an example of jointly inverted TEM (sounding ALI080) and MT data (sounding 080). In this case the TEMTD determined static shift multiplier and the MT data were divided by the shift multiplier so that both the TEM and MT data could be fitted with the same 1D model shown to the right of the figure.
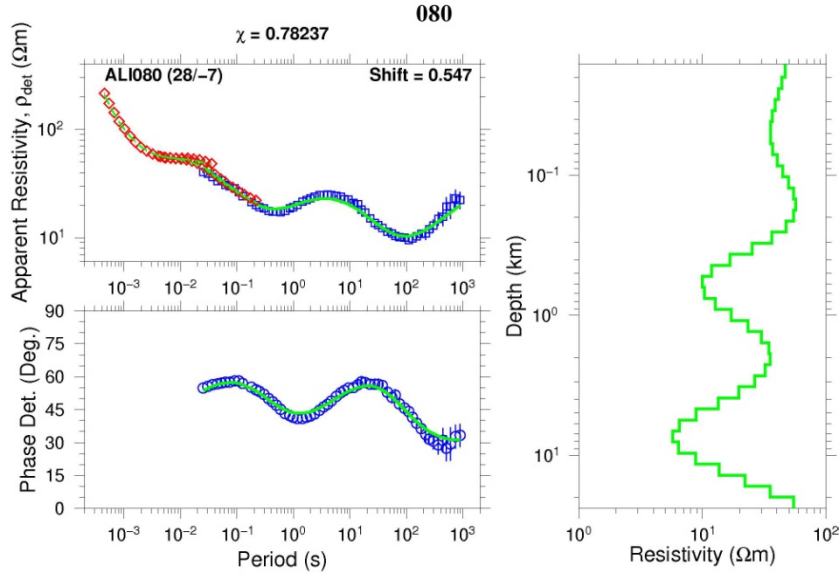
Figure 6.2. Result of 1D jointly inverted TEM and MT soundings for site 080. Red diamonds are TEM apparent resistivity, blue squares and circles are MT apparent resistivity and phase data, respectively derived from the determinant of the MT impedance tensor. Continuous green lines in the left panel are model response and the green curve in the right panel is 1D model result of the inversion. Number in the upper left panel: name of the TEM station Numbers in parenthesis in the upper left panel are distance between MT and TEM soundings and their elevation differences in meters. Number on the top of the figure: name of the MT station; number below the MT station: chi misfit; the static shift is shown in the upper right hand corner of the apparent resistivity panel. 1D models for the full data set are presented in appendix B.

Figure 6.3a shows histogram of static shift multipliers for all the MT soundings. Static shift ranges from 0.1 to 1.8; most of them are lower than one, majority being around 0.6. A shift of 0.1 means that the MT apparent resistivity is shifted down by an order of magnitude. If the data were interpreted without shift correction, then the model would yield 10 times too low resistivity value and about three times too shallow depths to resistivity boundaries as described in section 5.4. Figure 6.3b shows the spatial distribution of the shift multipliers for all the MT soundings in the Alid area. The distribution indicates that in some particular areas the MT apparent resistivity is consistently shifted down and in other areas shifted up. The static shifts are probably due to a combination of topography and near surface inhomogeneities. 1D MT/TEM jointly inverted curves are presented in Appendix B.
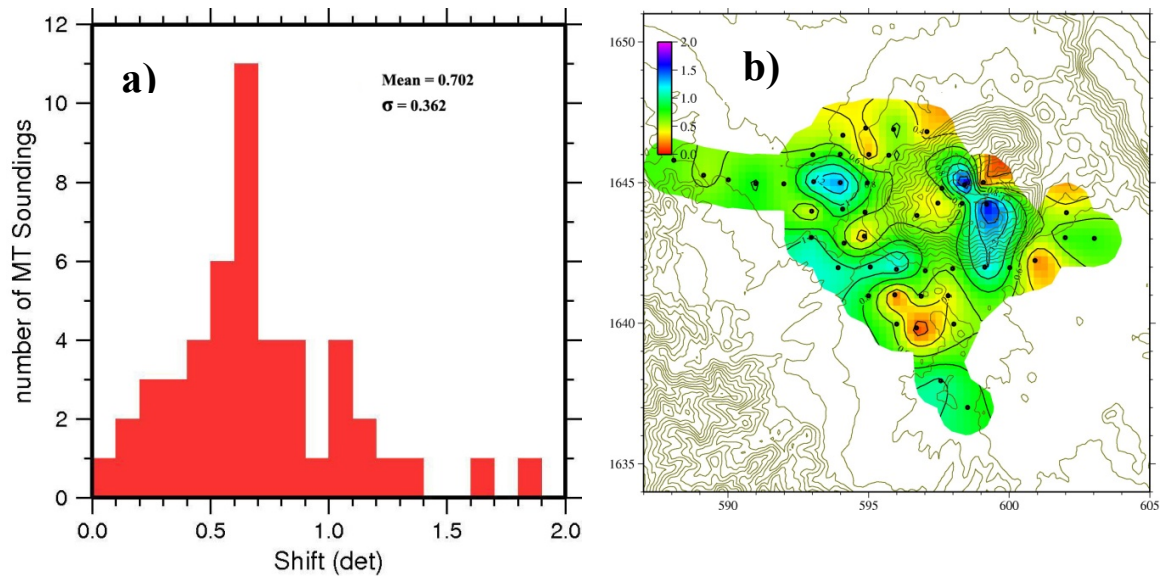
Figure 6.3. Histogram (a) and spatial distribution (b) of static shift parameter for the determinant apparent resistivity. Black dots on the figure to the right are MT stations, and Northing and Easting coordinates are in UTM units (km).

6.1.3 Results of 1D inversion

The result of the 1D Occam joint inversion of MT and TEM data shows resistivity variations only with depth for each sounding site. By combining the results of the individual soundings, a 3D view of the resistivity structure for the entire study area is formed. This subsurface resistivity structure is presented as iso-resistivity maps at different depths, as well as resistivity cross sections through the survey area. In addition, the results of the joint 1D inversion are also presented as 1D models for each sounding (Appendix B).

Iso-resistivity maps

Iso-resistivity maps show the resistivity distribution at different elevations. Iso-resistivity maps at 200, 550, 750, 1200, 2000, 3500, 4500, and 6000 m b.s.l. are presented in Figure (6.4a-h). The iso-resistivity map at 200 m b.s.l. shows low resistivity, as low as ~0.4 Ωm west and northwest of Mt. Alid. The low resistivity at this depth is elongated along the rift axis; in addition, low resistivity values (~1.6 Ωm) are also observed south of the mountain where only a few soundings are available. Below the mountain as well as, far west and south west of the mountain, higher resistivity is observed at this depth. At 550 m b.s.l. (Figure 6.4b), the low resistivity distribution to the west of the mountain has diminished considerably both in magnitude and in areal extent, localized to the northwest of the mountain with resistivity values of about 1 Ωm. While in the southern part of the mountain, the low resistivity is seen to broaden widely, meaning that the high resistivity observed southwest of the mountain at 200 m b.s.l. has disappeared completely. A high resistivity body is observed cutting Mt. Alid along its longest axis in SW-NE direction which is perpendicular to the rift axis and continues to appear to around 1.2 km depth.

At 750 m b.s.l. (Figure 6.4c) and down to 1200 m b.s.l. (Figure 6.4d), the low resistivity previously observed to the northwest of the mountain is disappearing, but the low resistivity body in the southern part of the mountain continues to exist with a clear SW-NE resistivity boundary. This resistivity boundary extends down to about 2000 m b.s.l. (the

50

general resistivity structure and the resistivity boundary is also outlined in the report of 1D inversion results made at ÍSOR, Eysteinsson et al., 2009). At 1200 m b.s.l. and further below, a low resistivity appears again to the northwest of the mountain, but the low resistivity observed south and southwest of the mountain continues to deeper levels. The reappearing of the low resistivity body to the northwest of the mountain is connected to the broader low resistivity to the south. Figure 6.4f (3500 m b.s.l.) shows a clear low resistivity body in NW-SE direction, parallel to the direction of the rift axis. The low resistivity body continues to deeper levels (Figures 6.4g and h) with a sharp resistivity boundary under the western part of the mountain. The low resistivity west of the mountain widens towards the centre of the mountain and a clear low resistivity region is observed on the western side of the mountain reaching resistivity values as low as ~ 0.2 Ωm.
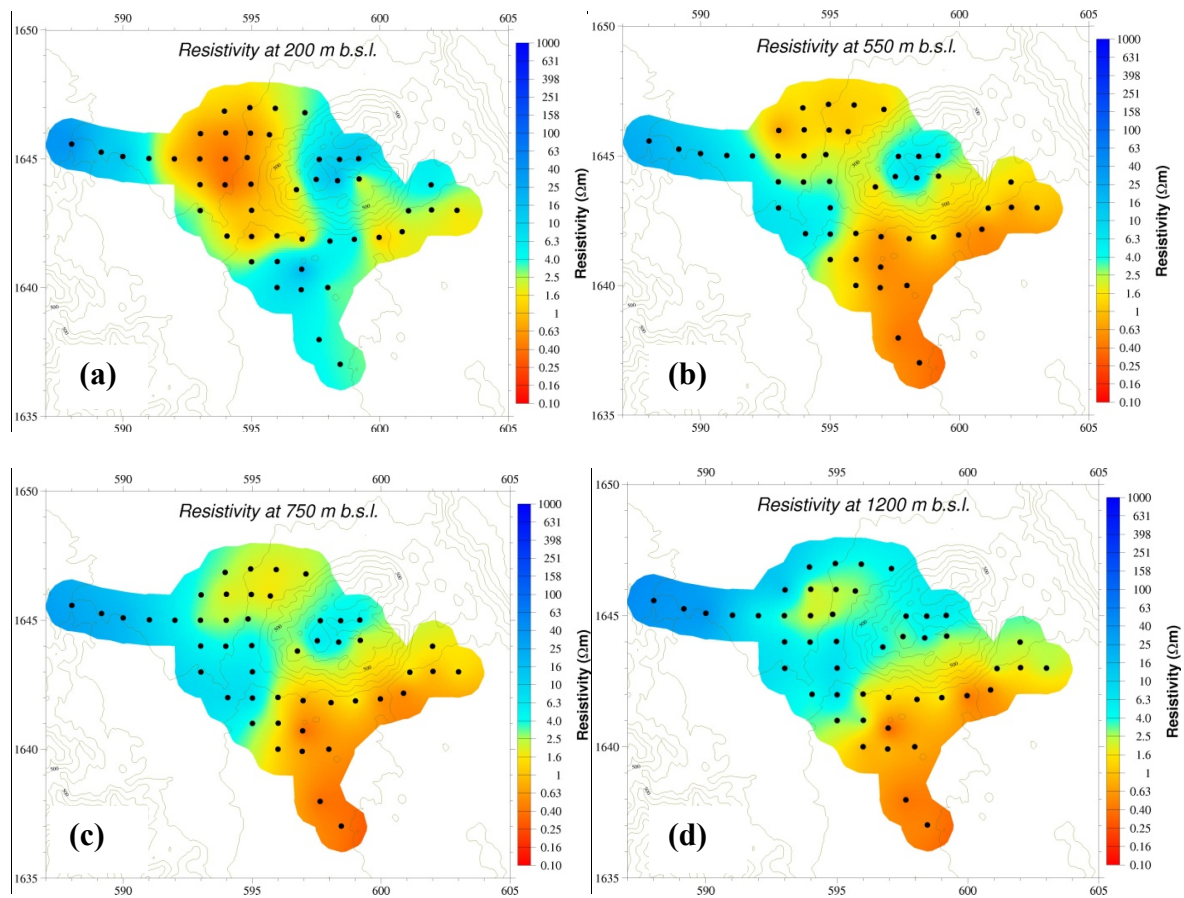

Figure 6.4. Resistivity maps at different depths. Black dots are MT soundings.
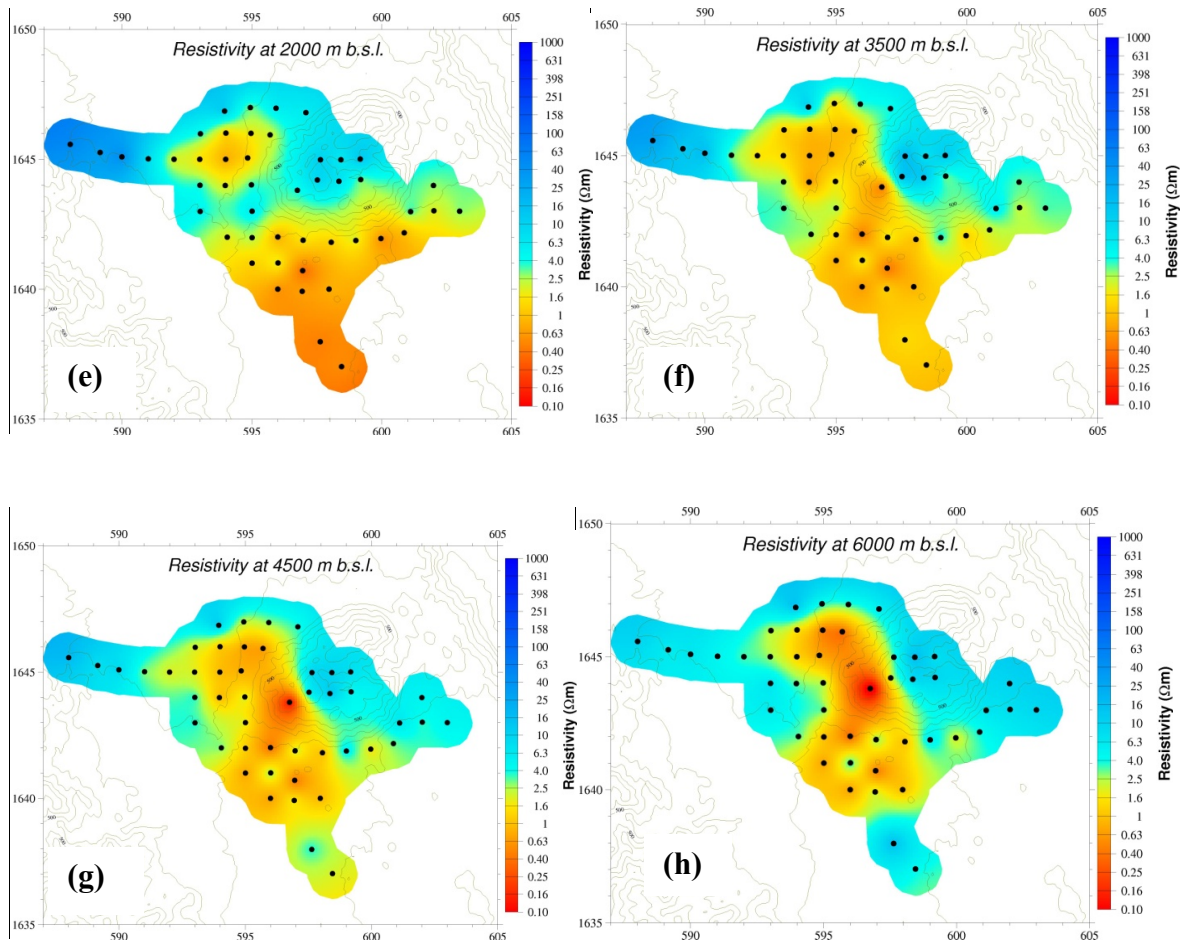
Figure 6.4. Continued.

Resistivity cross sections

Six vertical cross sections are presented in Figure 6.6 through 6.11; three cross sections are trending perpendicular to the rift axis (SW-NE direction), while the other three cross sections are trending parallel to the rift axis (SE-NW direction). The location of the cross sections is shown in Figure 6.5.

Cross section AC4000 presented in Figure 6.6 is perpendicular to the rift axis in the northern part of the survey area. The cross section shows mainly four resistivity layers. A thin high resistivity layer followed by a shallow conductor followed by a high resistivity layer and an underlying deeper conductor. No shallow conductor is seen in the southwest end of the cross section under sounding 078, or it is only very thin and slightly higher resistivity (~ 3.5 Ωm) is observed. The deeper conductor has also slightly higher resistivity (~ 2.5 Ωm) as compared to the central region. A sharp resistivity contact appears between sounding 008 and 009 from about 700 m b.s.l. and downwards. This sharp resistivity contact might be connected with the fractures running parallel to the rift axis which are probably covered by alluvium or it might be connected with lithological contacts. It is seen that the deeper conductor is connected to the shallow conductor through this sharp contact which presumably acts as a conduit.
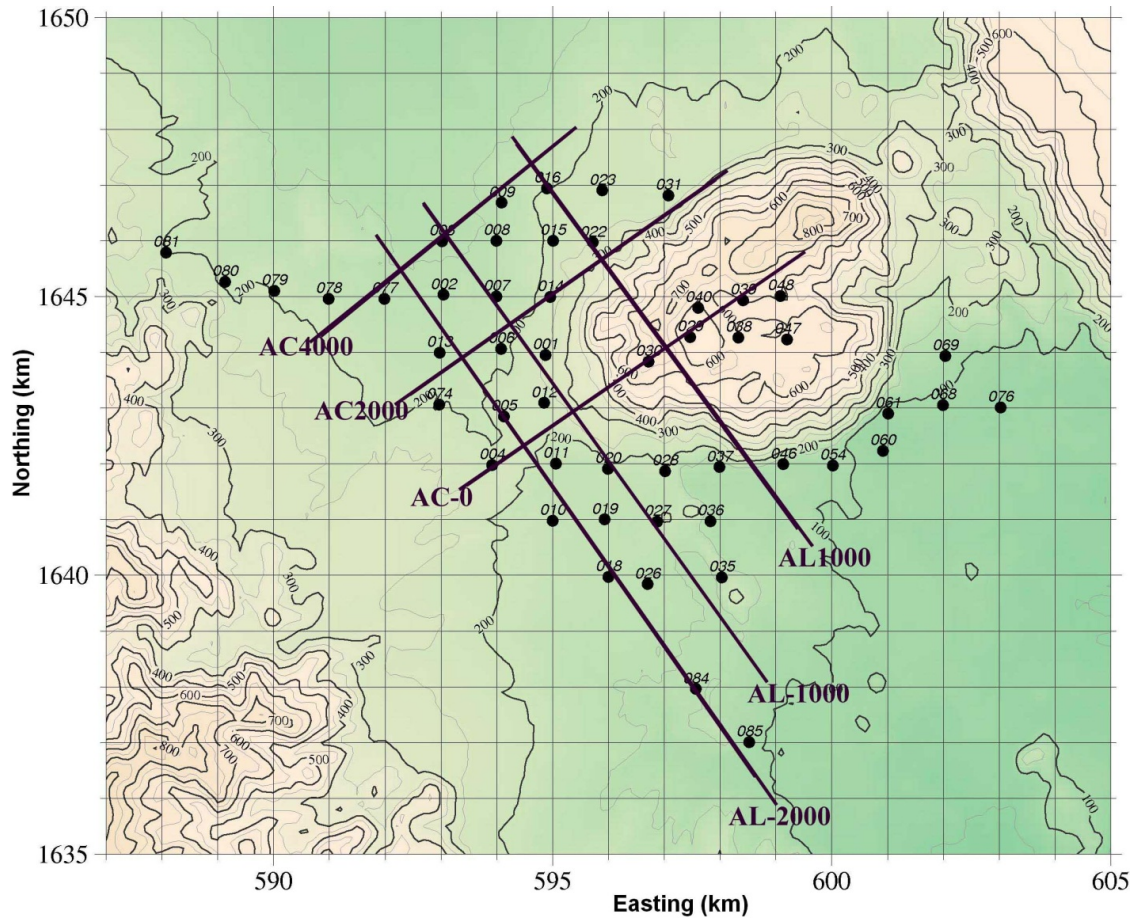
Figure 6.5. Location of profiles. AC in the names of the profile stands for across the rift and AL stands for along the rift. Black dots are MT soundings. Northing and Easting coordinates are in UTM units (km).

Cross section AC2000 in Figure 6.7 cuts the rift axis perpendicularly close to the foot of the mountain on its northwest side. The cross section shows a similar resistivity structure as cross section AC4000 but the deeper conductor is now wider particularly in the central part. No deep conductor is seen at the ends of the cross section.

Cross section AC-0 (Figure 6.8) cuts Mt. Alid. No low resistivity is observed beneath the mountain except for a sign of low resistivity at a depth of ~ 500 to 1600 m b.s.l. with resistivity values of ~ 3-4 Ωm. But a very conductive body (deep conductor) with a resistivity value of ~ 0.1 Ωm is observed below sounding 030, which is located in the south-western edge of the mountain. Here, there appears to be a resistivity contact between soundings 029 and 030. Southwest of sounding 029, the resistivity structure is similar to the four layer resistivity structure observed in the previous cross sections.
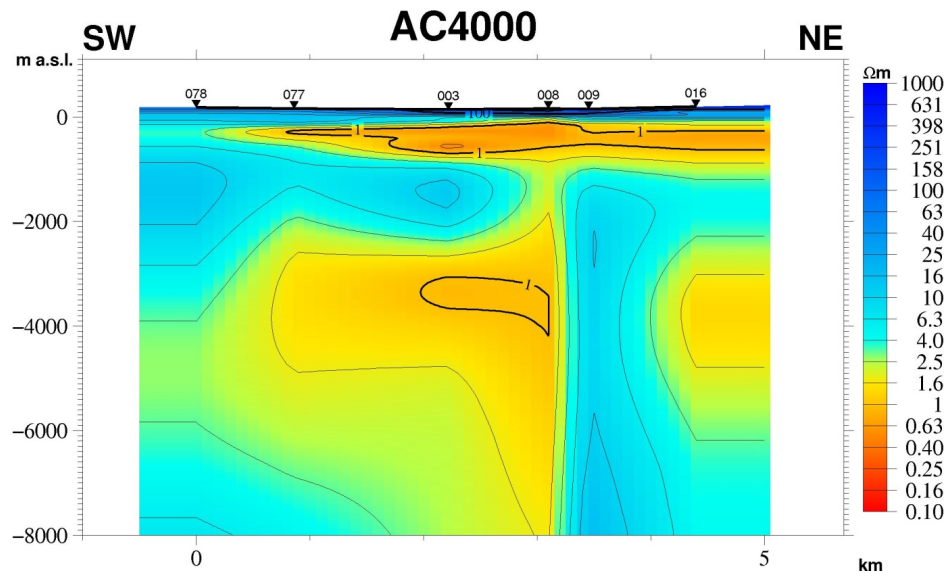
Figure 6.6. Compiled resistivity cross section AC4000, based on joint 1D inversion of TEM and MT data. Location is shown in Figure 6.5.
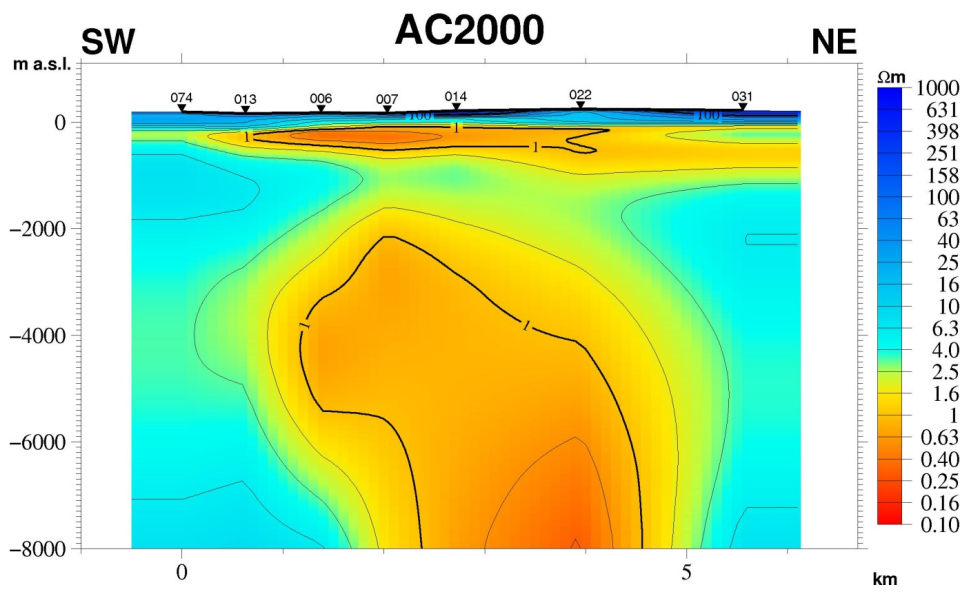

Figure 6.7. Compiled resistivity cross section AC2000, based on joint 1D inversion of TEM and MT data. Location is shown in Figure 6.5.
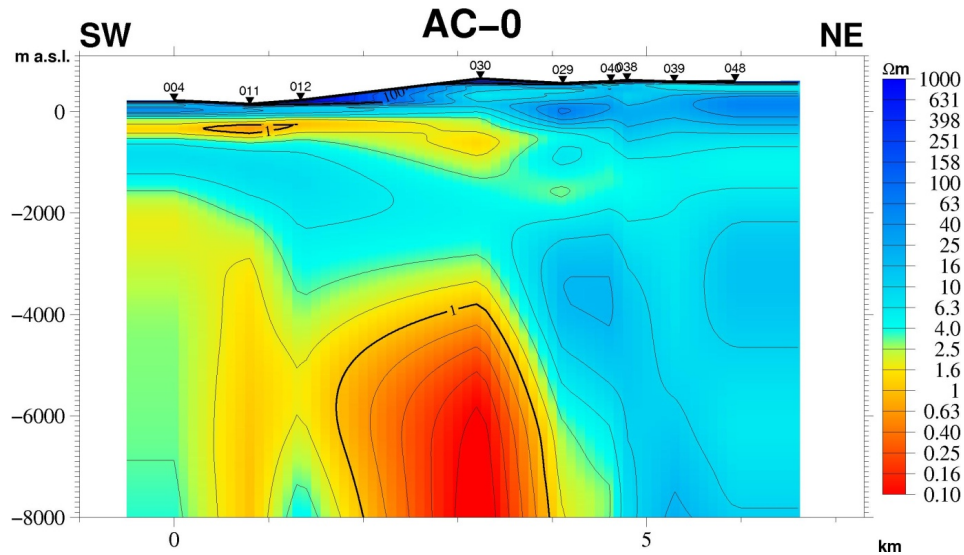
Figure 6.8. Compiled resistivity cross section AC-0, based on joint 1D inversion of TEM and MT data. Location is shown in Figure 6.5.

The resistivity cross sections oriented along the rift axis (SE-NW direction) are shown in Figure 6.9 through 6.11. The resistivity structures in the northern part of cross sections AL-2000 and AL-1000 (Figures 6.9 and 6.10) are similar to the general resistivity structures discussed above, showing a resistive top layer followed by conductive layer at shallow depth and then followed by higher resistivity layer which is underlain by a deeper conductor. While the southern part of the cross sections shows different resistivity structures. On the southern half of section AL-2000, three resistivity layers (the top resistive layer followed by a thick conductive layer which is underlain by a resistive layer) are observed. While, on the southern half of section AL-1000, only two resistivity layers (the top resistive layer followed by homogeneous conductive layer) are observed. The cross sections, AL-2000 and AL-1000 are located west of Mt. Alid. Cross section AL1000, (Figure 6.11), runs through the south-western part of Mt. Alid. There is a lack of sounding points through most of the central part of the section on which only sounding 030 is available at the centre of the section. This lack of soundings might have obscured the details of the resistivity structure, but generally the section shows the most common resistivity structure encountered in the other cross sections. Below sounding 030, a deeper conductor is observed with resistivity values of ~ 0.1 Ωm. All the three cross sections running along the rift axis show EW oriented vertical resistivity boundary.
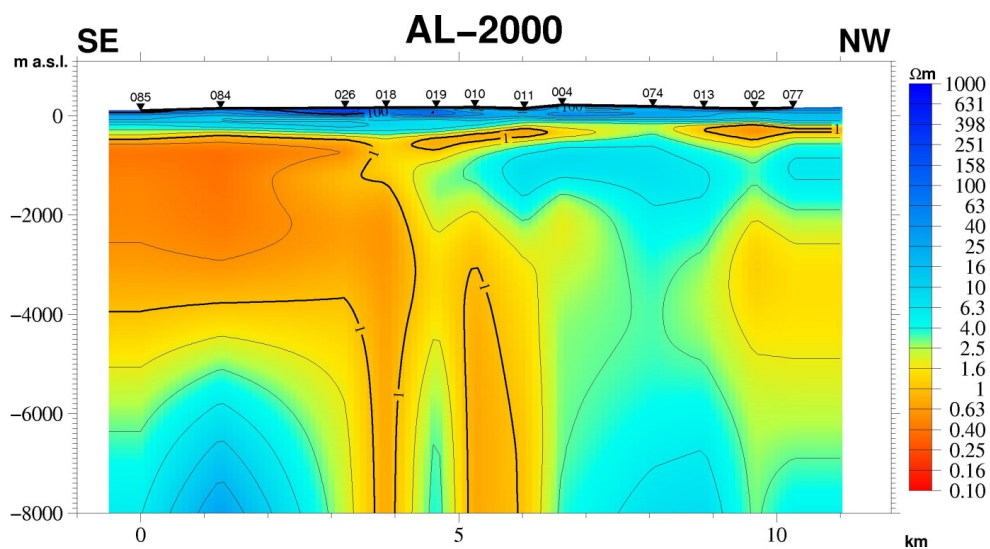
Figure 6.9. Compiled resistivity cross section AL-2000, based on joint 1D inversion of TEM and MT data. Location is shown in Figure 6.5.
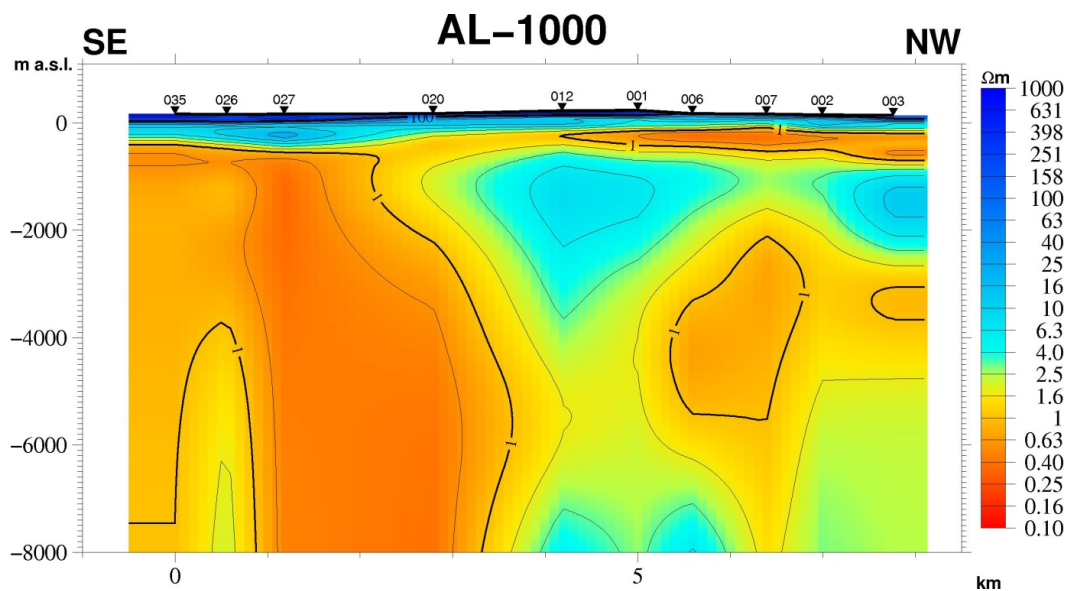

Figure 6.10. Compiled resistivity cross section AL-1000, based on joint 1D inversion of TEM and MT data. Location is shown in Figure 6.5.
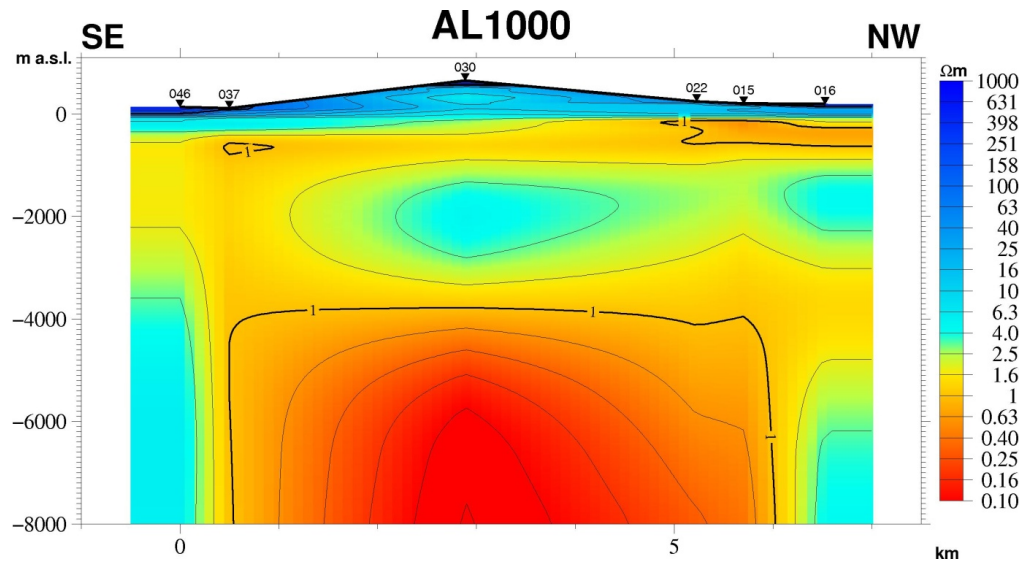
56

Figure 6.11. Compiled resistivity cross section AL1000, based on 1D inversion of TEM and MT data. Location is shown in Figure 6.5.

6.2 2D MT Data Inversion

The geological map in Figure 2.2 shows many structures (fractures and faults) running parallel to the rift direction (NNW-SSE). Moreover, a basic low resistivity anomaly more or less parallel to the rift direction (NW-SE) is revealed from the resulting models of 1D inversion from about 3.5 km depth downwards (see Figure 6.4g-h). The 1D modelling results, as described in section 6.1 showed a possible presence of a fault that runs roughly SW-NE, almost perpendicular to the rift axis (as indicated by the broken yellow line in Figure 6.13). A similar fault line is also indicated in the geological map (Figure 2.2) but the line trends more of WSW-ENE. Therefore, 2D modelling of the data for several profiles was done to see if the structures can be identified better.

As described in the preceding section, it is a common practice in 1D modelling to use some rotationally invariant property of the impedance tensor like the determinant. For 2D models the practice has been to invert for both the TE and TM data modes. According to Berdichevsky et al. (1998) both TE and TM mode should be used at various stages in the inversion process. This is contrary to what many other scientists do (Wannamaker et al., 1984, Boerner et al., 1999) who prefer simply to use the TM mode, because it is generally believed to be less influenced by 3D effects than the TE mode.

Here for the 2D inversion a code called REBOCC as described by Siripunvaraporn and Egbert (1999) is used.

6.2.1 Overview of REBOCC

REBOCC stands for **RE**duced **B**asis **OCC**am´s Inversion. The inversion is essentially a data-space variant of the Occam scheme of Constable et al. (1987) and deGroot-Hedlin and Constable (1990) (see Siripunvaraporn and Egbert, 2000). It seeks a minimum norm model subject to fitting data to within specified tolerance.

REBOCC can invert apparent resistivity (ρ_a) and phase (ϕ) of the TM and TE modes both independently and jointly, as well as the real ($\Re$) and imaginary ($\Im$) part of the vertical magnetic transfer function (tipper); that is, the ratio between the vertical magnetic field and the horizontal magnetic field (see equation 3.50). REBOCC is fast, stable (converges reliably), moderately memory demanding, easy to use and freely available for academic use.

The forward modelling is the core of the inversion and thus must be reliable, fast and accurate. It is used in two parts in the inversion; that is, to compute the sensitivity matrix and to compute the responses for calculating the misfit. Second order decoupled Maxwell´s equations are solved in the process; otherwise, first order coupled Maxwell´s equations would require a substantial computer memory (Mackie et al., 1994). Assuming the time dependence of exp(iωt), the second order Maxwell´s equations to be solved (from equation 3.14) are:

1) For the transverse electric (TE) mode in which the electric currents flow parallel to the strike of the 2D structure

$$\nabla \times \nabla \times \mathbf{E} = i\omega\mu\sigma\mathbf{E} \qquad\qquad 6.6$$

and

2) For the transverse electric (TM) mode in which the electric currents flow perpendicular to the strike of the 2D structure (see Figure 3.6 for both cases).

$$\nabla \times \nabla \times \mathbf{H} = i\omega\mu\sigma\mathbf{H} \qquad\qquad 6.7$$

REBOCC uses a finite difference (FD) method with TE and TM mode differential equations discretized as shown in Smith and Booker (1991). The discrete form of the differential equations can be expressed as $\mathbf{Ax}=\mathbf{b}$, where $\mathbf{b}$ is a vector which contains the terms associated with the unknown boundary values and source fields, and $\mathbf{x}$ is also a vector which represents the unknown interior fields ($\mathbf{E}$ for TE and $\mathbf{H}$ for TM). The matrix $\mathbf{A}$ is sparse and symmetric. The accuracy of the solution is mainly controlled by the quality of the mesh grid provided.

6.2.2 Model mesh grid design

The 2D mesh grid was designed based on basic rules described in Simpson and Bahr (2005). Different model mesh designs were made for the different cross sections considered in 2D inversion, each consisting of uniform half-space of 1 Ωm. Figure 6.12 shows an example of the mesh grid design used in 2D MT inversion for one of the profiles. The mesh contains 72 vertical and 40 horizontal grid planes with a total of 2880 cells of different sizes. In the centre of the mesh, the distance between grid planes is kept as dense as possible (200 m apart) and incremented on each side logarithmically. The block thickness in the z-direction increases gradually from 10 m on top to a maximum depth of 45 km.
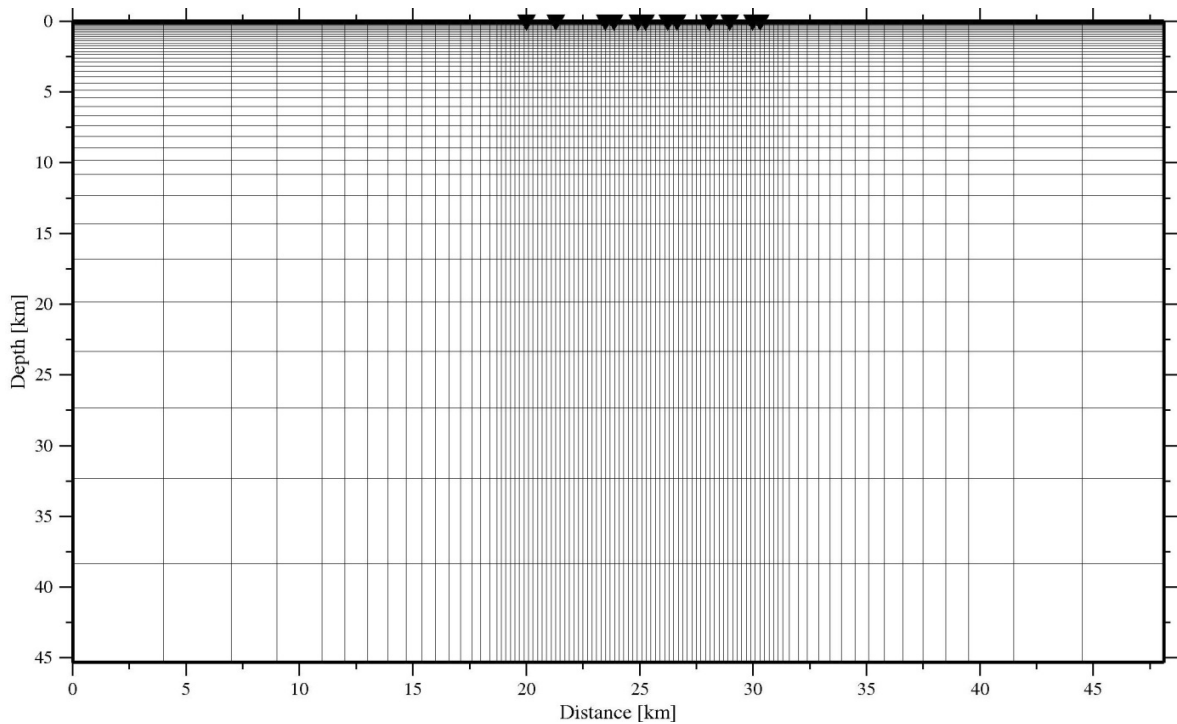
Figure 6.12. An example of a mesh grid design for 2D inversion using REBOCC. Black inverted triangles located on top within the denser part of the mesh gird are MT soundings projected onto the profile.

6.2.3 Inversion of the data

The data in the measured direction, xy (north-south) and yx (east-west) are rotated to the main regional geo-electric strike direction orienting the data into transverse electric (TE, electric field parallel to strike) mode and transverse magnetic (TM, electric field perpendicular to strike) mode. Regional geo-electric strike as described in section 5.3, is N35°W.

2D models were obtained by fitting the TE response and TM response data sets separately and the combined TM+TE responses for a total of four profiles (see Figure 6.13 for location). The 2D inversion was done by projecting the MT data onto each of the four profiles, containing 9, 10, 10 and 12 MT soundings each for 56 periods between 0.025 to 364 seconds. Three profiles are perpendicular to the geo-electrical strike which coincides with the regional geological strike (rift axis), in this case data were rotated N35°W and one profile parallel to the rift axis is taken to check the SW-NE running fault line observed in the geological map as well as from the results of the 1D inversion, in this case the data were rotated N55°E. To avoid unrealistic small errors in the data for the 2D approximation, error floors of 2% and 5% depending on the quality of the data were defined for both the apparent resistivity and phase. Prior to inversion, the MT data after rotation to the geo-electric strike were corrected for static shift by jointly inverting (both xy and yx modes) with TEM data from the same location or close by as described in section 5.4. To check for better convergence, various inversions with different starting models consisting of resistivity half spaces with various initial resistivities were tested. The best result was obtained by 1 Ωm half-space for the data.

The inversion was allowed to run for several iterations (mostly 20 iterations) and the final models were attained after many iterations (in some cases only 6 iterations were needed to reach the best fit) for the different modes and profiles with different rms (root mean square) values (shown under each models in Figures 6.14 – 6.17). Almost all the inversions provided models with relatively good data fit. Figure 6.18 shows pseudo-sections of the observed data and model response for one profile; and fit of the measured and response for the full data set is shown in Appendix C.
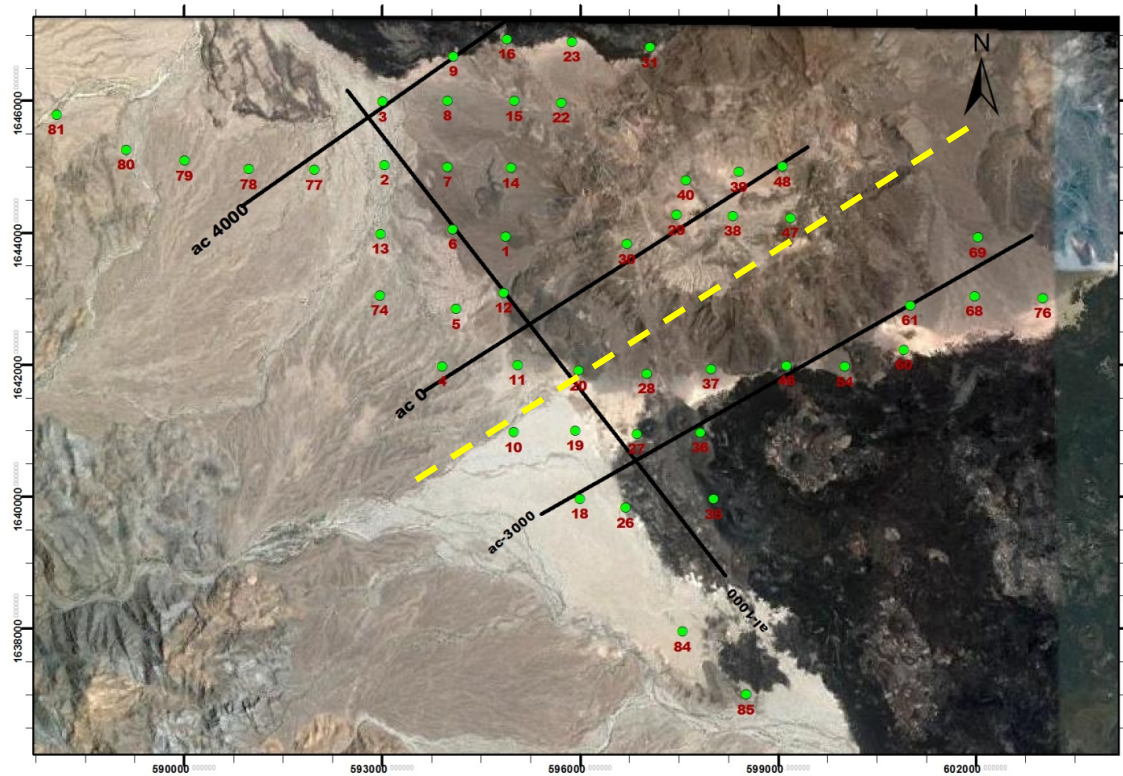

Figure 6.13. Location of the four profiles used in the 2D inversion. Green dots are all MT soundings in the survey area. The background picture is satellite image taken from Google Earth. On the profiles, ac stands for across the rift axis and al stands for along the rift axis. Broken yellow line is fault line inferred from the results of 1D inversion.

6.2.4 Results of 2D inversion

The final model results of the 2D inversion are shown in Figures 6.14 – 6.17 for the three profiles running perpendicular to the rift axis and the one along the rift axis. Three inversion options are given: TM mode inversion alone (Figure 6.14A, 6.15A, 6.16A and 6.17A), TE mode inversion alone (Figure 6.14B, 6.15B, 6.16B and 6.17B) and joint inversion of TM+TE modes (Figures 6.14C, 6.15C, 6.16C and 6.17C). The structure below the survey area is highly 3D; thus, the electric and magnetic field do not decouple into two modes nicely which would be expected to provide more reasonable approximation to the fault lines and rift fractures as well as the resistivity distribution. According to several 2D inversion of synthetic MT data (e.g. Pedersen et al., 2005; Lemma, 2010), generally the TE mode couples well to the conductor, whereas the TM mode couples better to the resistor. Joint inversion of both TM+TE modes gives then best model results (Pedersen et al., 2005).

60

Two different best fitting models are obtained from the TM and TE modes. The difference between the two is attributed to the fact that TM and TE modes respond differently to certain conductivities. It is observed that the models obtained from the TE modes (Figures 6.14B, 6.15B and 6.16B) provide very poor estimates of the deep conductor which possibly extends to deeper depths. Therefore, more emphasis will be given to the TM mode in this discussion as it is less influenced by 3D effects than the TE mode, but valuable information can also be gained from the TE mode.

The general resistivity structure is more or less similar to the models of the 1D inversion results discussed in section 6.1.3. All the profiles in both modes and their joint models, except on top of the mountain, show a thin high resistivity shallow layer which might be associated with the cold, unaltered fresh basaltic lava and the porous alluvium which covers most of the area. Under most of the sounding sites located on top of the mountain, a relatively conductive layer is observed reaching to the ground surface. This low resistive shallow layer on the top of the mountain seems to be in good agreement with the highly altered ground surface accompanied by other geothermal manifestations such as fumaroles, hot springs and steaming or hot ground observed in abundance.

The TM mode shows a deeper conductor from about 1 km down to about 4-7 km with resistivity values of approximately 0.1 Ωm in the three profiles perpendicular to the rift (Figure 6.14-6.16). The wide conductor zone below the mountain in Figure 6.15A from TM mode is not seen in the 1D inversion, but all the MT data on top of the mountain show a highly three-dimensional nature for long periods. This wide conductor zone might be assumed to be an artifact of the inversion but when it was compared with results of 3D inversion at deeper levels, about 2-4 km (section 6.3), its presence is somehow supported. The sharp resistivity contact which was observed from the 1D inversion between sounding 008 and 009 in Figure 6.6 is also clearly observed here in the TM mode of the 2D inversion (Figure 14A) from about 700 m b.s.l. downwards.

The cross section south of the mountain (ac-3000 in Figure 6.16) shows four zones of conductive bodies in both the TM and TE modes as well as in the inversion of both modes along the profile. These low resistivity zones are seen more clearly in the TE mode (Figure 6.16B). A careful look at the satellite image (Figure 6.13) and the geological map on Figure 2, reveals that these four zones of conductive bodies are directly related to the big fractures running parallel to the rift axis. Therefore, these fractures zones could be the main feeders of the lava flows and geothermal activities.

Figure 6.17 shows the cross section running parallel to the rift axis (al-1000 on Figure 6.13). This cross section was taken to check the SW-NE running fault line (broken yellow line in Figure 6.13), as inferred from the results of the 1D inversion or a fault line as indicated in the geological map. Because the main geo-electric strike is trending N35°W, rotating the data to the approximate strike direction of the fault line, which is N55°E, do not decouple into the appropriate modes (TE mode has now the electric field parallel to the suspected fault line and TM mode, the electric field is perpendicular to the fault line). The main geo-electric strike (rift axis) is still the major influencing feature of the data; as a result, the resulting models for TM and TE modes are reversed. The TE mode now could image the conductor to deeper levels nicely, while the TM mode only to shallow levels. TE mode (Figure 6.17b) shows the existence of the resistive body seen in the 1D resulting models (section 6.1) with a sharp vertical resistivity boundary which was inferred as fault line and extends from about 0.5 to 2 km depth.

Figure 6.14. Resulting models of 2D inversion for profile ac4000. TM mode inverted separately, RMS=4.2 obtained after 11 iterations (A). TE mode inverted separately, RMS=2.5 obtained after 13 iterations (B) and TM+TE joint inversion, RMS= 5.1 obtained after 6 iterations (C). For location of the profile, see Figure 6.13.

tmte_ac4000

Figure 6.14. continued.

tm_ac−0

Figure 6.15. Resulting models of 2D inversion for profile ac-0. TM mode inverted separately, RMS= 4.5 obtained after 7 iterations (A). TE mode inverted separately, RMS= 4.9 obtained after 16 iterations (B) and TM+TE joint inversion, RMS= 7.5 obtained after 13 iterations (C). For location of the profile, see Figure 6.13.
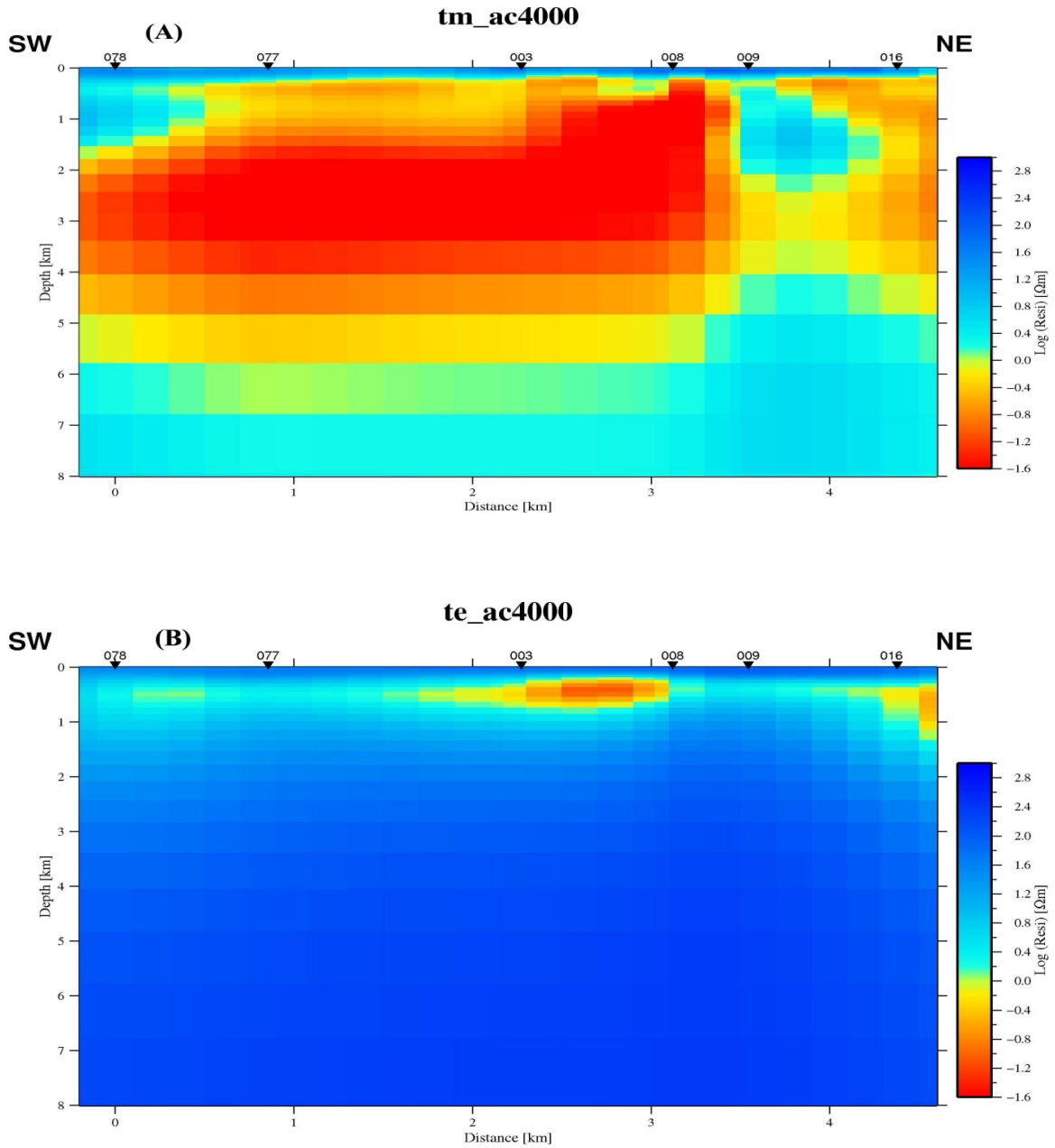
63
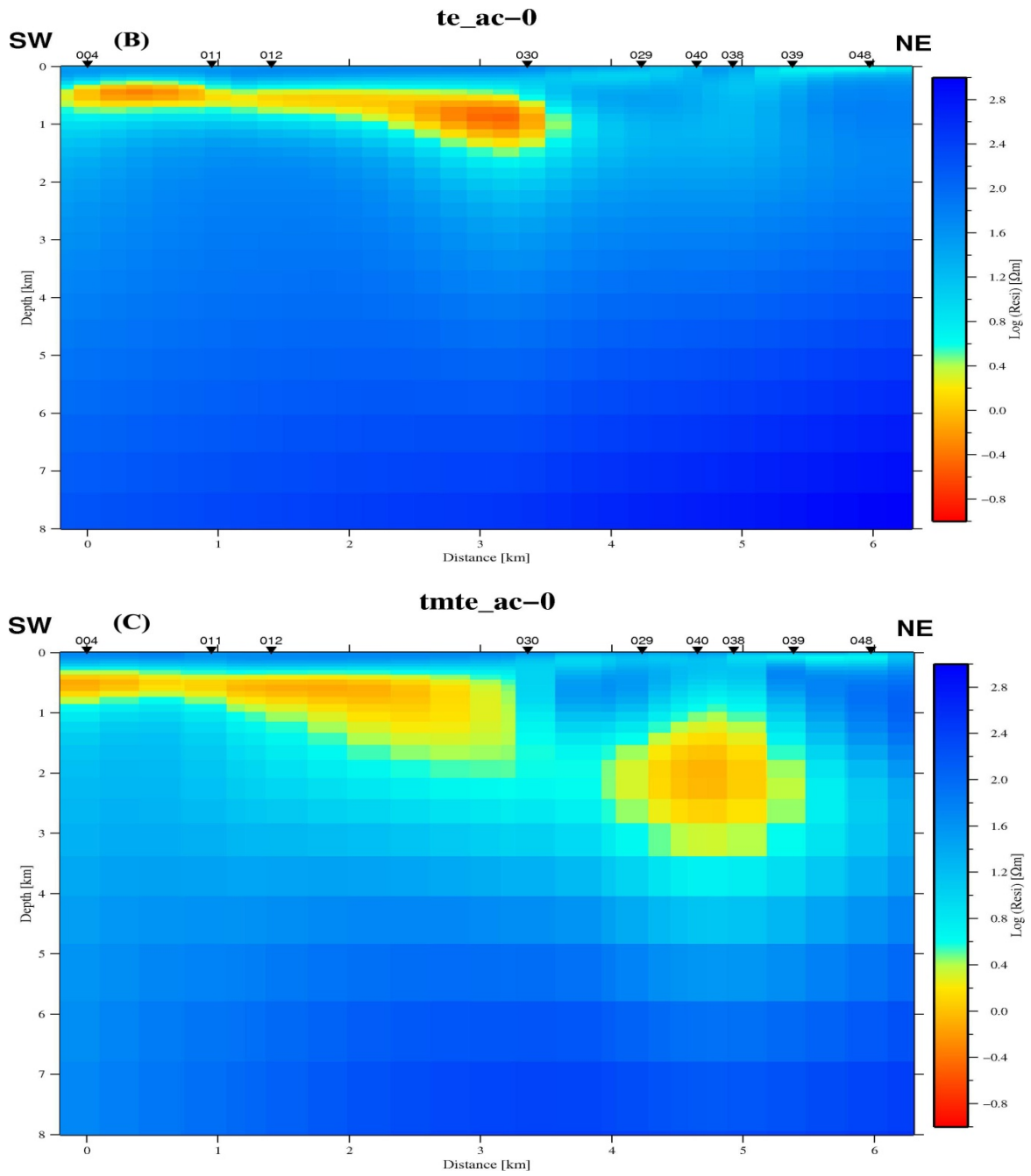
Figure 6.15. Continued.
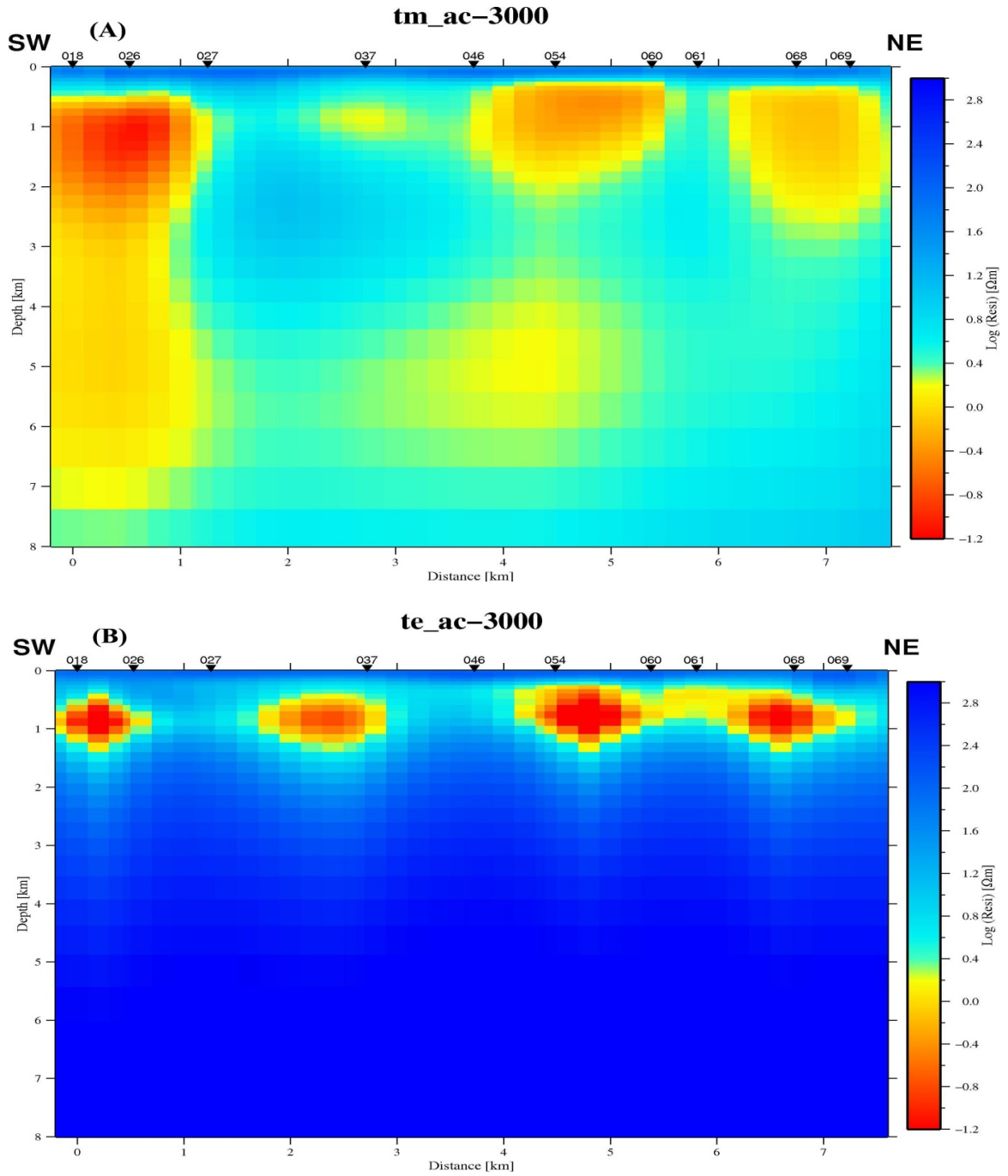
Figure 6.16. Resulting models of 2D inversion for profile ac-3000. TM mode inverted separately, RMS= 3.9 obtained after 13 iterations (A). TE mode inverted separately, RMS= 4.1 obtained after 10 iterations (B) and TM+TE joint inversion, RMS= 4.5 obtained after 14 iterations (C). For location of the profile, see Figure 6.13.
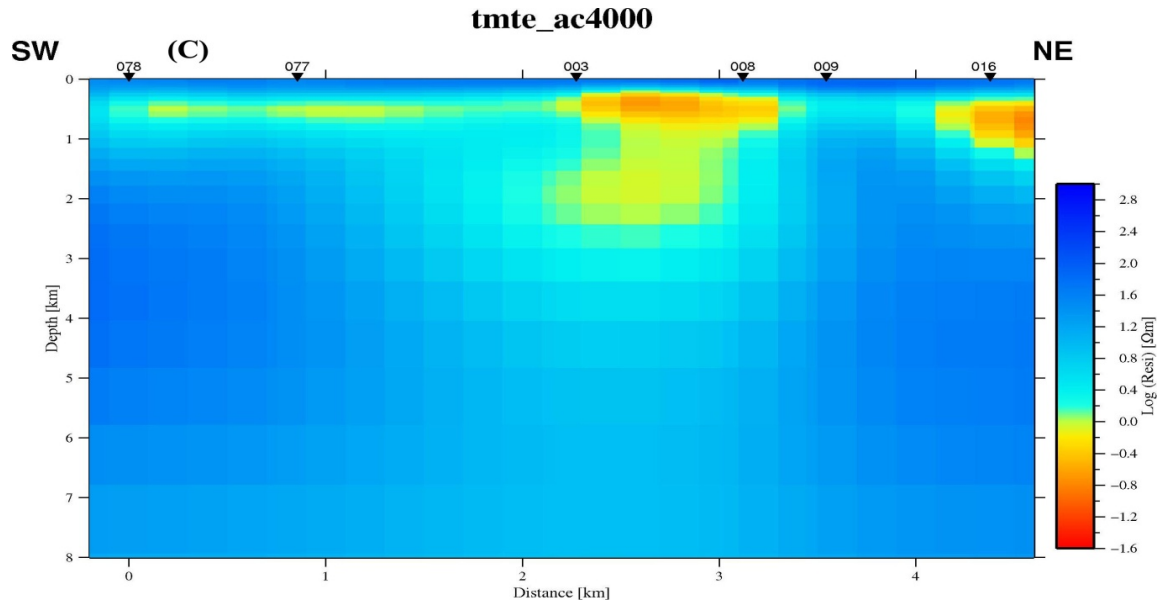
tmte_ac−3000
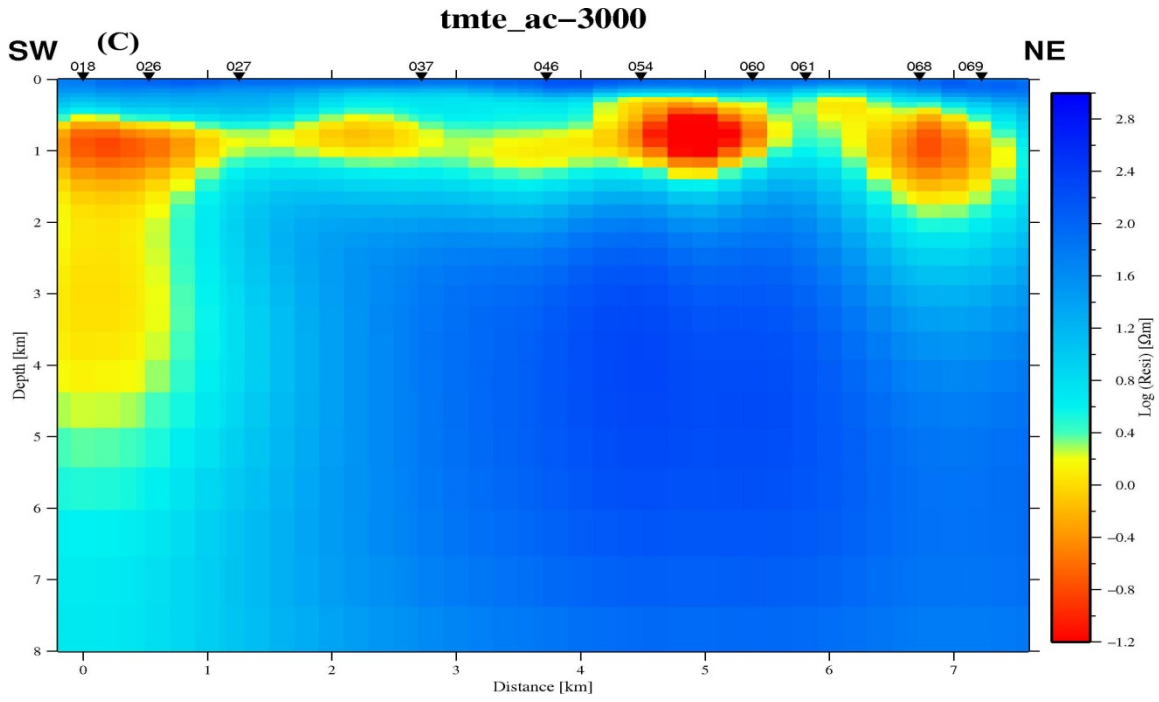
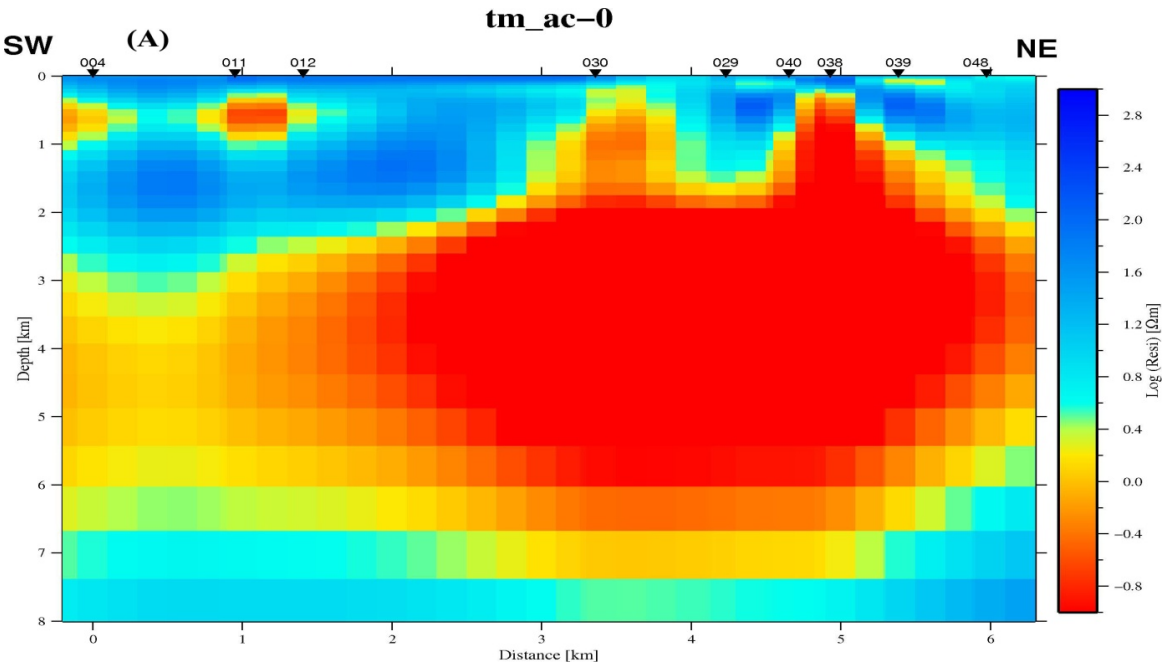*Figure 6.16. Continued.*
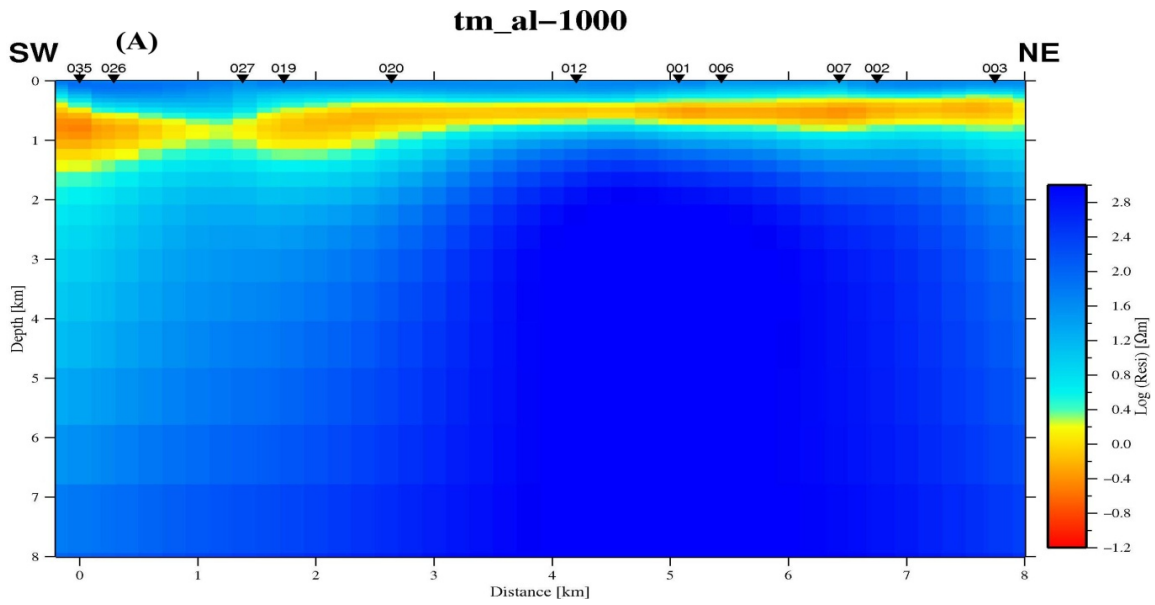
tm_al−1000

Figure 6.17. Resulting models of 2D inversion for profile al-1000. TM mode inverted separately, RMS= 2.8 obtained after 11 iterations (A). TE mode inverted separately, RMS= 4.5 obtained after 15 iterations (B) and TM+TE joint inversion, RMS= 4.4 obtained after 15 iterations (C). For location of the profile, see Figure 6.13.

te_al−1000

tmte_al−1000
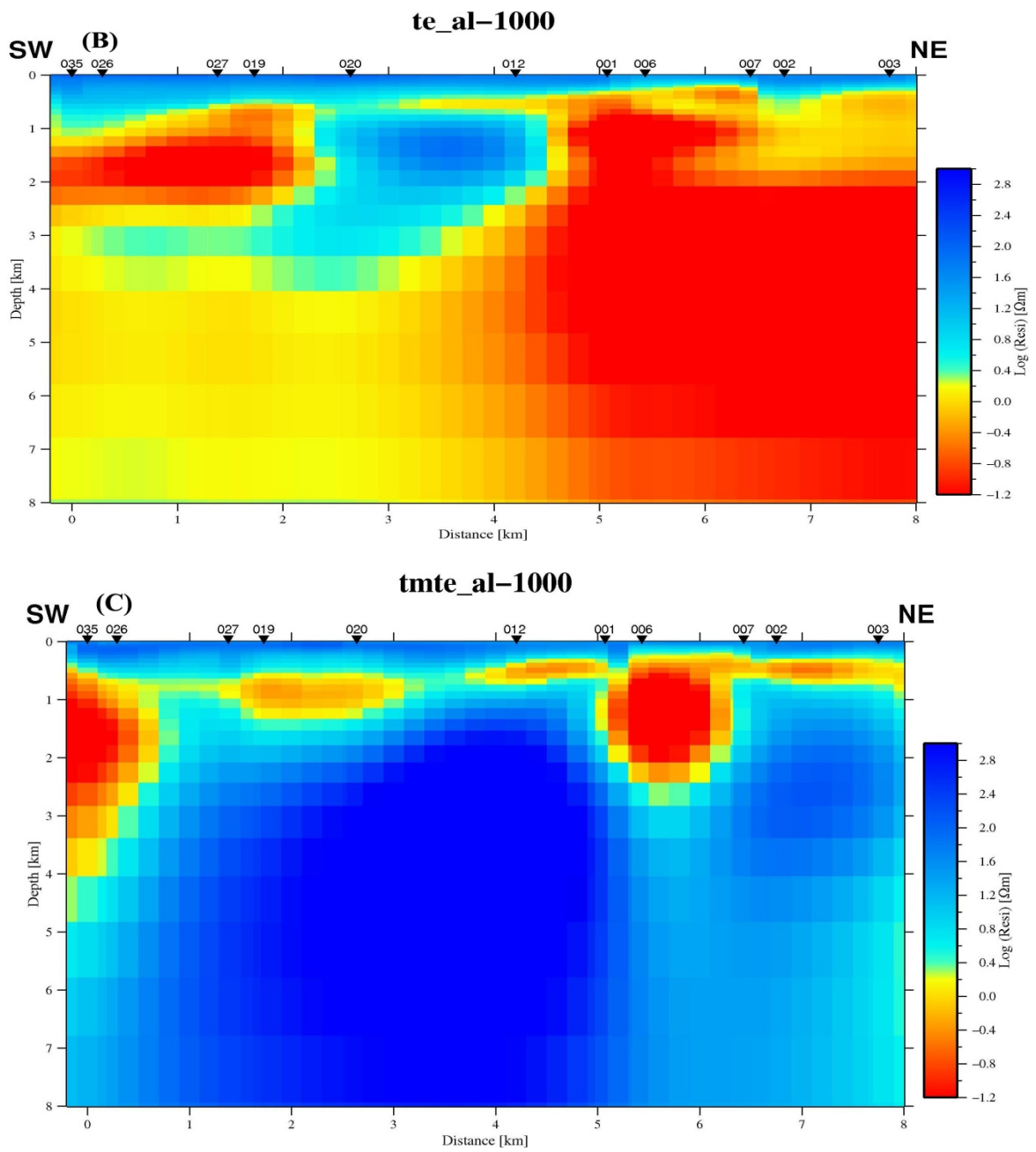
Figure 6.17. Continued.
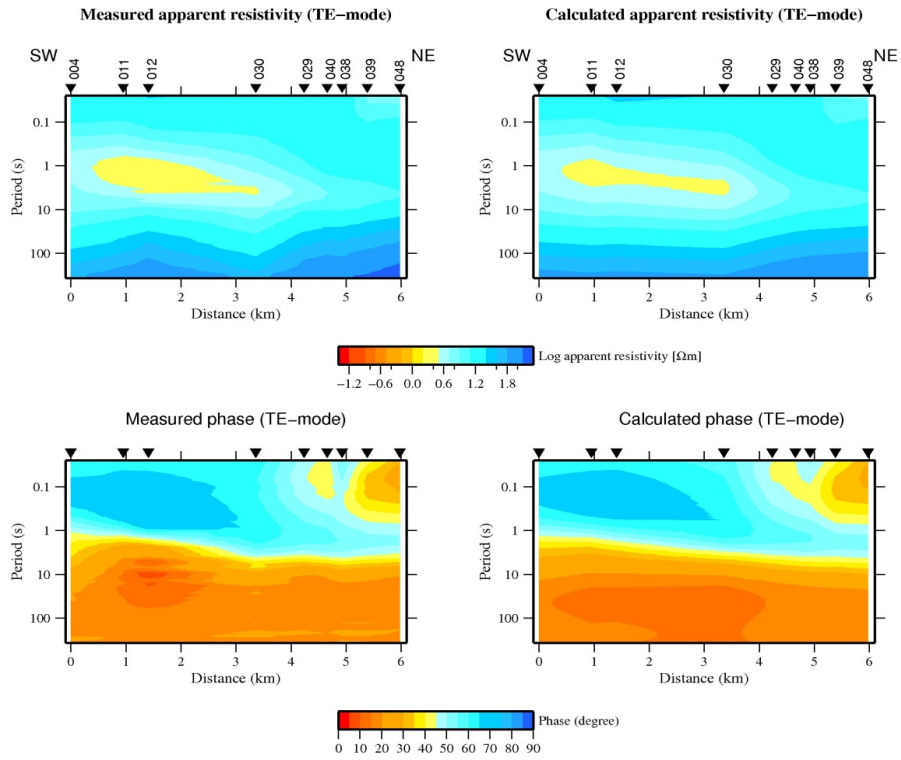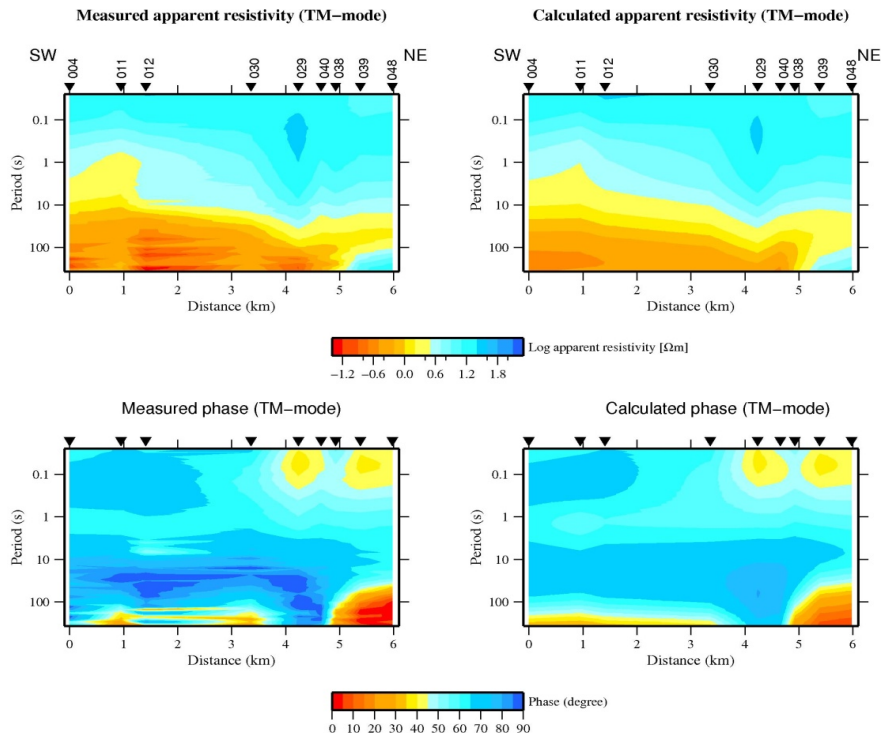
Figure 6.18. Pseudo-sections of the measured data (left) and the calculated data (right) showing the apparent resistivity and phase for profile ac-0 for both TE (a) and TM (b) modes inverted separately. The RMS for TM mode is 4.5 and for TE mode it is 4.9.

6.3 3D MT data inversion

According to the dimensionality analysis (section 5.1), the dimensional indicators of the impedance tensor of the MT data indicate that the resistivity structure is highly three dimensional or at least non-1D nature for long periods, greater than 1s.

MT soundings are tensor data and each sounding contains information on the vertical and lateral resistivity variations. Unlike 1D inversion which assumes that resistivity varies only with depth (vertical direction) and 2D inversion which assumes that resistivity varies with depth and in one lateral direction, 3D inversion assumes resistivity to vary in all three directions. 3D inversion is used to construct the model that fits the inductive responses produced by the regional conductivity structure. In addition, 3D inversion can be used to fit the inductive effects due to localized near surface structures both directly beneath and outside the region.

The drawback of 3D inversion is the large computational cost in terms of both memory and CPU time. A 3D MT inversion code called WSINV3DMT (version 1.1.0, Siripunvaraporn et al., 2005) which formulates the inversion problem in the data space rather than in the model space was used for this study.

6.3.1 Overview of WSINV3DMT

WSINV3DMT (Siripunvaraporn et al., 2005) is a full 3D inversion programme for Magnetotelluric data. The inversion algorithm is an extension of the 2D data space Occam inversion (Siripunvaraporn and Egbert, 1999). The inversion seeks the smoothest minimum structure model subject to an appropriate fit to the data.

The original Occam inversion was introduced by Constable et al. (1987) for 1D MT data. It was later expanded to 2D MT data by deGroot-Hedlin and Constable (1990). Occam inversion is stable and converges to an acceptable misfit in relatively small number of iterations, compared to most other methods. They both are based on the model space method (Siripunvaraporn et al., 2006). Computational costs associated with construction and inversion of model space matrices make a model space Occam approach to 3D MT inversion impractical because all computations depend on the number of the model parameter, M (Siripunvaraporn et al., 2006).

These difficulties can be overcome with a data-space approach, where matrix dimensions depend on the size of the data set N, rather than the number of model parameters M (Siripunvaraporn et al., 2006). Generally, N << M for MT data, here the data parameter size N is the total size of the data values which is the product of the number of periods Np, the number of stations Ns, and the number of responses Nr (maximum is 8 for all impedances and 4 for only off-diagonal impedances) while the model parameter M is the total number of discretization blocks which is a product of number of discretization in x (north-south) Mx, number of discretization in y (east-west) My, and number of discretization in z (vertical) Mz. As discussed in Siripunvaraporn and Egbert (2000) the transformation of the inverse problem to the data space can significantly improve the computational efficiency for the 2D MT problem. The WSINV3DMT inversion code is based on the data space approach (Siripunvaraporn et al., 2005). With the transformation to data space the computational costs (i.e. CPU time and RAM required) are significantly reduced making the 3D inversion practical for PCs.

6.3.2 3D grid mesh and initial models

In 3D inversion, forward modelling solutions depend significantly on the mesh discretization which has a considerable effect on the inversion results. Due to a big memory demand, there is a trade-off between the sizes of the model grid (numbers of x, y and z). Choosing small blocks is preferred for accuracy but the total number of blocks should be kept as small as possible (optimum) so that a solution can be obtained in a reasonable time (Pellerin et al., 1996; Siripunvaraporn et al., 2002)

The number of vertical grid planes from south to north is 39, from west to east 39 and the number of horizontal layers is 28 (without air layers); therefore, the total number of model cells is M = 39 × 39 × 28 = 42588. The horizontal grid spacing of the denser sections of the model (i.e. the central part of the model) are 1 km to ±8.5 km from the centre in both x- and y-directions and then progressively increasing in size to ±110.5 km. The first layer in z direction is 50 m thick, and the next four layers are 60, 70, 80 and 100 meters, down to 360 meter. Below that, the block sizes were increased by 1.3 times the overlaying layer thickness down to 70 km depth.

The actual locations of the MT soundings are shown as blue points in Figure 6.19. The programme requires that the soundings are at the centre of the grid cells and the MT data were slightly adjusted so that they can be at the centre of the grid cells (red diamonds at the centre of the grid cells).

To see how the mesh grid design affects the final model result, three mesh grids were tested being different in the vertical direction. The first mesh grid is coarse with dimensions 39 x 39 x 23 in the x, y and z directions, the second is relatively fine with dimensions 39 x 39 x 28 and the third mesh was even finer with 32 layers in the vertical direction. The three mesh grids were tested with an initial model of five layers with resistivity values of 200, 10, 50, 5 and 50 Ωm. The fit between the measured data and response of the inversion results from the three different mesh grids were compared and the mesh grid with dimensions of 39 x 39 x 28 was found to be the most appropriate to use.

Two types of initial models were tested using the mesh grid with dimensions 39 x 39 x 28: a homogeneous half space and a layered earth. First a homogeneous half space with a resistivity value of 50 Ωm was tested and then another half space with a resistivity value of 100 Ωm to see which half space gave the best fit. The model fit with 100 Ωm half space was better when fit between the measured data and responses of the inversion results were compared. The model fit with a 100 Ωm half space was then compared with the layered earth model of resistivity values: 200, 10, 50, 5 and 50 Ωm. A better model fit was obtained with the half space for the first run, but at the subsequent runs done with the best model as initial model, the final resulting best fit model was obtained from the layered earth model for these data.

The 3D initial model of Alid MT data for this study was therefore taken as a layered earth model consisting of five layers with resistivity values 200, 10, 50, 5 and 50 Ωm (Figure 6.19). These layered resistivity values are an approximate from the results of the 1D inversion. A horizontal slice through the grid of the central dense section and the initial model for the inversion are shown in Figure 6.19. The model directions are defined as follows: the x-axis is in the N35°W-S35°E direction with N35°W positive, the y-axis in the S55°W-N55°E direction with N55°E positive and the z-axis positive downwards. In the

plane view, the origin of the internal coordinate system of the model is at the centre of the surface of the grid mesh and shown with a black circle in Figure 6.19.
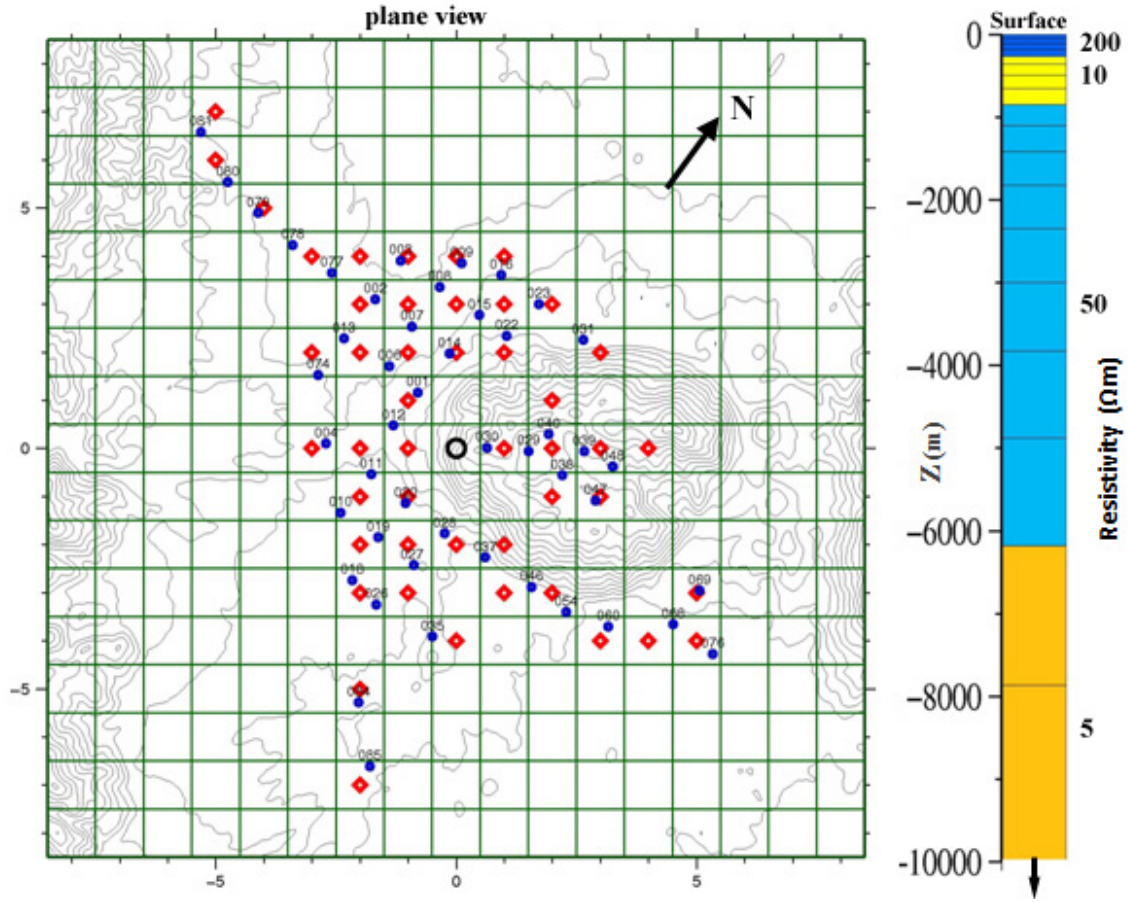

Figure 6.19. Plane grid (left) showing location of MT soundings (blue circles) in the central part of the 3D mode grid (grid coordinates are in km), and an initial layered model for the inversion (right). The dimensions of the central grid squares are 1 km x 1 km and the MT sites are slightly adjusted so that they are at the centre of the squares (red diamonds) as required by the inversion code.

6.3.3 Static shift correction of MT tensor data

3D inversion was performed for the MT impedance tensor; as a result a static shift correction for the MT impedance elements was needed. In the static shift, it is assumed that the shifts are mainly due to distortion of the electric fields. If S_{xy} and S_{yx} are the shift multipliers for the xy and yx apparent resistivities respectively, the corrected tensor $\mathbf{Z}^c$ is given by the following formula (Árnason et al., 2010):

$$\begin{bmatrix} Z_{xx}^c & Z_{xy}^c \\ Z_{yx}^c & Z_{yy}^c \end{bmatrix} = \begin{bmatrix} C_x & 0 \\ 0 & C_y \end{bmatrix} \begin{bmatrix} Z_{xx} & Z_{xy} \\ Z_{yx} & Z_{yy} \end{bmatrix}; \text{ where } C_x = \sqrt{\frac{1}{S_{xy}}}; \ C_y = \sqrt{\frac{1}{S_{yx}}}$$

From the MT data strike direction analysis in section 5.3, and from the geological structures (Figure 2.2), the general geo-electric strike of data is assumed to be N35°W.

Therefore, due to the expected influence of the structures, all the data were rotated so that the x-axis is parallel to the geo-electric strike. After rotation, all the MT data were jointly inverted with the TEM data from nearby location both for xy and yx modes and the shift parameters, S_{xy} and S_{yx} determined. Those parameters were then applied to the impedance tensor elements. An example of MT/TEM joint inversion of both the xy and yx modes is shown in Figure 6.20, where $S_{xy} = 0.956$ and $S_{yx} = 0.361$.
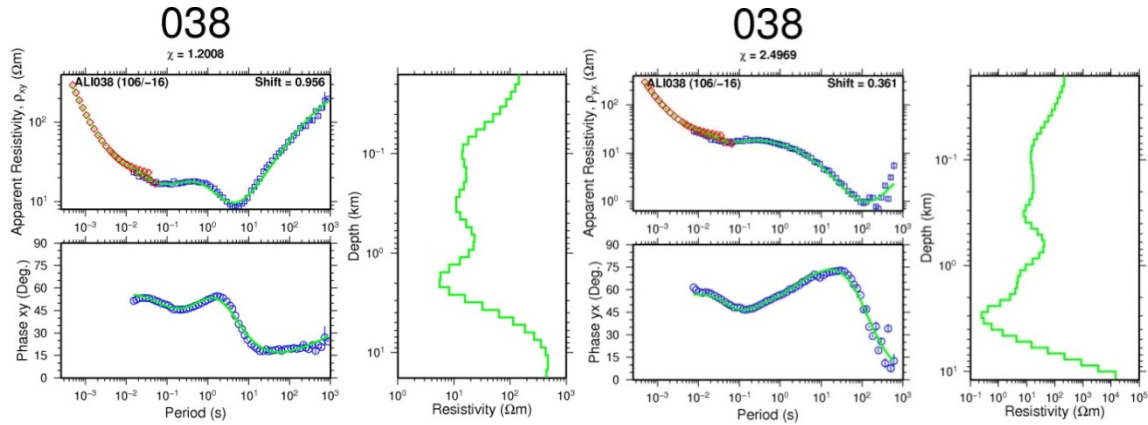
Figure 6.20. A separate 1D joint inversion of xy and yx of an MT sounding (038) and a TEM sounding. The two modes are shifted differently.

Histogram of shift multipliers of both xy and yx modes for all the MT soundings used in the 3D inversion is presented in Figure 6.21. The mean shift values are 0.78 for xy mode and 0.71 for yx mode. The mean values for both cases is less than one and the reason for this could most probably be due to the conductor (bentonite) that was placed locally below the electrodes which act as near surface inhomogeneities.

Figure 6.21. Histogram of shift multipliers for S_{xy} (blue) and S_{yx} (brown), for all the MT soundings used in the 3D inversion.

6.3.4 Input Data Description and Inversion

Input data in the 3D inversion with WSINV3DMT were formed from the basic elements of the real and imaginary parts of the impedance tensor ($\mathbf{Z}$). Due to the computational cost, the 3D inversion of MT data was performed for 47 sound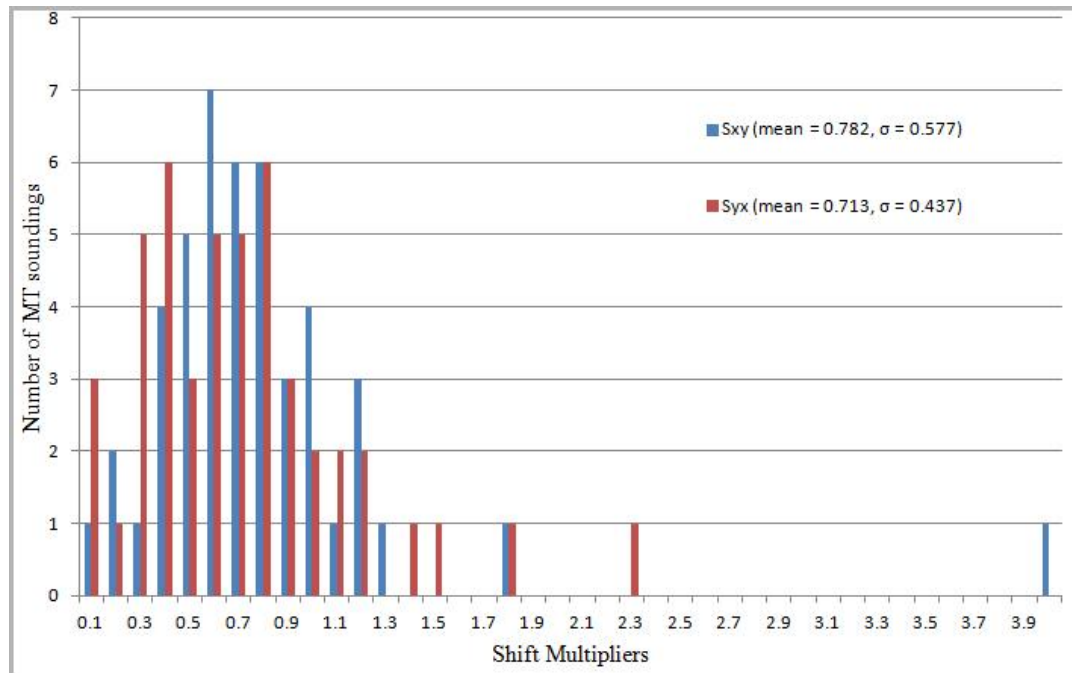ings at only 16 periods for the full impedance tensor elements (for 8 real and imaginary values for each period). Four periods per decade were selected over the period range of 0.0617 to 149.25 s. The specific periods included in the inversion were the following: 0.0617, 0.1064, 0.1786, 0.294, 0.4926, 0.8547, 1.4286, 2.3256, 3.937, 6.849, 11.364, 18.518, 31.25, 54.645, 90.909 and 149.25 s, giving a total of 6016 MT data values.

The full static shift corrected impedance tensor data including error bars for all the soundings at each of the selected periods were provided as one data file with their station location. The inversion was run using a Linux operating system on an Intel Xeon 64-bit, 2.83 GHz processor with 3.6 GB memory. Five runs were performed and 10 iterations were allowed for each run. The best model obtained from each run was used as initial model for the successive runs. Each iteration step took about 27 hours.

Most of the MT data at short periods show one dimensional resistivity structure; therefore, the 3D model and the models obtained from 1D inversion should be expected to be in good agreement at shallow depth, but topography should be noted during the comparison. But because the shortest period used in the inversion is 0.06 s, the resistivity structure at shallow depth is probably resolved poorly resulting in a relatively poor comparison with the results of 1D inversion.

According to several research papers (e.g. Ranganyaki and Madden, 1980, Mackie et al., 1988, Eysteinsson and Hermance, 1985), interpretation of MT data from coastal environment requires that the low resistivity of seawater is correctly modelled. This is because the seawater is a very good conductor and can affect MT soundings located close to the sea.

The Red Sea coast is located about 30 km east and northeast of the study area, and about 26 km to the north-west of the study area where a long and narrow strip of bay (~52 km long and ~11 km wide Gulf of Zula) are nearest to Alid survey area. As described in section 6.3.2, the vertical grids extend to ±110.5 km from the centre of the model grid and therefore, part of the Red Sea is included in the grid model. To see how the seawater affects the MT data in the inversion, 3D modelling was also performed taking into account the effect of the sea. Part of the sea which is included in a best model was kept as a fixed feature by designing a model control and the resistivity of the seawater was taken to be 0.3 Ωm. Seafloor topography was estimated from bathymetry maps of satellite images.

The 3D inversion with and without the seawater constraint showed similar results; therefore, we can conclude that the MT soundings from the study area are far enough from the Red Sea that the effect of the seawater is negligible for the periods considered. Figure 6.22 is provided to show the similarity between the models obtained from 3D inversion with and without including the sea.
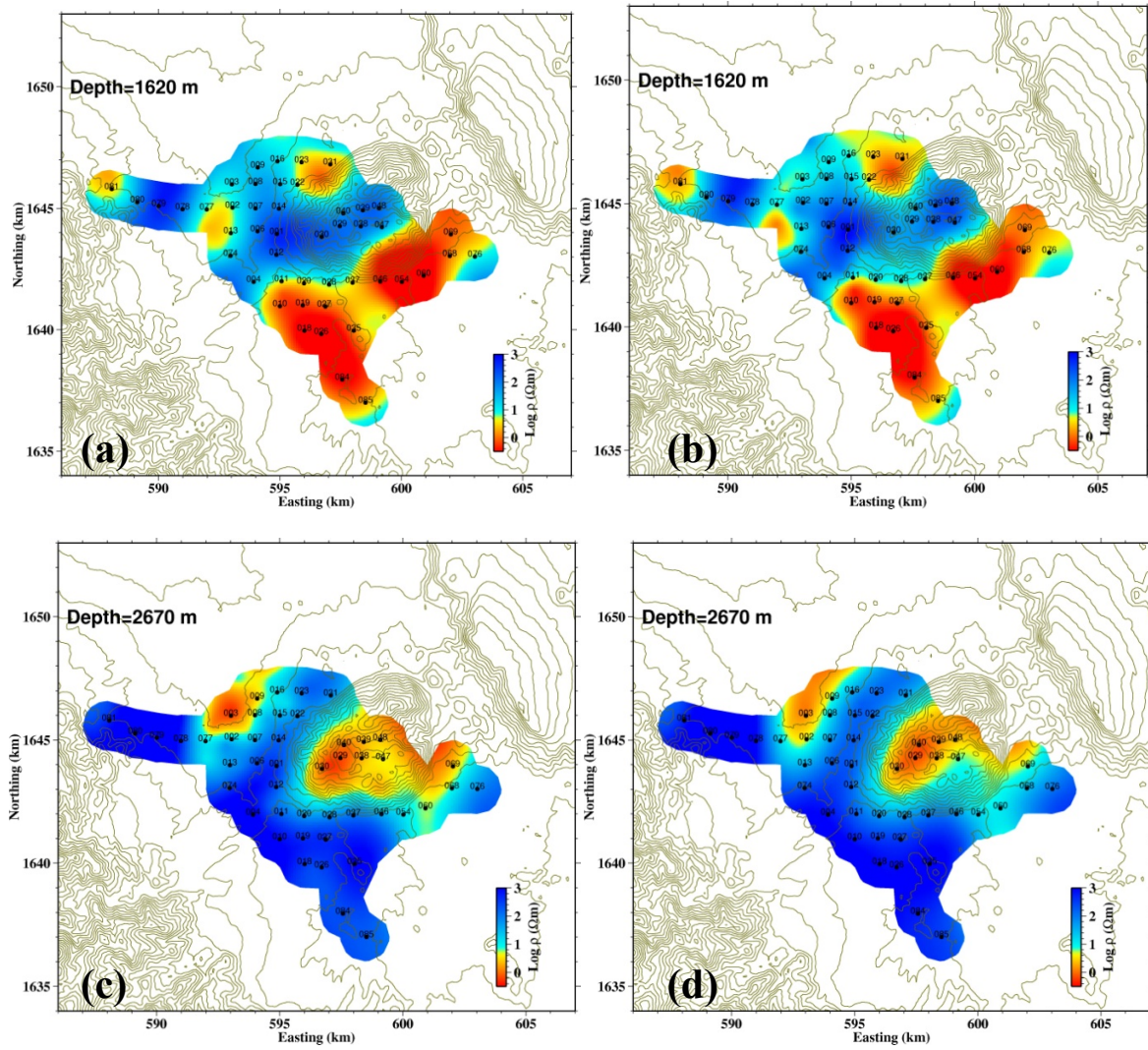
Figure 6.22. Smoothed resistivity slices at depths of 1620 m and 2670 m with (a and c) and without (b and d) the constraint of Red Sea in the initial model.

6.3.5 Results of 3D inversion

Resulting models obtained from the 3D inversion using an initial model of a layered earth model consisting of five layers and without including the sea are considered here for discussion. Figures 6.23(a)-(j) show the central part of the smoothed resistivity models as iso-resistivity maps at the depths of 220, 425, 750, 1000, 2080, 2670, 3410, 4310, 5530 and 7000 m b.g.l. (meters below ground level) corresponding to the centres of the horizontal grid layers. The models are obtained from fairly good fit of the data and response after seven iterations of the last run (fifth run) with rms value of 1.86. The fit of the data and responses of the inversion for xy and yx modes are presented in Appendix D.

MT is capable of imaging the conductivity distribution of the subsurface to several kilometres both in lateral and depth extension. As can be seen from the geological map (Figure 2.2) and the simplified tectonic map (Figure 2.1), the rift axis in Alid geothermal area is bounded by crystalline rock units of the Nubian plate to the west and the Danakil Alps to the east. Because of the crystalline nature of the bounding rock units, they are expected to have high resistivity. Therefore, to see how these bounding rock units effect on

74

the model results of the 3D inversion (i.e. to see whether the resistivities of the Precambrian rocks on the Nubian plate and stratoid basalts on the Danakil Alps are required by the MT data), the resistivity slices in Figure 6.23 are covering a larger area outside the surveyed area.
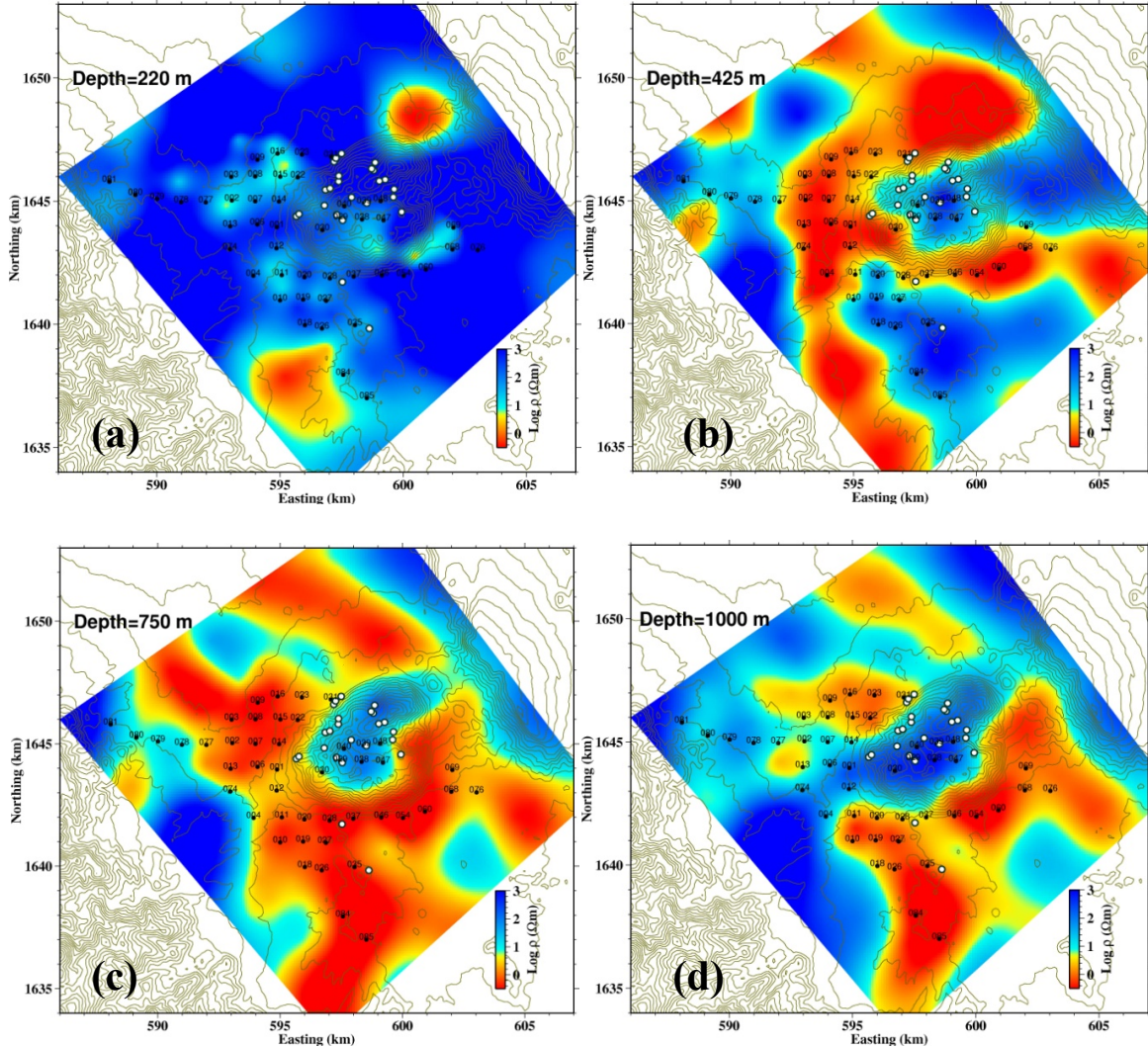

Figure 6.23. Smoothed resistivity slices of model result from 3D inversion at ten depths: i.e. at 0.22 km depth (a), at 0.425 km depth (b), at 0.75 km depth (c), at 1.258 km depth (d), at 2.085 km depth (e) at 2.67 km depth (f), at 3.41 depth (g), at 4.35 km depth (h), 5.53 km depth (i) and at 7 km depth (j). Geothermal surface manifestations (fumaroles, boiling and hot springs) are shown with white dots, black dots are MT sites and the thin light green curved lines are surface topographic contours.

The 3D inversion results of MT data show more or less a similar resistivity distribution as was found by the 1D joint inversion of TEM/MT data at depths down to about 1 km below ground level. The resistivity slices of the 1D models are given in meters below sea level while the resistivity slices of the 3D models are given in meters below ground level. The elevation of the MT soundings in the study area is on the average about 200 meters above sea level in the low plain land and about 600-650 meters on the top of the mountain. Therefore, about 200 meters should be added to elevation of the resistivity slices of the 1D

75

models in Figure 4.6 to be comparable with the 3D models in Figure 6.23 (e.g. iso-map 550 m b.s.l. for 1D is equivalent to 750 m for the 3D iso-maps).

At shallow depth, 0.22 km below ground surface (Figure 6.23a), the model shows high resistivity in most part of the map and almost in all the area covered by MT soundings. Two zones of conductive areas with resistivity values < 1 Ωm are observed outside the surveyed area, one is northeast of mount Alid and the other in the southern part of the survey area. Slightly conductive spots are also observed within the area covered by MT soundings aligned in the same direction as the rift axis. The high resistivity in the area is most probably due to the unaltered fresh volcanic rocks in the rift zone and the crystalline rock units outside the rift. The slightly conductive spots might presumably be correlated with the conductive zeolite-smectite alteration mineralogy (alteration mineralogy is discussed in chapter 7). The conductive zones could be correlated with some conductive sediment or from old remains of a salt lake.

The resistivity model slice at 0.425 km below ground surface (Figure 6.23b) shows low resistivity as low as ~ 0.4 Ωm mostly around Mt. Alid. In addition, some low resistivity values are also observed south of the mountain where no sounding is located. They are connected to the conductor west of the mountain. The two spots of conductive bodies observed in Figure 6.23a have now broadened and are connected to the main conductor observed at this depth.

The resistivity distribution at a depth of 0.75 km (Figure 6.23c) is somewhat similar to that at 0.425 km depth, but now the high resistivity to the south of the mountain is replaced by a conductive body extending to the eastern side of the mountain. The high resistivity body observed in the 1D models (Figures 6.4b-d), is also observed here and cuts Mt. Alid along its longest axis in the SW-NE direction. This high resistivity continues downwards and is more pronounced at a depth of 1 km (Figure 6.23d). At that depth, the low resistivity body observed to the west of the mountain at 0.75 km has disappeared and is replaced by a resistive body.

The resistivity slice at the depth of 2.085 km (Figure 6.23e) shows low resistivity under the eastern (where there are no data) and western parts of the mountain. The conductive body observed east of the mountain in Figure 6.23d, extends northwards to the northeast of the mountain. A relatively low resistivity (~ 4 Ωm) beneath the mountain starts to appear and gets broader and lower (~0.6 Ωm) at the next depth slice at 2.67 km in Figure 6.23f. This conductive body connects to the eastern conductor. Two spots of conductors are also observed in the northwest and southeast margin of the maps in Figures 6.33e-g outside of the surveyed area.

At a depth of 3.41 km (Figure 6.23g), the conductor observed at 2.67 km beneath the western part of the mountain (Figure 6.23f) still exists, but the conductor in the eastern side of the mountain is fading out and completely disappears in the depth slice of 4.35 km (Figure 6.23h). The general alignment of the low resistivity bodies down to a depth of 4.35 km (Figure 6.23h) is parallel to the rift axis. In Figure 6.23h, the conductor beneath the western part of the mountain is slightly shifted southwards and the two spots of conductors in the northwest and southeast margins of the maps are fading out and completely disappear at the depth of 5.53 km (Figure 6.23i). In the southern corner of the maps, a conductor is also starting to reappear at this depth and continues downwards to a depth of 7 km (Figure 6.23j). The resistivity slice at the depth of 7 km (Figure 6.23j) which may not

have good resolution, since the longest period used are only 149 seconds, shows a conductor in the northern part of the map outside data coverage and therefore questionable whether it is required by the data.
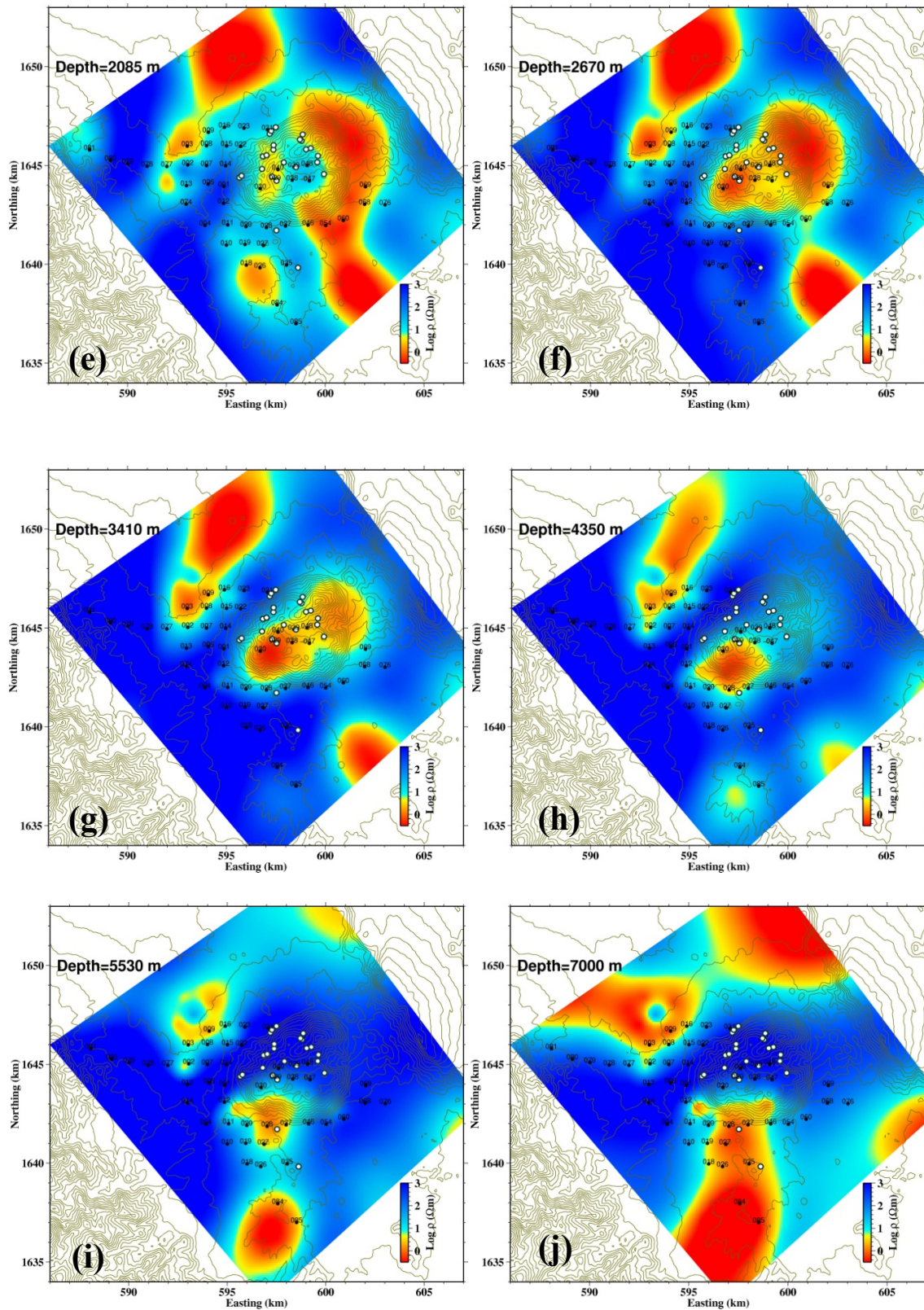

Figure 6.23. Continued.

The central part of the model resulting from 3D inversion is also presented as vertical cross sections along the y-axis (perpendicular to the geological strike or the rift axis) and x-axis (parallel to the rift axis) in the model coordinate system. Figure 6.24 shows the location of the cross sections labelled by their x-coordinates for sections across the rift axis (NW-SE direction) and by their y-coordinates for sections along the rift axis (SE-NW direction). Five vertical cross sections across the rift axis (parallel to the y-axis in the model coordinate) and six sections along the rift axis (parallel to the x-axis in the model coordinate) are presented in Figures 6.25 and 6.26, respectively.
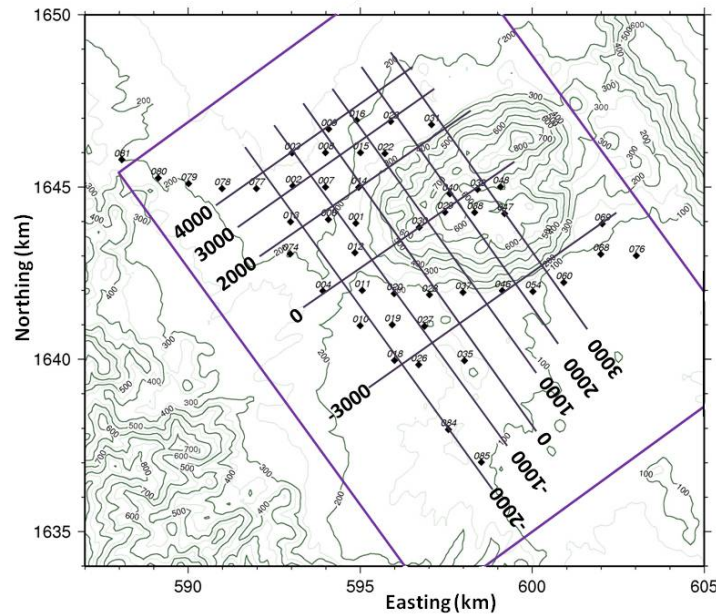

Figure 6.24. Location of 3D vertical resistivity cross sections shown in Figures 6.25 and 6.26. Black diamonds are MT soundings and thin green lines are topographic contour lines in m a.s.l.

The cross sections at x=4000 (Figure 6.25a) and x=3000 (Figure 6.25b) are perpendicular to the rift axis in the north western part of the survey area and have similar resistivity structures, with a high resistivity surface layer, ~ 360 m thick underlain by a shallow conductor (variable values, down to ≤ 1 Ωm), ~ 600 m thick. Below the shallow conductor there is a moderately resistive body in the central part (from y=-2500 to y=1500) for the cross section at x=4000 underlain by a deeper conductor, which continues downwards. The deeper conductor for section x=3000 is relatively higher and variable in resistivity (4-25 Ωm). High resistivity is observed on the southwest part of the cross sections (from y=-5000 to y=-2500). This high resistivity body which is covered by sediments could probably be correlated to the Precambrian basement of the Nubian plate. In the northeast part of the cross section, the shallow conductor is underlain by high resistivity followed by a deep conductor.

The cross sections at x=2000 (Figure 6.25c) shows a high resistivity layer on the surface underlain by a shallow conductor (≤ 1 Ωm) of variable thickness followed by a uniform high resistivity.
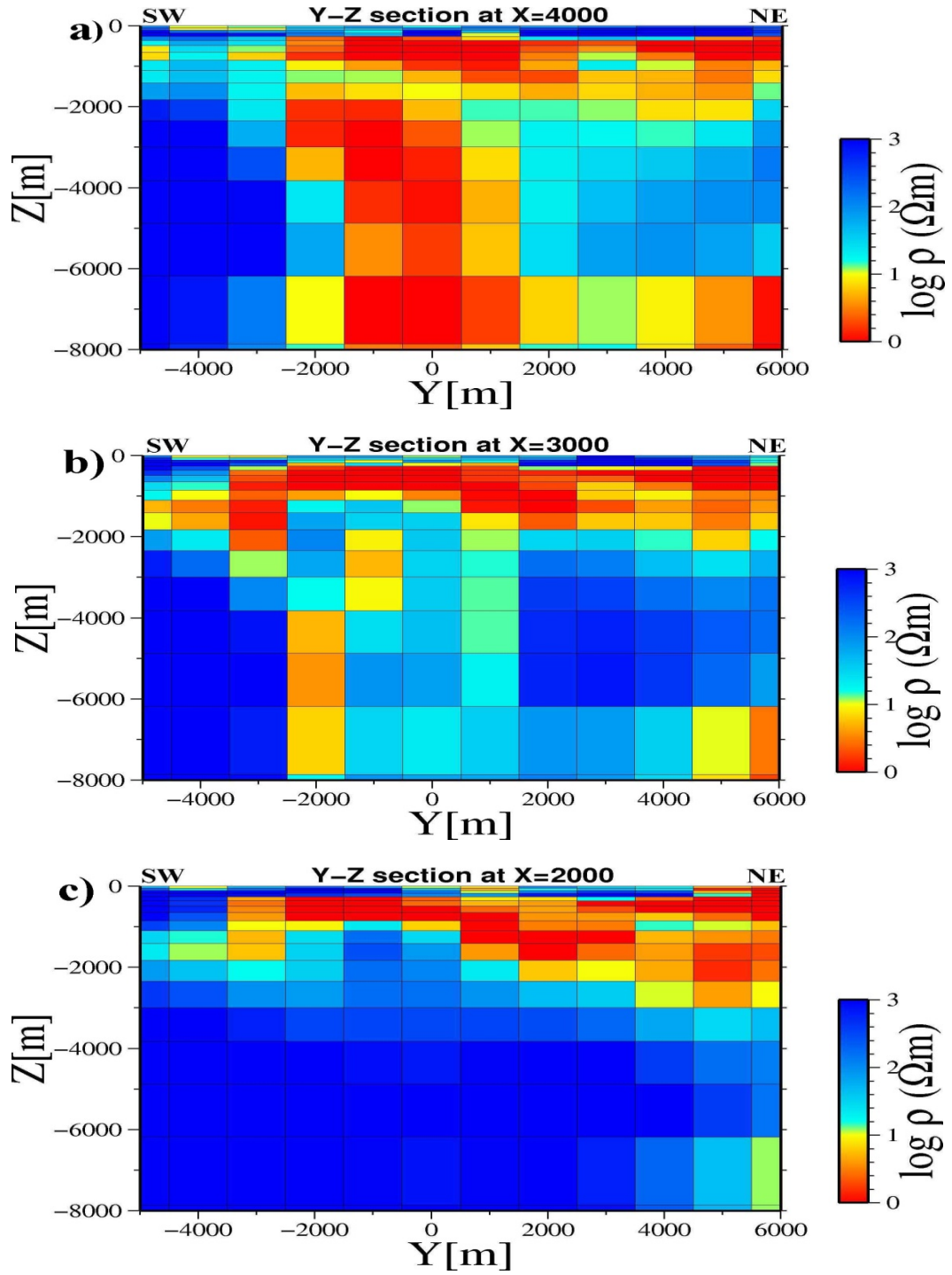
78

Figure 6.25. Vertical resistivity cross sections across the rift axis (SW-NE direction). (a) across the model at x=4000 m. (b) across the model at x=3000 m. (c) across the model at x=2000 m. (d) across the model at x=0 m. (e) across the model at x=-3000 m. (Location of the cross sections is shown in Figure 6.24).
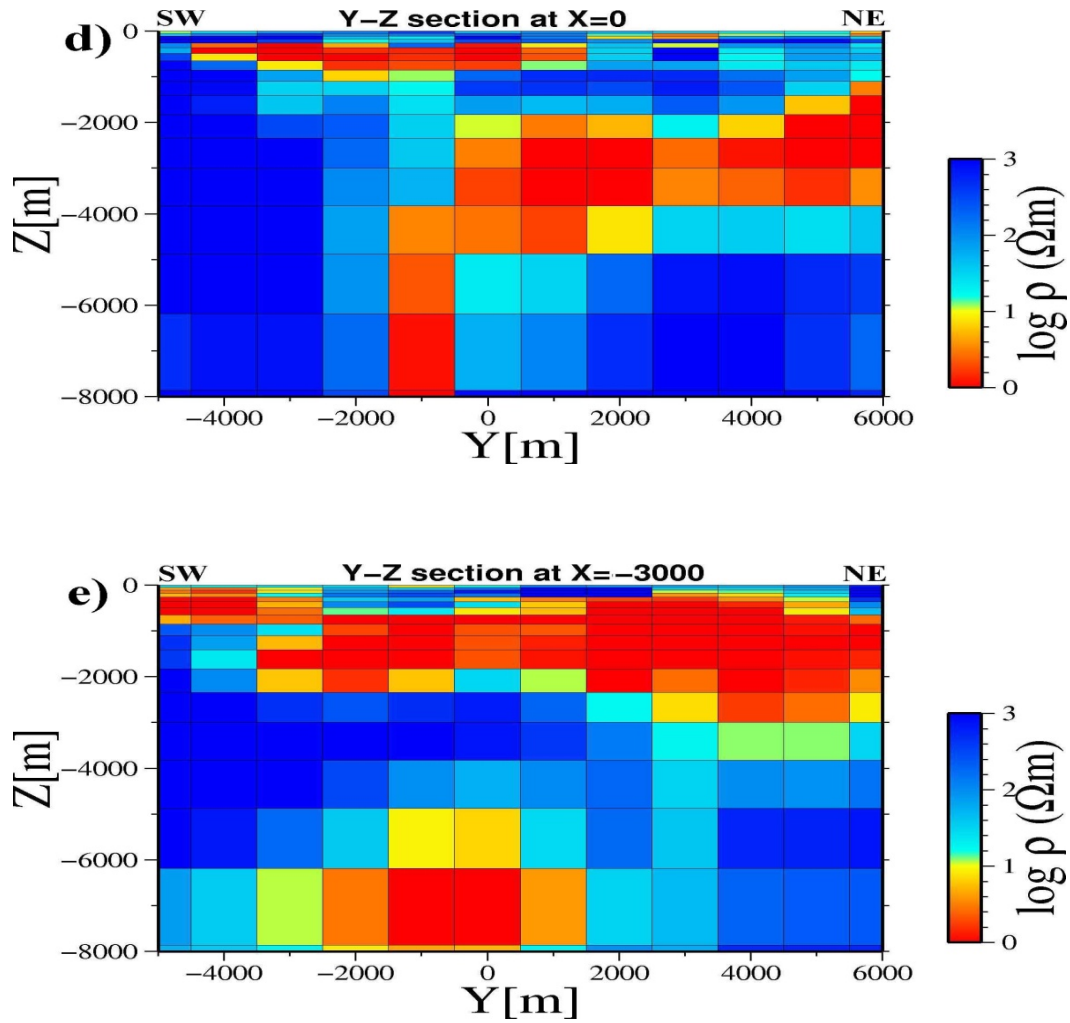
Figure 6.25: Continued.

The cross section at x=0 (Figure 6.25d) passes through Mt. Alid along its main axis. The cross section shows three resistivity layers in its southwest part, a high resistivity surface layer, about 360 m thick underlain by a conductor of resistivity values ≤ 1 Ωm and about 500 m thick, followed by almost a uniformly high resistivity body. No deep conductor is encountered on the southwest part of the cross section. The central and northeast part of the cross section show the resistivity distribution beneath the mountain.

The complex geology of Mt. Alid (see chapter 2) is reflected in the near surface resistivity structure that varies greatly from about 5-500 Ωm. A low resistivity value (~1 Ωm) is observed at about 2-4 km depth beneath the mountain with high resistivity below, except at narrow interval around y=-1000. Between y=-500 and y=2000, the shallow conductor is underlain by high resistivity followed by the deep conductor. On the northeast part of the cross section, relatively low resistivity values are observed on surface which might be correlated with the big surface manifestations and alterations.

The cross section at x=-3000 is just south of the mountain. On the central part of the section (from y=-2500 to y=1500), four resistivity layers are found: a resistive layer at the surface underlain by a shallow conductor followed by a high resistivity about 2.5 km thick and at a depth of ~2 km underlain by a deeper conductor. On the southwest end of the

cross section (from y=-5000 to y=-3000), a low resistivity is observed from the surface down to about 1 km followed by high resistivity. This high resistivity body, covered by sediments could probably be correlated to the Precambrian basement of the Nubian plate. The northeast part of the cross section shows three resistivity layers: a thin resistive surface layer underlain by a thick low resistivity down to about 3 km, followed by a high resistivity layer. A deep conductor, at about 5-6 km depth appears left of the center part of the cross section. This conductive body which continues downwards is presumably the heat source. An oasis as outlined in the report by Eysteinsson et al., 2009 is present on the surface above this deeper conductor.
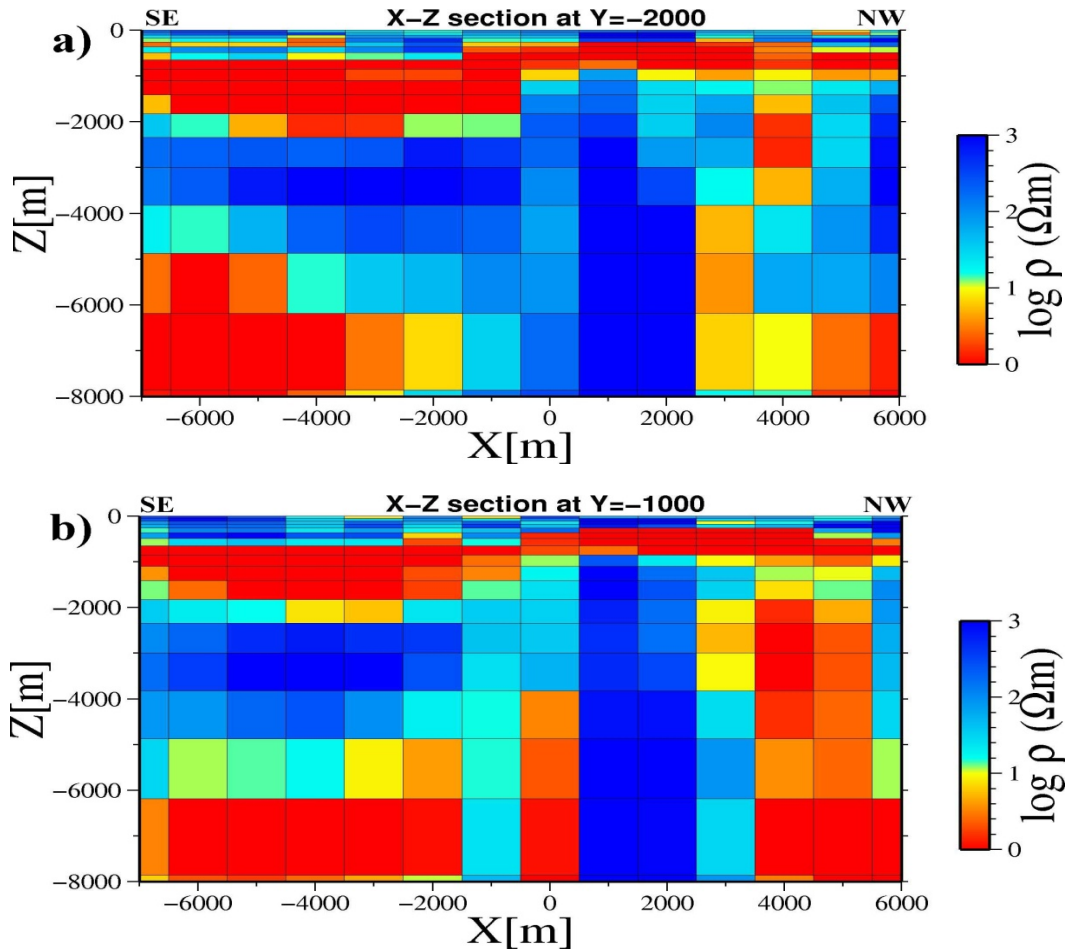

Figure 6.26. Vertical resistivity cross section along the rift axis (SE-NW direction). (a) across the model at y=-2000 m. (b) across the model y=-1000 m. (c) across the model at y=0 m. (d) across the model y=1000 m. (e) across the model at y=2000 m. (f) across the model at y=3000 m. (location of the cross sections are shown in Figure 6.24).

Six cross sections along the rift axis (x-axis in the model coordinate) are presented in Figure 6.26 to reveal the resistivity structure perpendicular to the rift axis. The cross section at y=-2000 and at y=-1000 are to the west of the mountain, while the cross sections at y=0, y=1000, y=2000 and at y=3000 cross the mountain, with the cross section at y=0 passing through the western slope of the mountain. Cross sections at y=-2000 and y=-1000 depict the common four resistivity layers on their southeast half from x=-7000 to x=-500. The first layer is a high resistivity body down to about 650 m depth with some low resistivity values in between for the cross section at y=-2000. Below the first high

81

resistivity layer is a low resistivity body down to about 2 km, followed by a high resistivity layer down to about 5 km depth underlain by a deep conductor.

The cross section at y=0 shows some similarity to the two cross sections at y=-2000 and at y=-1000 on its southeast side, but now the deeper conductor is below 6 km depth from x=-7000 to x=-2500. Between x=-1500 and x=500, the deeper conductor starts at 2 km depth.

 The three cross sections also encounter a high resistivity block that extends from about 1 km depth downwards between about x=500 to x= 2500. To the north western side, the cross sections show a low resistivity with variable resistivities below the resistive surface layer.

The cross sections at y=1000, at y=2000 and at y=3000, show a similar resistivity structure on their southeast half as the other cross sections parallel to the rift, but now the deep conductor is replaced with relatively resistive body. The cross sections in the central part from x=-3000 to x=2000, show the resistivity structure below the mountain. The deeper conductor for these cross sections ranges from about 2 km to about 5 km depth. On the surface of the central part, of the cross sections show a relatively low resistivity.

All the cross sections which are taken parallel to the rift axis, encountered the fault line which runs SW-NE (broken yellow line in Figure 6.13). The cross sections at y=-2000 and at y=-1000 encountered the fault line at x=-500 while the other four cross sections encountered the fault line at x=-1500.
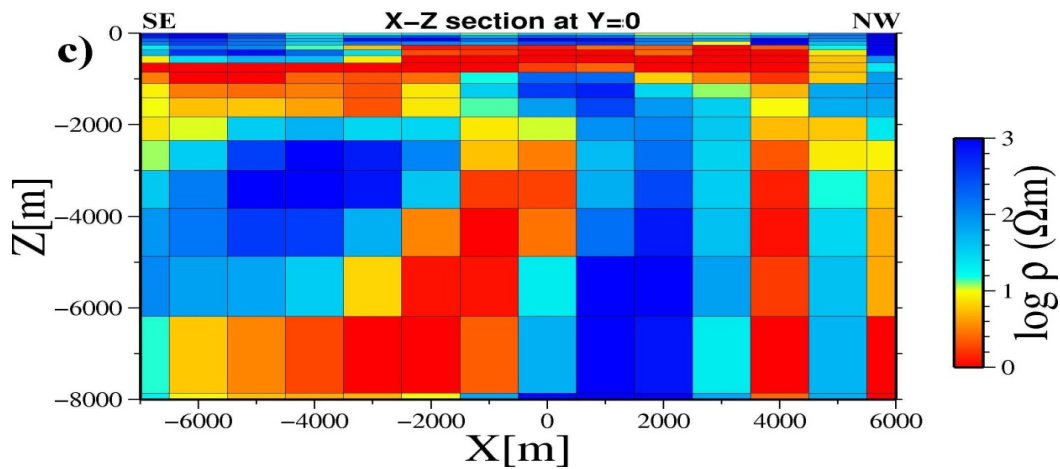
Figure 6.26. Continued.
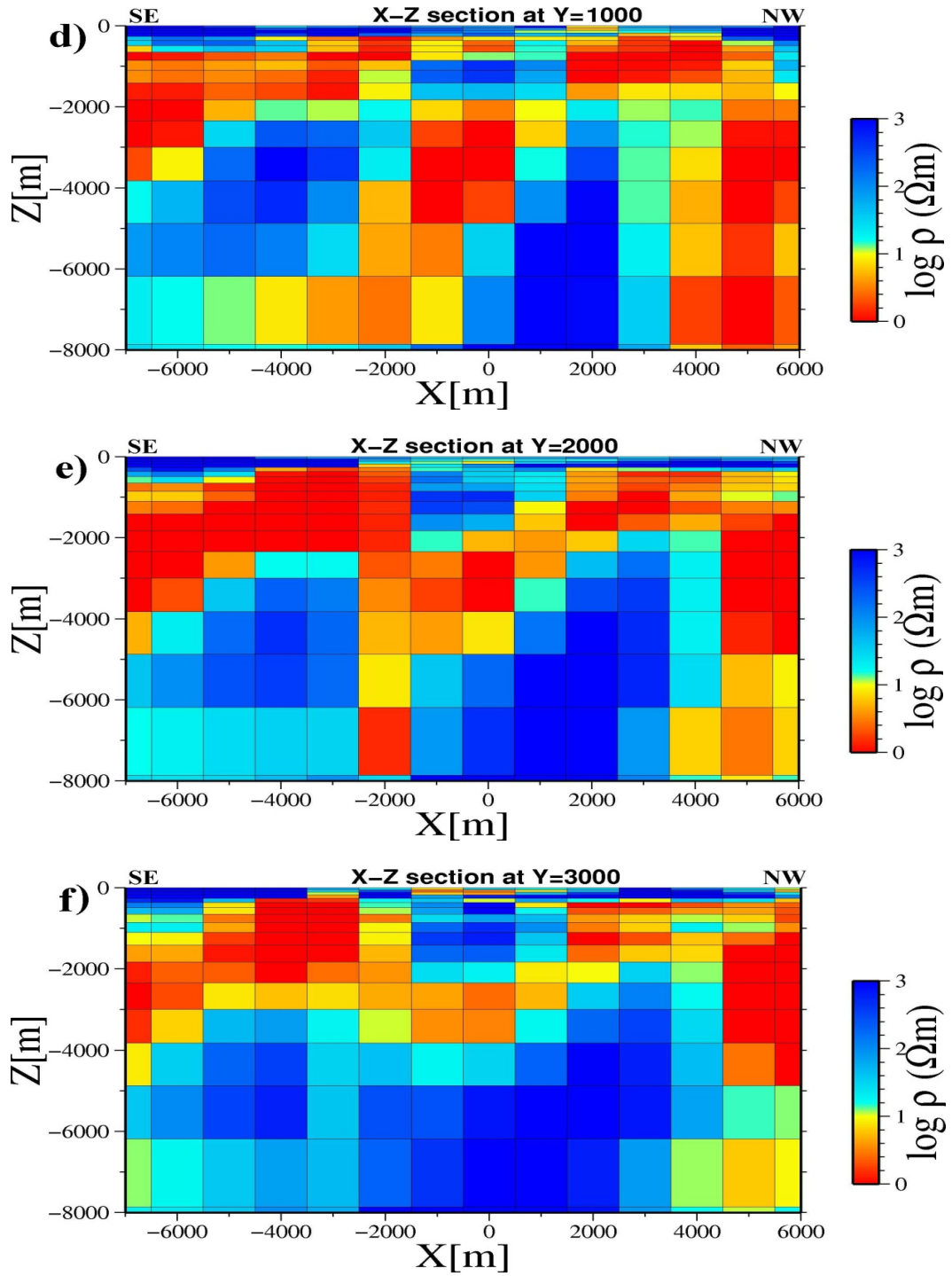
Figure 6.26. Continued.

6.4 Comparison of 1D, 2D and 3D modelling results

Dimensionality analysis discussed in section 5.1 showed that the 3D effect in the MT data is pronounced at long periods (≥ 1 s). Because the MT data show 1D nature at short periods (<1 s), the resistivity distribution in the models of the 3D inversion of the MT data are comparable to the model results of 1D joint inversion of TEM/MT at the shallow depths

down to about 1 km below ground level. Detailed picture may, however not be seen from the 3D models at shallow levels as the shortest period modelled in the 3D inversion is 0.06 s and also since the 3D inversion code is not capable of handling topography. The 1D inversion of MT data for the determinant tensor jointly inverted with TEM data was discussed in section 6.1. Difference in the resistivity structure at deeper levels is expected; however, the general resistivity structure is similar from both inversions. In the 1D inversion, topography was included and therefore, the resistivity slices and cross sections of the 1D models (Figures 6.4 and 6.6-6.11) are given in meters above and below sea level. Topography was not included in the 2D and 3D inversions and therefore not included in the resistivity cross sections and resistivity slices. The cross sections and resistivity slices are given in meters below ground level.

Figure 6.27 and 6.28 show comparison of the resistivity distribution and structures from the model results of 1D, 2D and 3D inversion. In Figure 6.27, a profile from the northern part of the study area is considered mainly for comparison of the vertical structure of the resulting models with the three different inversions. A sharp vertical resistivity contact is observed in the model from 1D inversion (Figure 6.27a), the joint TM+TE modes (Figure 6.27b) of the 2D inversion between sounding 008 and 009. But because sounding 008 is not included in the cross section, the resistivity contact is not observed from the corresponding profile of the 3D inversion (Figure 6.27c) at that point but some contact is seen at y=500 at the depth interval of 2 km to 4 km. The three inversion approaches also show similarity in the general resistivity distribution across the profiles except in the southwest part.
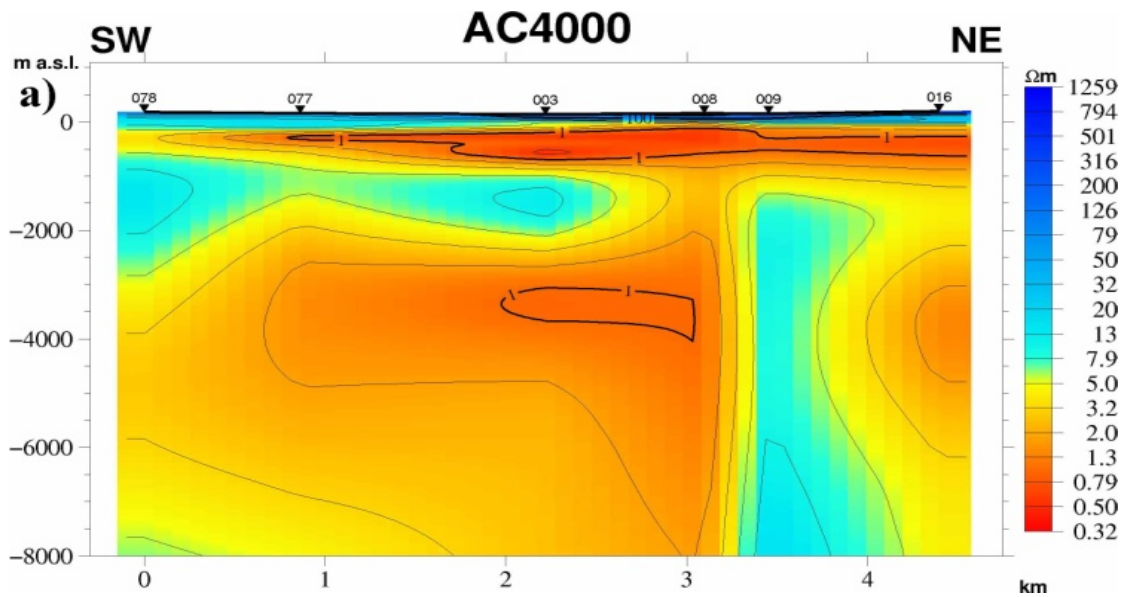

Figure 6.27. Comparison of 1D joint inversion of MT/TEM data (a), jointly inverted TM and TE modes of 2D inversion (b) and 3D inversion (c) vertical cross sections in the northern part of the study area across the rift (ac4000 in a and b corresponds to x=4000 of 3D inversion in c). (Location of the cross sections are shown in Figure 6.24).

Figure 6.27. Continued.

Figure 6.28 shows a cross section perpendicular to the rift axis through mount Alid. The three inversions show some similarities in their modelling results at shallow depths (note that in the 1D model, Figure 6.28a, topography is included). At deeper levels, the modelling result from the 1D inversion, Figure 6.28a, shows a different resistivity structure from the modelling result of 2D (Figure 6.28b) but is somewhat similar with the 3D (Figure 6.28c) inversion result. Here a deep conductor is seen below sounding 030 from

the 1D inversion (Figure 6.28a) and 3D inversion (Figures 6.28c) which is totally absent from the modelling results of 2D (Figure 6.28b) inversion.

Figure 6.28. Comparison of 1D joint inversion of MT/TEM data (a), 2D jointly inverted TM and TE modes (b) and 3D inversion (c) vertical cross sections across the rift crossing Mt. Alid (ac-0 in a and b corresponds to x=0 of 3D inversion in c). (Location of the cross sections are shown in Figure 6.24).

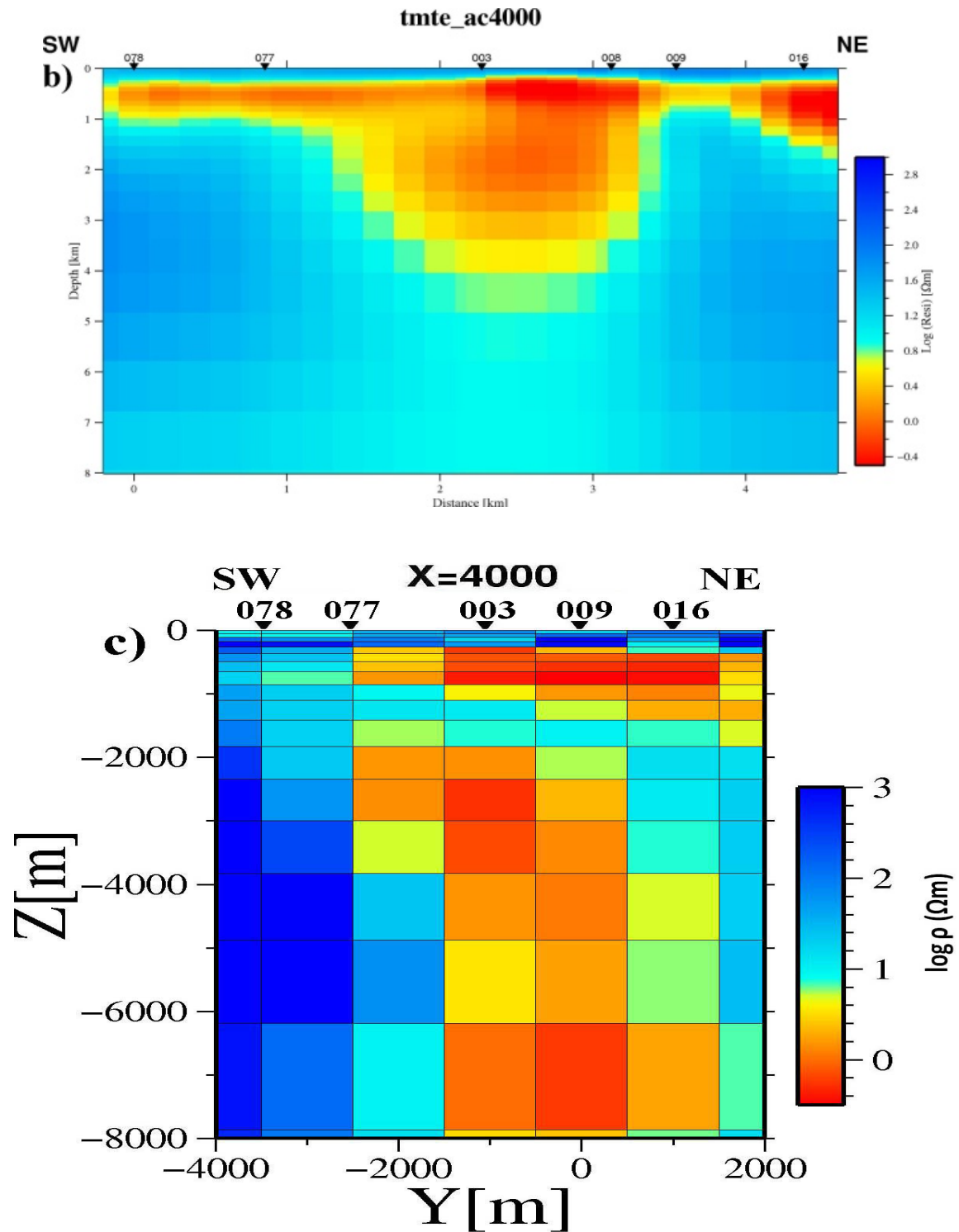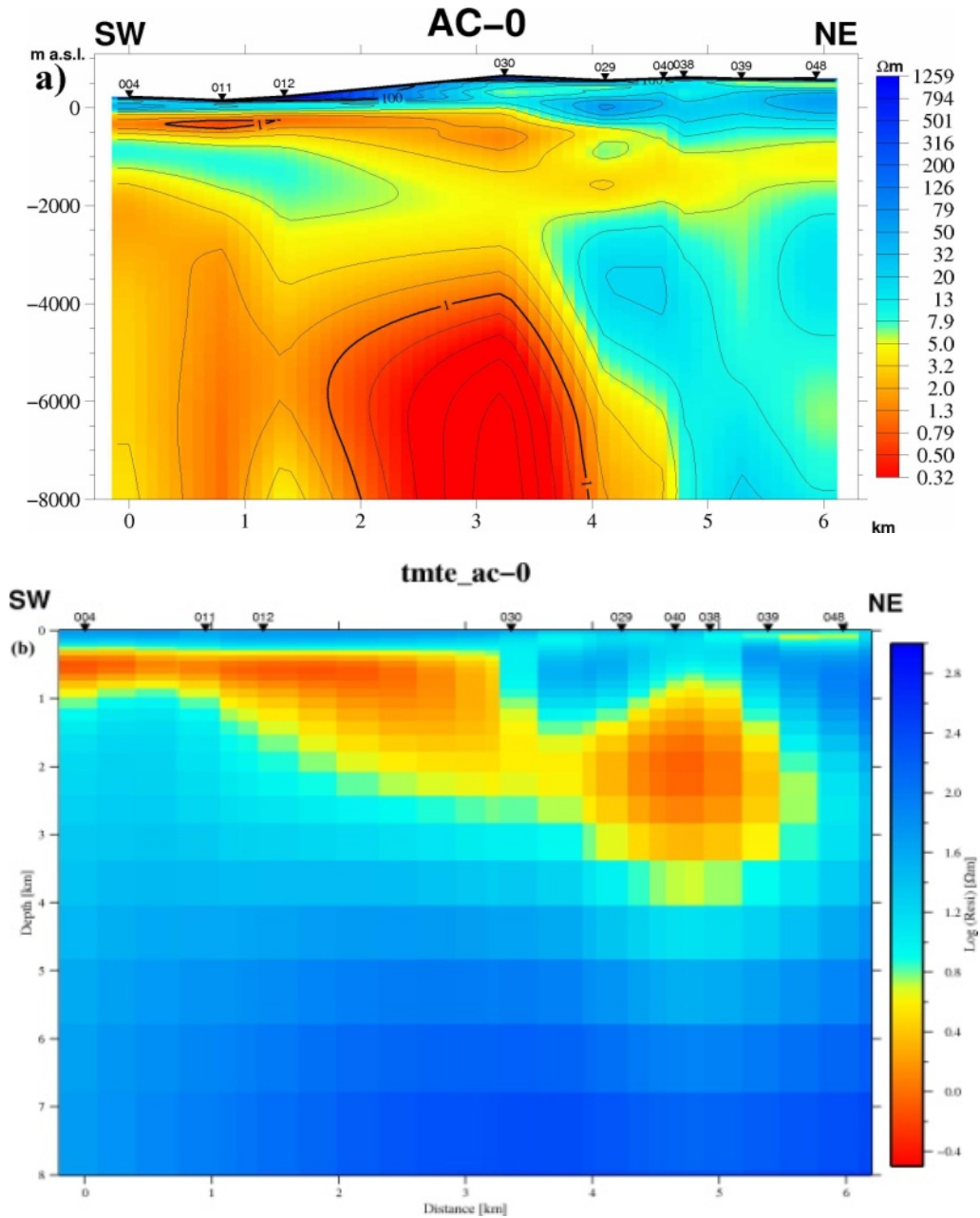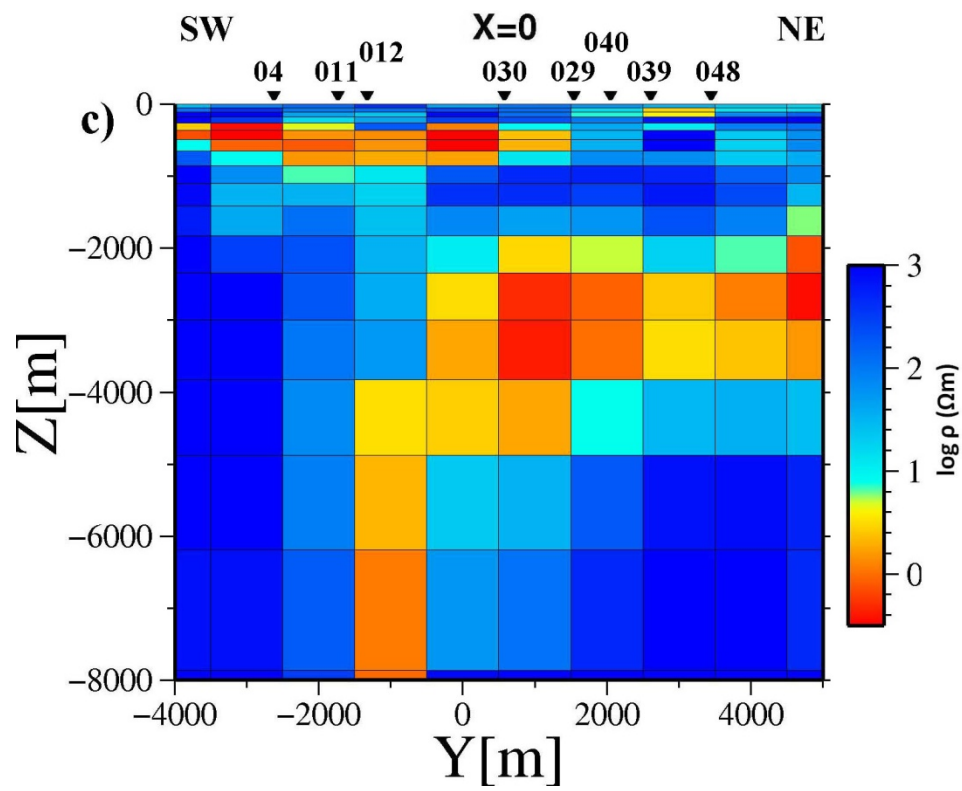*Figure 6.28. Continued.*

7 Discussion, Conclusions and Recommendations

The resistivity structure of the basaltic crust in Iceland has been compared with the crust in the Asal Rift in Djibouti and was found to be quite similar (Árnason et al., 1988). Comparison of the resistivity structure with data from wells has been carried out in high temperature geothermal areas in Iceland (Árnason et al., 2000) and in Asal Rift (Árnason et al., 1988). The results were in good agreement with alteration mineralogy. Therefore, the experience from Iceland and Asal rift might also apply to Alid geothermal area.

In the Icelandic high-temperature geothermal areas, at temperatures from 100-200°C, smectites and zeolites are the dominant alteration minerals but chlorite and epidote predominate above 250°C. Between 200°C and 250°C, there is a transition called the mixed layer zone (Árnason et al., 1987; Árnason and Flóvenz, 1992).

Usually, it is expected that resistivity decreases with increasing temperature but in high-temperature volcanic areas the situation is the reverse in the chlorite and chlorite-epidote alteration zone; i.e., resistivity increases with increasing temperature. The reason for this transition is that smectites and zeolites which are formed at relatively low temperatures, have mobile ions in the structure of the crystal that makes it easy for electric currents to pass through. In the high temperature alteration minerals (chlorite and chlorite-epidote alteration zone), these ions are fixed in the crystal lattice, hindering the flow of electricity.

The resistivity is relatively high in cold unaltered rocks outside the reservoir. The low-temperature alteration mineralogy, the smectite-zeolite zone, forms a low-resistivity cap at the outer margin of the reservoir. The upper boundary of the low-resistivity cap corresponds to temperatures in the range of 50-100°C, depending on the intensity of the alteration (Árnason et al., 2000). The transition from the low-resistivity cap to the resistive core corresponds to temperature in the range of 230-250°C (Árnason et al., 2000). The resistivity increases again towards the interior of the reservoir at the top of, or within, the mixed layer clay zone. If the temperature is in equilibrium with the dominant alteration mineralogy, then the resistivity structure can directly be correlated with the temperature.

The resistivity structure observed in Alid geothermal area might partly or fully be correlated with the hydrothermal alteration mineralogy. There are four resistivity layers in most part of the survey area observed mainly from 1D and 3D inversions. A thin high resistivity layer followed by a shallow depth conductor and then follows a high resistivity layer underlying by a deep conductor. The upper conductive structure below the unaltered resistive surface layer which is present in most of the study area might be associated with the low temperature alteration mineralogy. There is also a possibility that, this thin shallow resistivity layer could be associated with the old conductive marine sediments (Eysteinsson et al., 2009). The high resistive core below the shallow conductor might be associated with the high temperature alteration mineralogy, while the deep conductor may represent the partial melt, which is the heat source for the geothermal system.

Several lithological contacts or lineaments were identified by the three inversions. A sharp resistivity contact or fault line is observed with an orientation of SW-NE (broken yellow line in Figure 6.13) at the depth interval of approximately 0.5-2 km. This fault line is

clearly observed particularly from the 1D and 3D models, which is slightly different from the fault line outlined in the geological map (Figure 2.2). The southern side of the fault line is downthrown as can be seen in Figure 6.26b at x=-500 m.

From the modelling results of 1D inversion, a low resistivity body below the western part of mount Alid and to the west of the mountain, is observed with approximately NW-SE direction (almost parallel to the rift axis) from about 2-3 km down to approximately 7 km (Figure 6.4e-h). This low resistivity body is absent from the modelling result of 3D inversion, but only spots of low resistivity are observed in the northwest and beneath the south western side of the mountain. The dimensionality analysis showed that the MT data are highly three dimensional at long periods, greater than 1s and for some others greater than 10 s, which corresponds to the deeper levels. Therefore, the resistivity structure from the modelling results of 3D inversion of the MT data at deeper levels is more trustworthy as compared to results of 1D inversion. In addition to the low resistivity body beneath the western part of the mountain seen in the 3D inversion, there is also a low resistivity body beneath the eastern part of the mountain from about 0.75 km to approximately 3.41 km. There are no soundings on the east part of the mountain so the reality of the low resistivity body is uncertain, but the eastern part of the mountain is highly collapsed structurally and the rocks on the surface are highly altered.

The mountain Alid is a dome shaped volcanic center located at the center of the graben. Clynne et al. (1996) (Figure 2.3) believe that the dome was apparently formed as a result of shallow intrusion of rhyolitic magma. According to the study by Clynne et al. (1996), the doming uplifted the Precambrian rocks and deformed the overlying sequence of Pliocen/Pleistocene sediments caped by different types of lava flows. Subsequent to the structural doming, there were eruptions of pyroxene rhyolite lavas on the flanks of the mountain and rhyolite was erupted on the mountain as pumice and pyroclastic flow.

The 3D modelling somehow support the conceptual model of geological cross section presented by Clynne et al. (1996) (Figure 2.3). Modelling results in Figures 6.23, 6.25 and 6.26 show the presence of conductive bodies at a depth of approximately 2-5 km beneath the mountain which could be the magma and/or the hot plutonic rock seen in the conceptual model in figure 2.3.

The fumaroles and boiling pools (white circles on the iso-maps of Figure 6.23) are distributed widely on the top of the mountain. This suggests that hydrothermal system underlies most parts of the mountain. In addition, it is believed that hydrothermal system exists below the south west of the mountain, where big thermal manifestation (the oasis) is located. The fumaroles vent through different lithologies (Lowestern et al., 1997), this means that they don´t appear to be controlled by the rock types or contacts of different rock units but through fractured zones. Magma intrusion beneath the mountain that possibly formed the structural dome most likely created the collapses on the eastern and western parts of the mountain and created abundant fracture zones beneath Alid volcanic center through which much of the fumaroles are venting.

Due to terrain difficulties with the short timeframe given, it was not possible to cover to the north and northeast part of mount Alid with MT/TEM soundings. Therefore the results are to some extent inconclusive. To get a better picture on the resistivity structures, it is recommended that further resistivity survey should be done in these areas.

More geophysical methods should be employed to gain better understanding of the geothermal resource of the area. Tectonic activities play a major role in geothermal activity and therefore, to see if tectonic activities are taking place in Alid area, micro seismic survey is recommended. Gravity measurements provide valuable information about underground rock densities, which contribute to a better understanding of the subsurface geology. Intrusive bodies are more likely the heat sources for geothermal system and can be mapped with gravity surveys. Therefore, gravity survey is recommended as well.

References

Andemariam, T., Woldeyohannes, D., Misghina, M., 2006. Geology and hydrogeology of Alid and surrounding. *Eritrean Department of Mines, unpublished report*.

Árnason, K., Flóvenz, Ó., Georgsson, L.S., and Hersir, G.P., 1987. Resistivity structure of high-temperature geothermal systems in Iceland. *IUGG XIX General Assembly, Vancouver Canada, 1-22 August, abstract V, 477*.

Árnason, K., Björnsson G., Flóvenz, Ó.G., Haraldsson E.H., 1988. Geothermal Resistivity Survey in the Asal Rift in Djibouti. *Orkustofnun,* Reykjavík, report OS-88031/JHS-05, 48 PP.

Árnason, K., 1989. Central loop transient electromagnetic sounding over a horizontally layered earth. *Orkustofnun*, Reykjavík, report OS-89032/JHD-06, 129 pp.

Árnason, K., Flóvenz, Ó.G., 1992. Evaluation of physical methods in geothermal exploration of rifted volcanic crust. *GRC Transactions*, vol. 16, 207-217.

Árnason, K., Karlsdóttir, R., Eysteinsson, H., Flóvenz, Ó.G., Gudlaugsson, S.T., 2000. The Resistivity Structure of High-Temperature Geothermal Systems in Iceland. *Proceedings World Geothermal Congress*, Kyushu- Tohoku, 923-928.

Árnason, K., 2006a. TEMTD. Programme for 1D inversion of central-loop TEM and MT data. *Iceland GeoSurvey Report* ÍSOR, Reykjavík, short manual, 16 pp.

Árnason, K. 2006b. TemX. A Graphically Interactive Programme for Processing Central-loop TEM data. *Short Manual. Iceland GeoSurvey*. Unpublished ÍSOR internal Report. 17 pp.

Árnason, K.*,* 2008. The Magnetotelluric static shift problem. Reykjavík, *Iceland GeoSurvey Report* ÍSOR-08088, 16 pp.

Árnason, K., Eysteinsson, H., Hersir, G.P., 2010. Joint 1D inversion of TEM and MT data and 3D inversion of MT data in the Hengill area, SW Iceland. *Geothermics*, vol 39, 13-34.

Bahr, K., 1988. Interpretation of the magnetotelluric impedance tensor: regional induction and local telluric distortion, *J. Geophys*., 62, 119-127.

Barberi, F., and Varet Jacques., 1977. Volcanism of Afar: Small-scale plate tectonic implications. *Geological Society* of America Bulletin. v 88. p 1251-1266.

Berdichevsky, M.N., Dmitriev, V.I., 1976. Basic principles of interpretation of magnetotelluric curves. In: *Geoelectric and geothermal studies*. Adam, A., Ed., Akademini Kiado, 165-221.

Berdichevsky, M.N., Dmitriev, V.I., Kuznetsov, V.A., 1995. Bimodal two-dimensional interpretation of MT-soundings. Phys. Earth (Fizika Zemli), Vol. 31, No. 10, 821-837.

Berdichevsky, M. N., Dmitriev, V.I., Pozdnjakova, E. E., 1998. On two-dimensional interpretation of magnetotelluric soundings. *Geophys. J. Int.*, 133, 585-606.

Berdichevsky, M.N., Dmitriev, V.I., 2002. Magnetotellurics in the context of the theory of ill-posed problems. *Society of Exploration Geophysicists*, USA, 215 pp.

Berdichevsky, M.N., Dmitriev, V.I., 2008. Models and methods of magnetotellurics. *Sprinkler*, 561 pp.

Boerner, D. E., R. D. Kurtz, J. A. Craven, G. M. Ross, F. W. Jones, and W. J. Davis, 1999, Electrical conductivity in the Precambrian lithosphere of western Canada: *Science*, 283, 668–670.

Cagniard, L., 1953. Basic theory of the magneto-telluric method of geophysical prospecting: *Geophysics*, Soc. of Expl. Geophys., 18, 605-635.

Clarke. J., Gamble, T.D., Goubau, W. M., Koch, R. H., Miracky, R. F., 1983. Remote reference magnetotellurics: Equipment and procedures. *Geophys. Prosp.,* v., 31, 149-170.

Clynne, M.A., Duffield, W.A., Fournier, R.O., Weldegiorgis, L., Janik, C.J., Kahsai, G., Lowenstern, J., Weldemariam, K., and Tesfai, T., 1996: Geothermal potential of the Alid Volcanic Center, Danakil depression, Eritrea. *U.S. Geol. Survey*, final report to U.S. Agency for International Development under the terms of PASA No. AOT-0002-P-00-5033-00, 46 pp.

C.N.R.-C.N.R.S., 1973. Geology of northern Afar (Ethiopia): Revue de Geographie Physique et de Geologie dynamique, Vol.15, Fasc.4, 443-490.

Constable, C.S., Parker, R.L., Constable, C.G., 1987. Occam inversion: A practical algorithm for generating smooth models from electromagnetic sounding data. *Geophysics*, 52, 289-300.

Cumming, W., and Mackie, R., 2010. Resistivity imaging of geothermal resources using 1D, 2D and 3D MT inversion and TDEM static shift correction illustrated by a Glass Mountain case history, *Proceedings World Geothermal Congress 2010*, Bali, Indonesia, 25-29 April.

deGroot-Hedlin, C., Constable, S., 1990. Occam inversion to generate smooth, two dimensional models from magnetotelluric data. *Geophysics*, 55, 1613-1624.

Demidova T. A., Yegorov I. V. and Yanikyan V. O., 1985. Galvanic distortions of the magnetotelluric field of the lower Caucasus; *Geomagnetic Aeron.* **25**, 391-396

Duffield, W. A., Bullen, T. D., Clynne, M. A., Fournier, R. O., Janik, C. J., Lanphere, M. A., Lowenstern, J., Smith, J. G., Giorgis, L., Kahsai, G., Mariam, K. and Tesfai, T., 1997. Geothermal Potential of the Alid Volcanic Center, Danakil Depression, Eritrea. *US Geological Survey Open File Report* 97-291.

Eberhart-Phillips, Donna, Stanley, W.D., Rodriguez, B.D., and Lutter, W.J., 1995. Surface seismic and electrical methods to detect fluids related to faulting: *Journal of Geophysical Research*, v. 100, no. B7, 12919-12936.

Eysteinsson, H., and Hermance J.F., 1985. Magnetotelluric measurements across the eastern neovolcanic zone in south Iceland, *J. Geophys. Res.*, Vol. 90, 10093–10103.

Eysteinsson, H., Teklesenbet, A., Rosenkjær, G.K., Karlsdóttir, R. 2009. Resistivity Survey in Alid geothermal area, Eritrea. *Iceland GeoSurvey*, ÍSOR-2009/016, 115 s.

Gamble, T.D., Goubau, W.M., Clarke, J., 1979. Magnetotellurics with a remote magnetic Reference. *Geophysics*, V. 44, 53-68.

Goitom, B., Teklesenbet, A., Beraki, M., 2006. Resistivity survey for geothermal exploration at Alid area. *Department of Mines, Eritrea*,Unpublished report.

Goubau. W.M., Gamble. T.D., Clarke. J., 1979. Magnetotelluric data analysis: removal of bias. *Geophysics*, V. 43. p. 1157-1169.

Groom, R.W., Bailey, R.C., 1989. Decomposition of the magnetotelluric impedance tensor in the presence of local three-dimensional galvanic distortion. *J. Geophys. Res.*, 94, 1913-1925.

Han, N., Nam, M.J., Kim, H.J., Lee, T.J., Song, Y., Suh, J.H., 2008. Efficient three-dimensional inversion of Magnetotelluric data using approximate sensitivities, *Geophys*. J. Inter, 175, 477-485.

Hayward, N.J., Ebinger, C.J., 1996. Variations in the along-axis segmentation of the Afar Rift System, *Tectonics,* 15, 244–257.

Hersir, G.P., and Björnsson, A., 1991. Geophysical exploration for geothermal resources. Principles and applications. *UNU-GTP*, Iceland, report 15, 94 pp.

Hirn, A., Le´pine, J. C., Sapine, M., 1993. Triple junction and ridge hot spots: Earthquakes, faults, and volcanism in Afar, the Azores, and Iceland. J. *Geophys*. Res. 98, 11995-12001.

http://earthquake-report.com, 2011.

http://volcanoes.usgs.gov/yvo/aboutus/jlowenstern/alid/alidmaps.html (Alid Home Page).

http://www.phoenix-geophysics.com/home.

http://www.shabait.com, 2011.

http://www.swisseduc.ch/stromboli/perm/erta/lava-lake,2008.

Ingham, M. R., 1988. The use of invariant impedances in magnetotelluric interpretation. *Geophysical Journal, 92,* 165–169.

Jiracek, G., 1990. Near-surface and topographic distortions in electromagnetic induction. *Surv. Geophys.*, 11,163-203.

Jones, A.G., 1988. Static shift of magnetotelluric data in a sedimentary basin environment. *Geophysics*, 53: 967–978.

Keller, G.V., and Frischknecht, F.C., 1966. Electrical methods in geophysical prospecting. *Pergamon Press Ltd*., Oxford, 527 pp

Keller, G.V., 1989. Electrical properties. In*:* Carmichael, R.S., ed., Practical handbook of physical properties of rocks and minerals: *Boca Raton, Fla*., CRC Press, p. 359-427.

Lemma, Y., 2010. Multidimensional Inversion of MT data from Krýsuvík High Temperature Geothermal Field, SW-Iceland, and study how 1D and 2D inversion can reproduce a given 2D/3D resistivity structure using synthetic MT data. *Master′s thesis,* Faculty of Earth Sciences, University of Iceland, pp.119.

Levenberg, K. (1944). A Method for the Solution of Certain Non-Linear Problems in Least Squares. The Quarterly of Applied Mathematics 2: 164−168.

Lowenstern, J. B., Janik, C. J., Fournier, R. O., Tesfai, T., Duffield, W. A., Clynne, M. A., Smith, J. G., Woldegiorgis, L., Weldemariam, K. and Kahsai, G., 1999. A geochemical reconnaissance of the Alid volcanic center and the geothermal system, Danakil depression, Eritrea. *Geothermics*. P 161−187.

Mackie, R.L., Bennett, B.R., Madden, T.R., 1988. Long period magnetotelluric measurements near the central California coast: A land-locked view of the conductivity structure under the Pacific Ocean. *Geophys. J. R. Astron. Soc*., 95, 181-194.

Mackie, R. L., J. T. Smith, and Madden, T. R., 1994. Three-dimensional electromagnetic modeling using finite difference equations: The magnetotelluric example, *Radio Science*, 29, 923–935.

Marini, A., 1938. Il Vulcano Alid nella Colonia Eritrea. *L'Universo* 19**,** 131–170.

Marquardt, D. (1963). An Algorithm for Least-Squares Estimation of Nonlinear Parameters. *SIAM Journal* on Applied Mathematics 11: 431−441.

Martinelli, P., Osella, A., and Pomposiello, C., 2000. Comparative magnetotelluric modeling of smooth 2D and 3D conducting bodies using Rayleigh-Fourier codes: Pure Appl. *Geophys*., 157, 383–405

McNeill, J.D., 1990, Use of electromagnetic methods for groundwater studies: in *Geotechnical and Environmental Geophysics*, ed: S.H.Ward, SEG, IG#5, Vol. 1: P.191-218.

Nelson, P.H., and Anderson, L.A., 1992. Physical properties of ash flow tuff from Yucca Mountain, Nevada: *Journal of Geophysical Research*, v. 97, no. B5, p. 823-6841.

Newman, G.A., Gasperikova, E., Hoversten, G.M., and Wannamaker, P. E., 2008. Three-dimensional magnetotelluric characterization of the Coso geothermal field, *Geothermics* Volume 37, Issue 4, 369-399.

Park, S. K. and Livelybrook, D. W., 1989. Quantitative interpretation of rotationally invariant parameters in magnetotellurics. *Geophysics, 54*, 1483–1490.

Parkinson, W.D., 1959. Direction of rapid geomagnetic fluctuations. *Geophys. J. R. Astron. Soc.*, 2: 1-14.

Pedersen, L. B., Engels, M., 2005. Routine 2D inversion of magnetotelluric data using the determinant of the impedance tensor. *Geophysics*, Vol. 70, No. 2.

Pellerin, L., Hohmann, G.W., 1990. Transient electromagnetic inversion: A remedy for magnetotelluric static shifts. *Geophysics*, *55-9,* 1242-1250.

Pellerin, L., Johnston, J.M., Hohmann, G.W., 1996. Numerical evaluation of electromagnetic methods in geothermal exploration. Geophysics, Vol. 61, NO. 1; P. 121-130.

Phoenix Geophysics, 2005. Data Processing User Guide, *Phoenix Geophysics Limited*, 3781 Victoria Park Avenue, unit 3, Toronto, ON Canada M1W 3K5.

Ranganayaki, R.P., Madden, T.R., 1980. Generalized thin sheet analysis in magnetotellrics: An extension of Price's analysis, *Geophys. J. R. Astro. Soc.*, 60, 445-457.

Ranganayaki, R.P., 1984. An interpretative analysis of magnetotelluric data. *Geophysics* 49: 1730-1748.

Reddy, I.K., Rankin, D., Phillips, R.J. 1977. Three-dimensional modelling in Magnetotelluric and Magnetic variational sounding. *Geophys. J. R. Astr. Soc.* 51, 313-325.

Romo J. M., Flores C., Vega R., Vazquez R., Perez Flores M .A., Gomez-Trevino E., Esparza F. Z., Quizano J.E and Garcia V. H., 1997. A closely spaced magnetotelluric study of the Ahuachapan-Chipilapa geothermal fields, El Salvador; *Geothermics* 26, 627-656.

Rowland, B.F., 2002: Time-domain electromagnetic exploration. *Northwest Geophysical Associates*, Inc., 6 pp.

Ruegg, J. C., Briole, P., Feigl, K. L., Orsoni, A., Vigny, C., Abdalla, M. A., Bellier, O., de Chabalier, J. B., Huchon, P., Jacques, E., 1993. First epoch geodetic GPS measurements across the Afar plate boundary zone. *Geophys*. Res. Lett. 20, 1899-1902.

SEG, 1991: *MT/EMAP* data interchange standard. *Society of Exploration Geophysicists*, 112 pp.

Sharka, L., and Menvielle, M., 1997. Analysis of rotational invariants of the magnetotelluric impedance tensor, *Geophysics*. J. Int. 129, 133-142.

Simpson, F., Bahr, K., 2005. *Practical magnetotellurics. Cambridge University Press*, Cambridge, UK, 254 pp.

Siripunvaraporn, W., Egbert, 1999. *Software documentation and user manual a Reduced Basis Occam (REBOCC) inversion version 1.0 for Two-dimensional magnetotelluric data.* College of Oceanic and Atmospheric Sciences, Oregon State University, Corvallis, 97331, 19 pp.

Siripunvaraporn, W., Egbert, G., 2000. An efficient data-subspace inversion method for 2-D Magnetotelluric data. *Geophysics*, 65, 791-803.

Siripunvaraporn,W., Egbert, G., Lenbury,Y., 2002. Numerical accuracy of magnetotelluric modeling: a comparison of finite difference approximations. *Earth Planets Space* 54, 721–725.

Siripunvaraporn,W., Egbert, G., Lenbury, Y., Uyeshima, M., 2005. Three-dimensional magnetotelluric inversion: data-space method. *Phys. Earth Planet. Interiors* 150, 3–14.

Siripunvaraporn,W., Egbert, G., Lenbury, Y., Uyeshima, M., 2006. *WSINV3DMT version 1.0.0 for single processor Machine User Manual.* Department of physics, Faculty of science, Mahidol University, Rama 6 Rd., Rachatawee, Bangkok 10400, Thailand. 21 pp.

Smith, J.T., Booker, J.R., 1991. Rapid Inversion of Two- and Three- Dimensional Magnetotelluric Data. *J. Geophys. Res.,* 96, 3905-3922.

Sternberg, B.K., Washburne, J.C., Pellerin, L., 1988. Correction for the static shift in magnetotellurics using transient electromagnetic soundings. *Geophysics,* vol. 53, p. 1459-1468.

Swift, C. M., 1967. A magnetotelluric investigation of an electric conductivity anomaly in the south-western U.S.: Ph.D. Thesis, MIT, 211 p.

Tikhonov, A. N., 1950. The determination of electrical properties of the deep layers of the Earth's crust. Dokl. Acad. Nauk. SSR 73: 295-297 (in Russian).

Vozoff, K., 1972. The magnetotelluric method in the exploration of sedimentary basins. *Geophysics,* Soc. of Expl. Geophys., 37, 98-141.

Vozoff, K., 1991. The magnetotelluric method. In: *Electromagnetic Methods in Applied Geophysics*. Vol 2 Application. Soc. Expl. Geophys., Tulsa, OK., 972 pp.

Wannamaker, P.E., Hohmann, G.W., Ward, S. H., 1984. Magnetotelluric responses of three-dimensional bodies in layered earth. *Geophysics*, 49**,** 1517–1533.

Ward, S.H, and Wannamaker, P.E., 1983. The MT/AMT electromagnetic method in geothermal exploration. UNU-GTP, Iceland, report 5, 107 pp.

Wiese, H., 1962. Geomagnetische Tiefentellurik, Teil 2, Die Streichrichtung der Untergrundstrukturen des elektrischen Winderstandes, ersclossen aus geomagnetischen Variationen, *Geofis*. Pura. Appl. 52, 83-103.

Yohannes E., 2004. Geothermal interpretation of thermal water and gas samples from Krysuvik, Iceland and Alid, Eritrea. Report 18 in: *Geothermal Training in Iceland 2004.* UNU-GTP, Iceland, 403-438.

Yohannes, E., Ghebrehiwet, K., and Habte, B., 2006. Assessment of fractures and faults of alid geothermal area. Eritrean Department of Mines, unpublished report.

# APPENDIX A: Location and elevation of TEM and MT soundings

TABLE A.1: Location and elevation of TEM and MT soundings. Location in UTM coordinate system zone 37 and datum is WGS84. All values are in meters.

	TEM				MT		
Name	EW	NS	Elevation	Name	EW	NS	Elevation
ALI001	593004	1643999	163	013	592980	1643986	169
ALI002	592992	1645003	152	002	593044	1645028	156
ALI003	593016	1645982	140	003	593016	1645989	140
ALI004	594056	1642001	218	004	593920	1641977	203
ALI005	593980	1643000	227	005	594128	1642847	204
ALI006	593980	1643988	178	006	594076	1644055	194
ALI007	593996	1645003	165	007	593996	1645001	167
ALI008	593998	1646005	157	008	593992	1646002	156
ALI009	593948	1646857	155	009	594084	1646679	155
ALI010	595008	1641001	174	010	595000	1640979	175
ALI011	595008	1641987	148	011	595064	1642000	175
ALI012	595012	1643005	232	012	594852	1643093	228
ALI013	594988	1644013	237	001	594876	1643947	250
ALI014	594840	1645050	217	014	594956	1644986	219
ALI015	594964	1645995	202	015	595008	1646000	200
ALI016	594944	1646992	195	016	594896	1646940	195
ALI018	596000	1640000	165	018	596004	1639969	165
ALI019	596012	1641014	166	019	595936	1641004	167
ALI020	596000	1642007	176	020	595988	1641914	177
ALI022	595704	1645939	244	022	595720	1645972	245
ALI023	595932	1646963	204	023	595888	1646898	205
ALI026	596936	1639915	163	026	596700	1639837	162
ALI027	596960	1640712	167	027	596872	1640956	165
ALI028	596972	1641885	188	028	597020	1641866	188
ALI029	597528	1644206	560	029	597468	1644274	570
ALI030	596752	1643806	651	030	596716	1643831	651
ALI031	597080	1646798	218	031	597072	1646813	209
ALI035	597976	1640002	166	035	598036	1639965	156
ALI036	597993	1640984	124	036	597828	1640975	130
ALI037	598058	1641808	115	037	597988	1641941	123
ALI038	598356	1644156	619	038	598328	1644259	603
ALI039	598432	1644983	587	039	598416	1644926	589
ALI040	597644	1644986	595	040	597612	1644797	573
ALI046	599004	1641873	134	046	599132	1641991	122
ALI047	599192	1644217	618	047	599200	1644229	601
ALI048	599176	1645008	597	048	599080	1645006	597
ALI054	599968	1641947	117	054	600024	1641974	108
ALI060	600868	1642173	71	060	600916	1642232	80

ALI061	601116	1642980	76	061	601012	1642900	90
ALI068	602012	1643015	82	068	601992	1643045	86
ALI069	601992	1643995	122	069	602040	1643933	114
ALI074	593008	1642994	190	074	592972	1643055	190
ALI075	603040	1643913	86				
ALI076	603000	1643000	79	076	603024	1643013	71
ALI077	592000	1645001	161	077	591984	1644956	161
ALI078	591016	1645015	181	078	590984	1644964	187
ALI079	589996	1645093	197	079	590012	1645096	198
ALI080	589160	1645264	190	080	589132	1645262	183
ALI081	588004	1645579	214	081	588076	1645792	194
ALI082	591984	1646019	163				
ALI083	596964	1638991	160				
ALI084	597632	1637979	150	084	597564	1637957	146
ALI085	598456	1637024	106	085	598520	1637005	103
ALI086	599028	1636086	103				
ALI088	600712	1634086	62				
ALI089	601012	1633080	53				
ALI090	601528	1631624	20	000	601464	1631600	27
ALI091	591172	1647070	138				
ALI092	590424	1648286	122				
ALI093	589716	1649497	118				
ALI094	589048	1650805	115				
ALI095	594028	1640794	220				
ALI097	592992	1641935	260				
ALI098	593024	1640863	218				
ALI099	595028	1639880	182				
ALI101	588480	1651899	83				

APPENDIX B: 1D joint inversion of TEM and MT
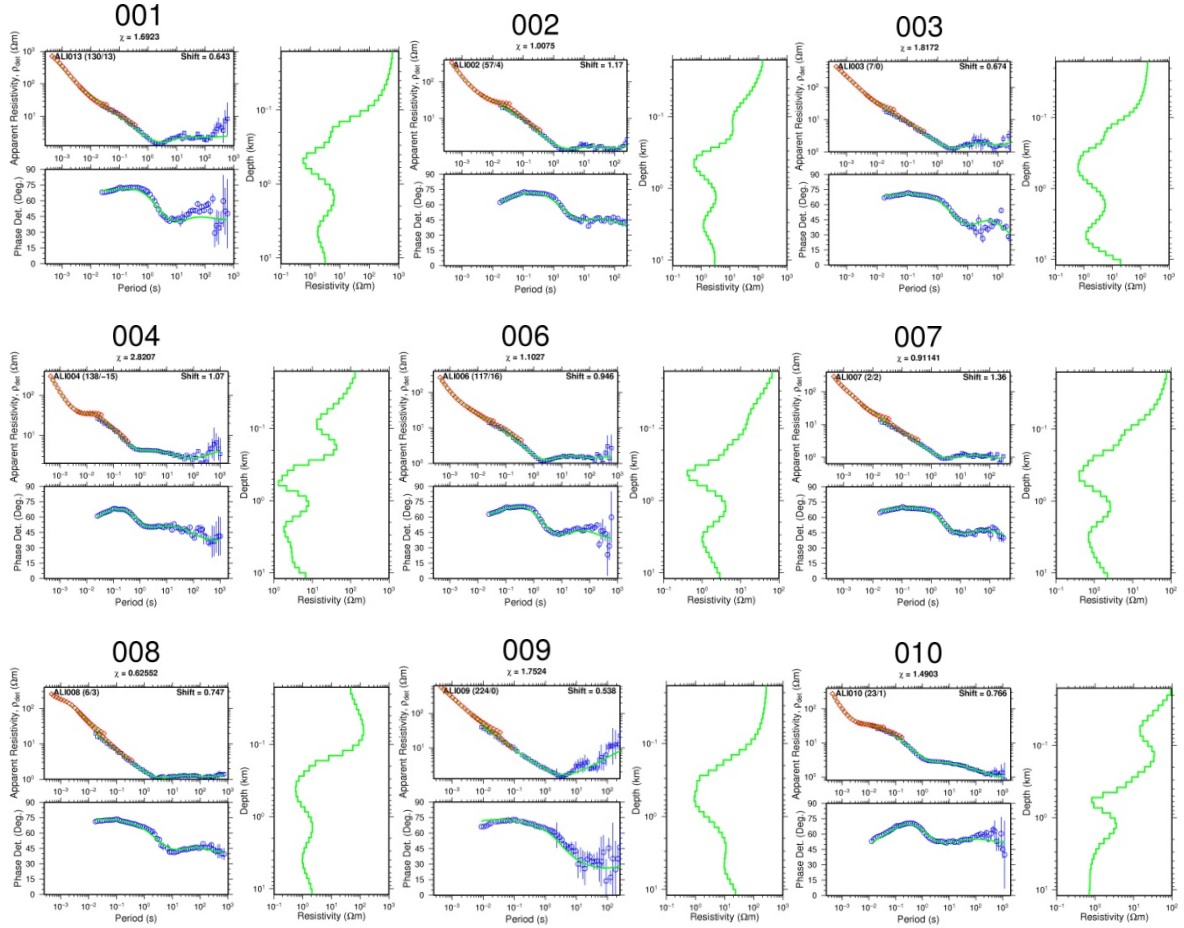
Figure B: *Model results of 1D joint inversion of TEM and MT data. Red diamonds are measured TEM data. Blue squares and blue circles are measured MT apparent resistivities and phases, respectively obtained from the determinant of the MT impedance tensor. The solid curves in the left panels are calculated responses from the Occam inversion model to the right. Number on the top of the figure: name of the MT station; number below the MT station: chi; number in the upper left panel: name of the TEM station. The static shift is shown in the upper right hand corner of the apparent resistivity panel. The numbers in parenthesis indicate that MT and TEM stations were separated in horizontal distance and elevation, respectively in meters by those numbers.*

The TEM data is plotted as a function of the period (T), but is actually measured as a function of time from current turn off (t). The transformation used is an empirical one suggested by Sternberg et al., 1988, where T=t/0.2.
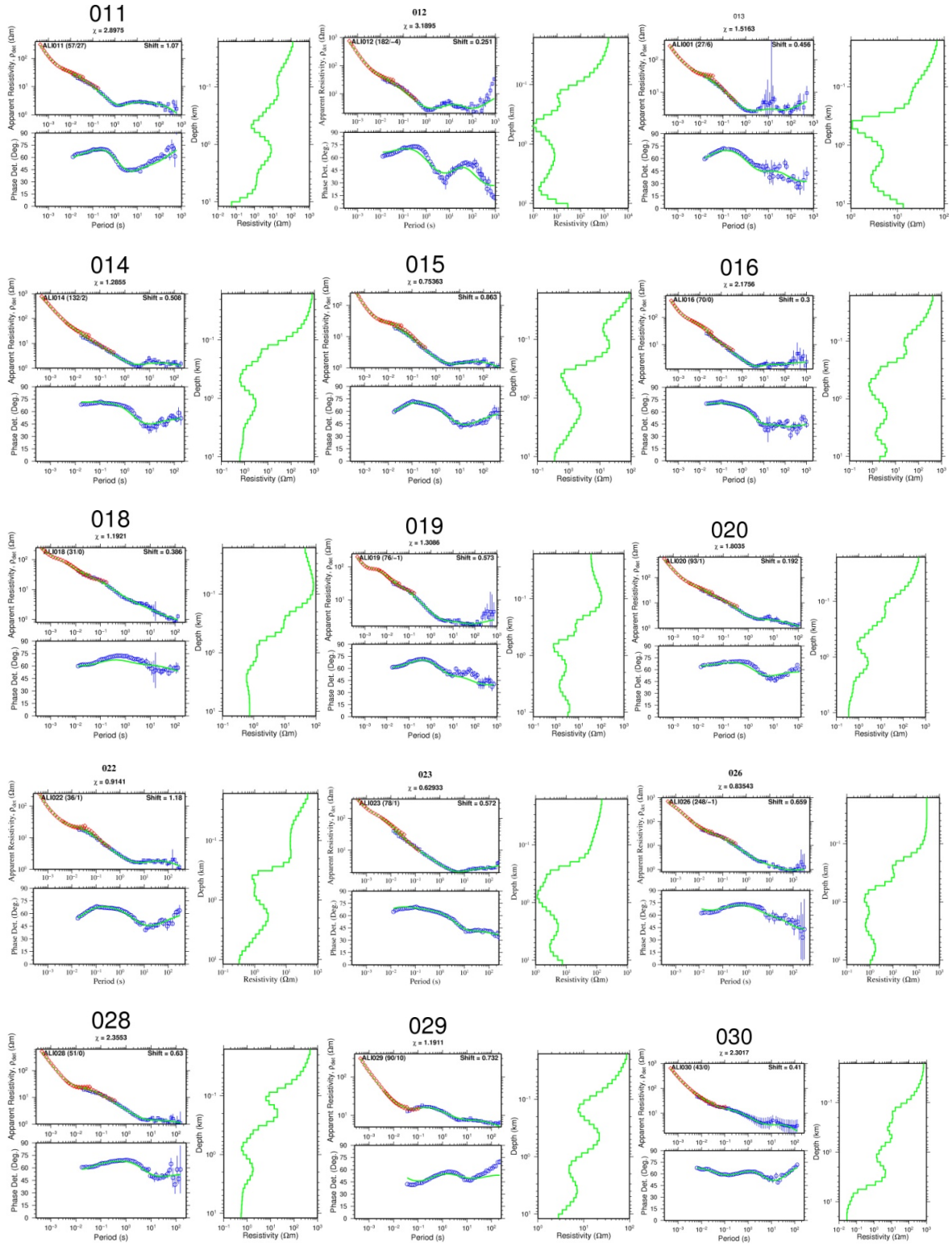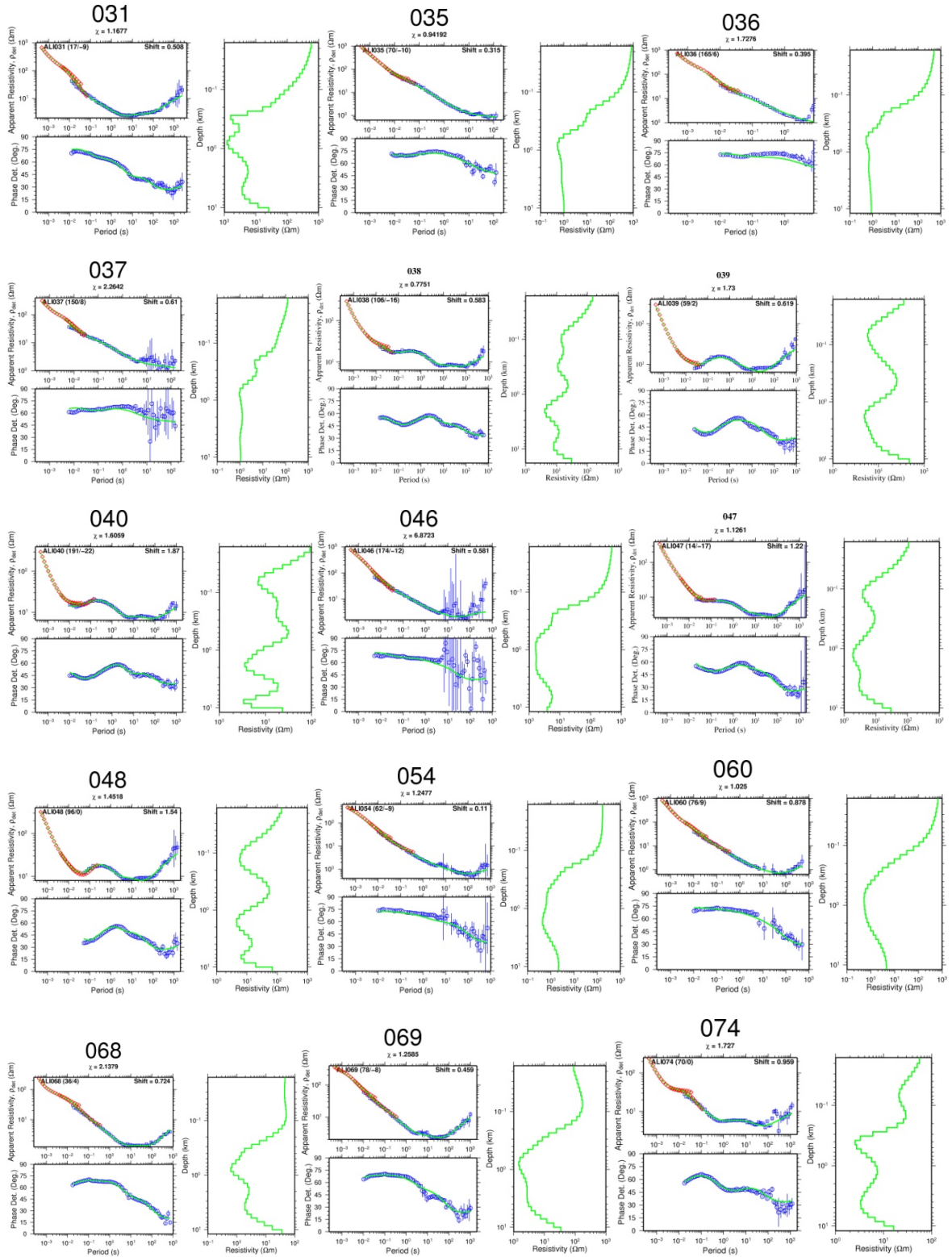
Figure B: *Continued.*

Figure B: *Continued.*

076

077

078

079

080

081

084

085
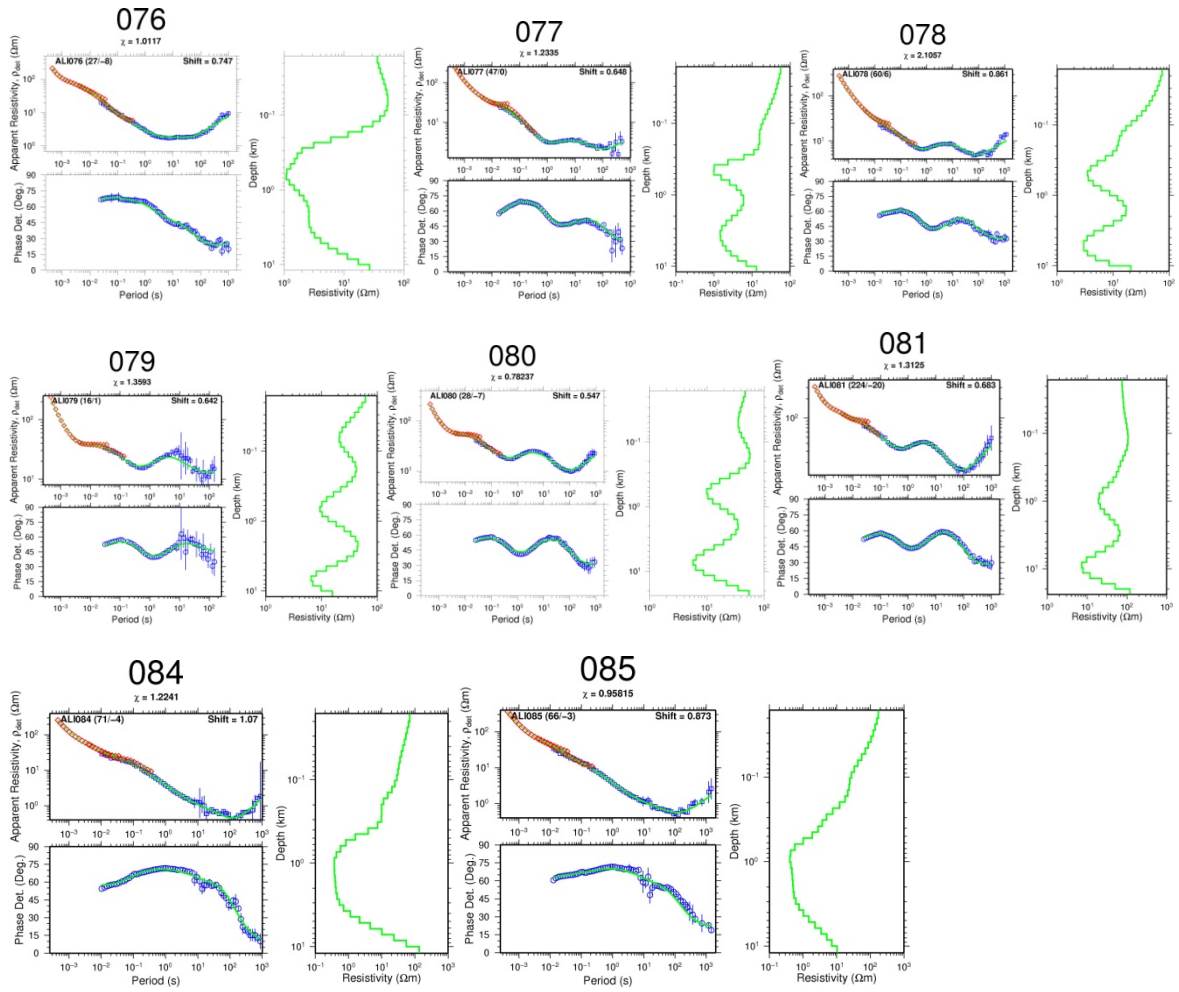
Figure B: *Continued.*

APPENDIX C: 2D Inversion responses
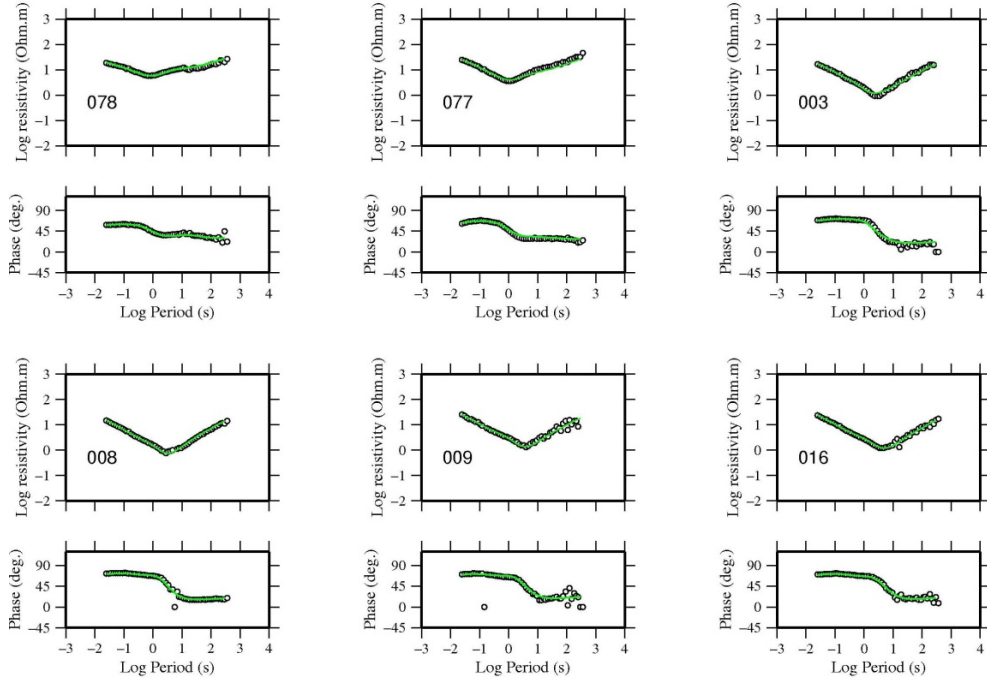
Figure C.1: *Fit of the 2D inversion TE mode apparent resistivity ρ_a in (Ωm) and phase ϕ in (°) of MT sites on Profile ac4000. Solid green curves show the response of the inversion model. The black circles are measured MT data points.*
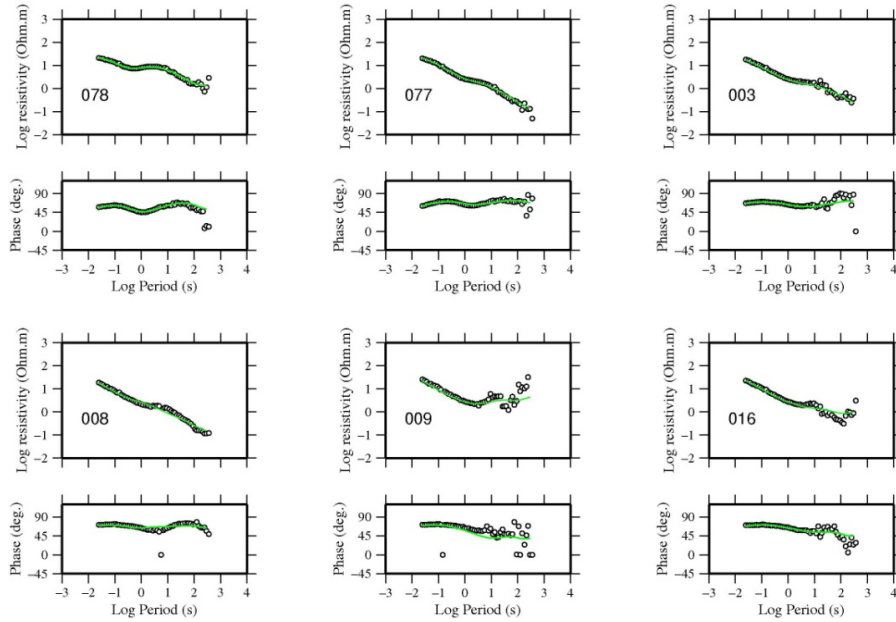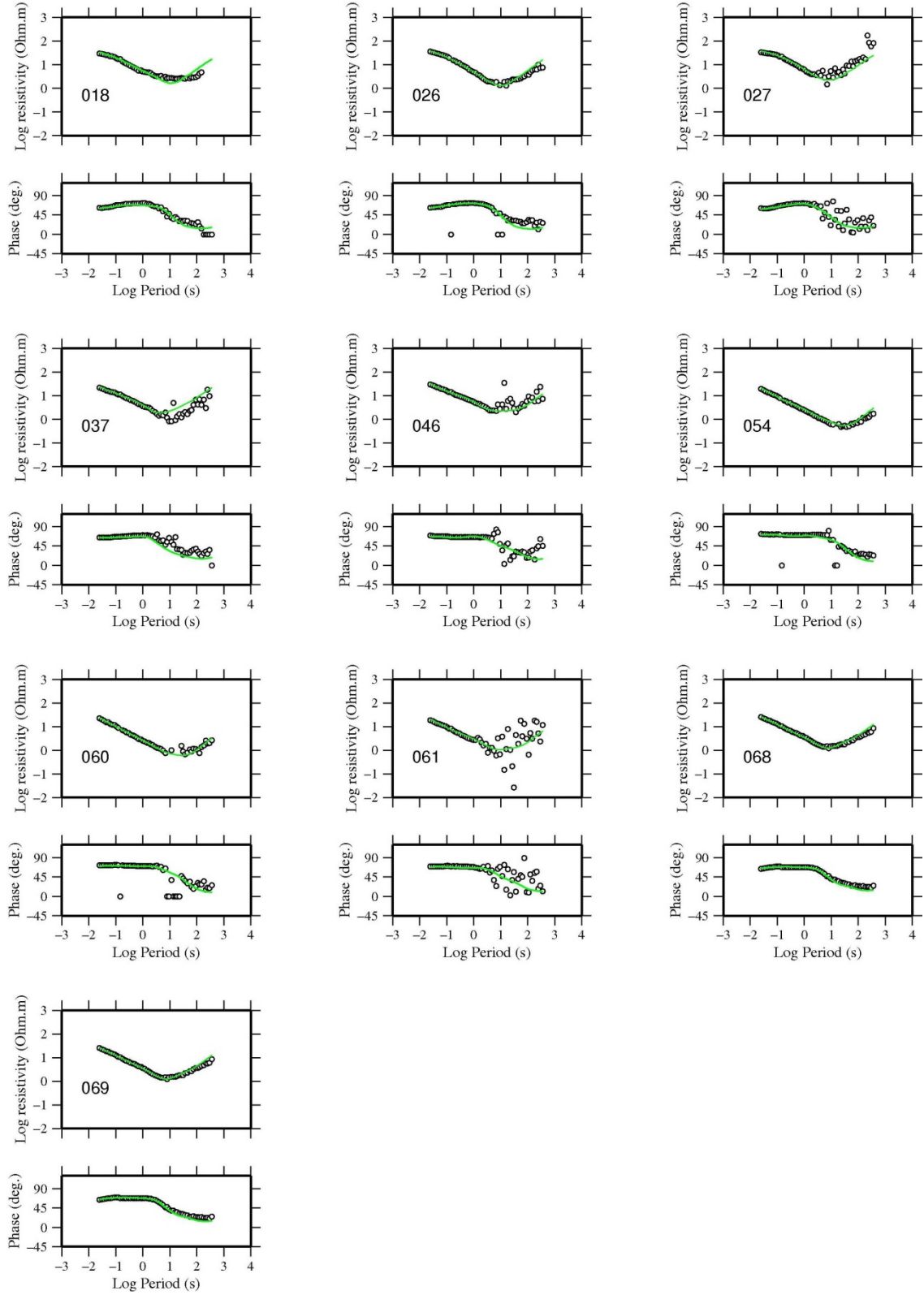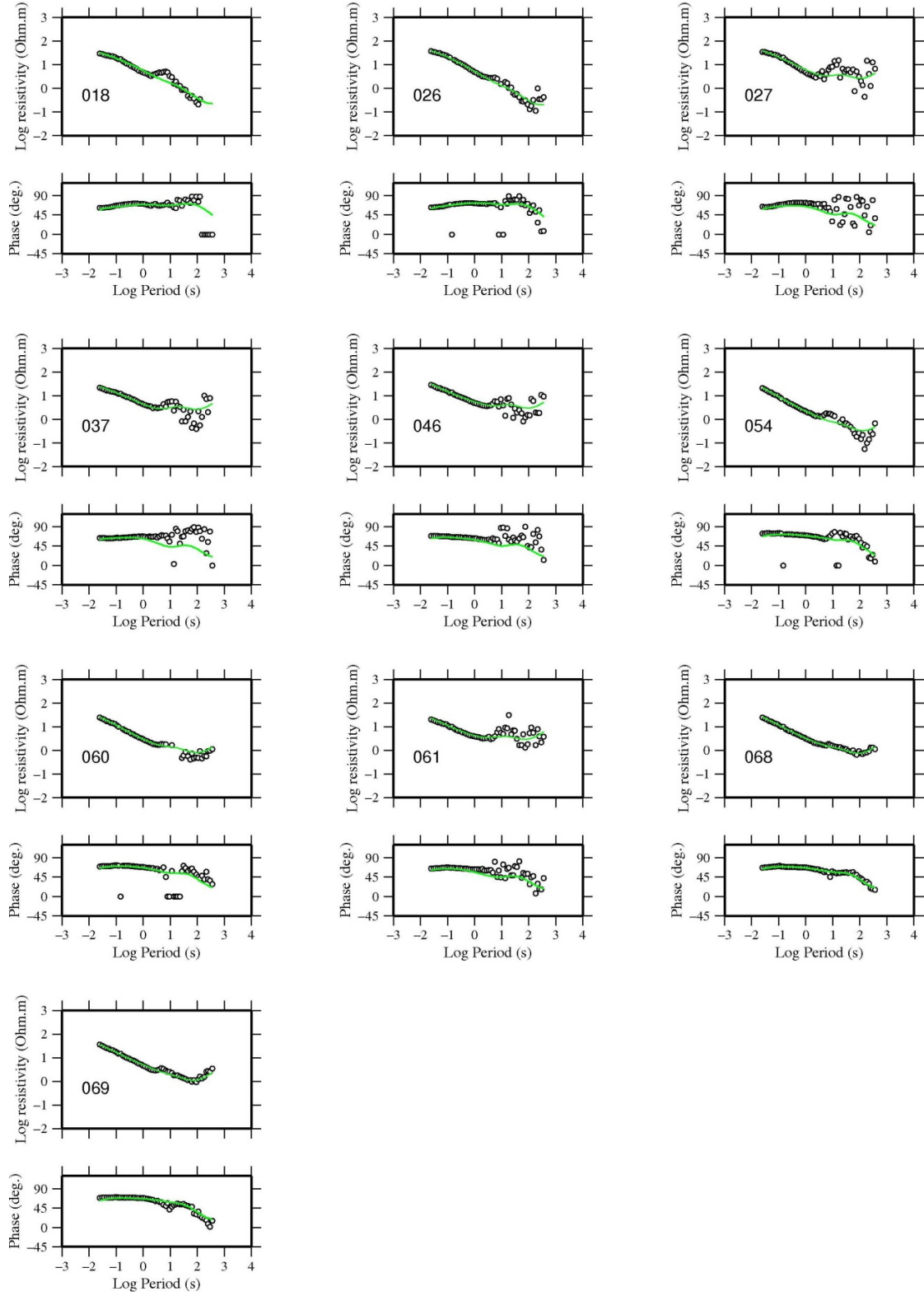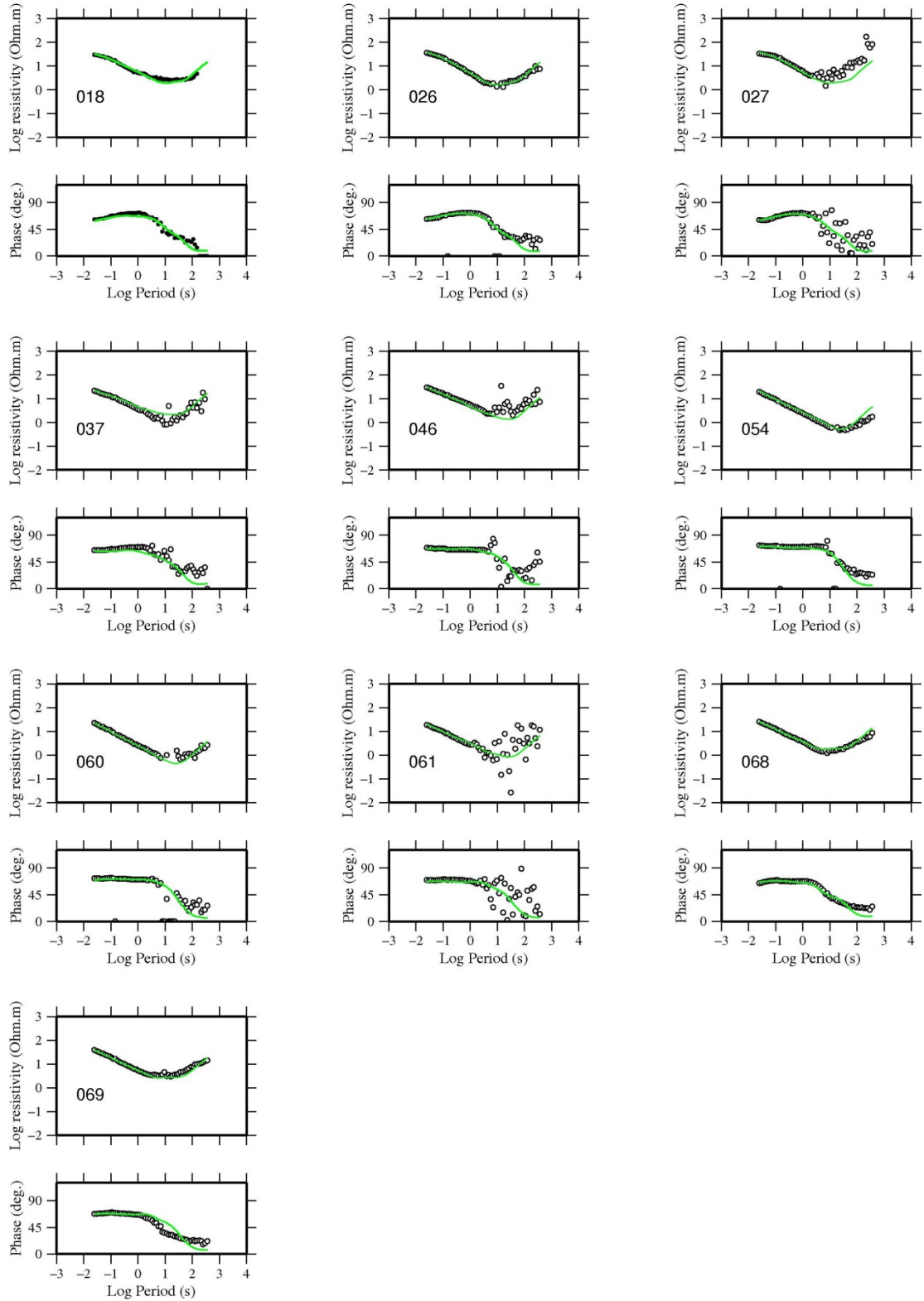

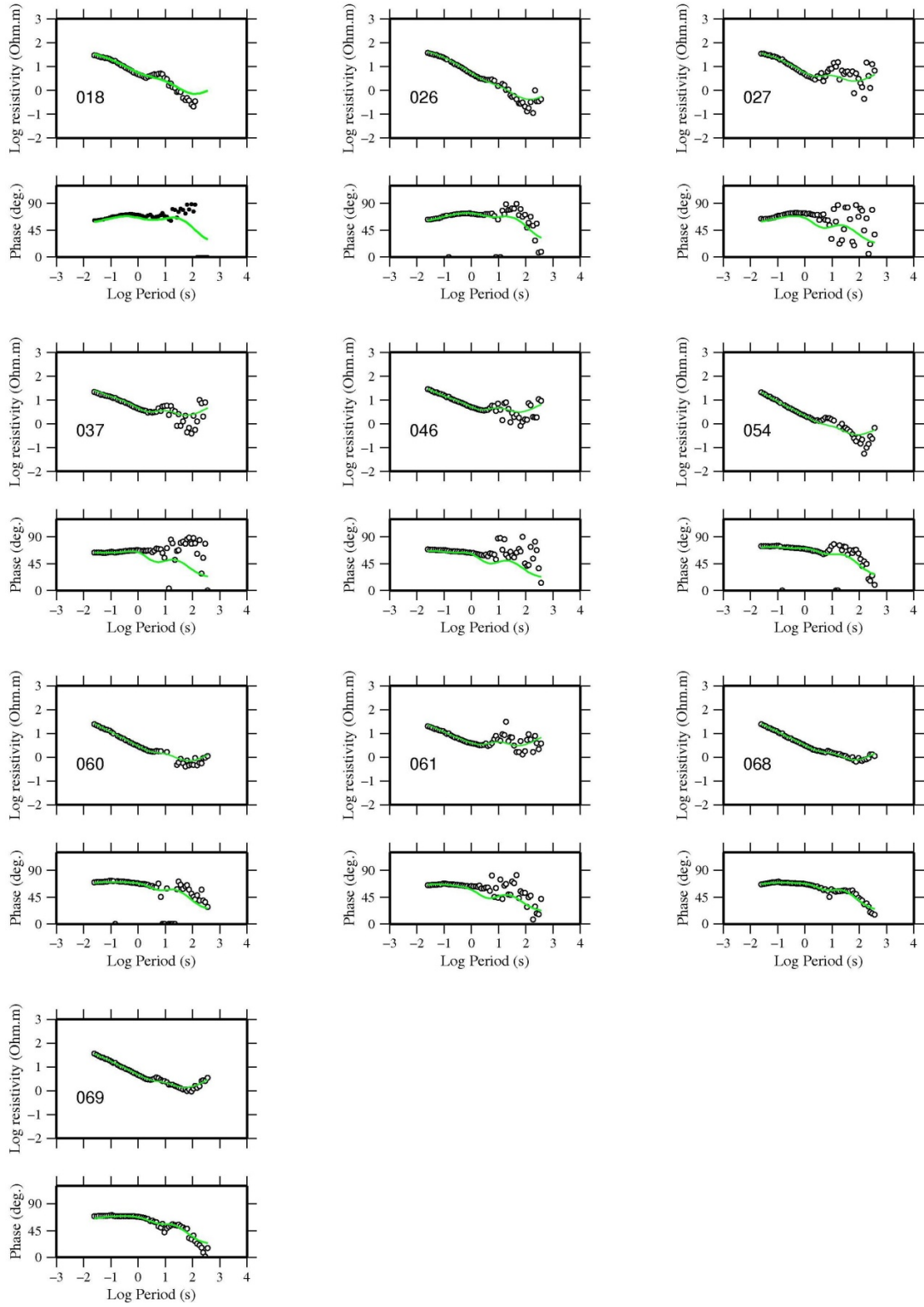***Figure C.2:*** *Fit of the 2D inversion TM mode apparent resistivity ρ_a in (Ωm) and phase ϕ in (°) of MT sites on Profile ac4000. Solid green curves show the response of the inversion model. The black circles are measured MT data points.*
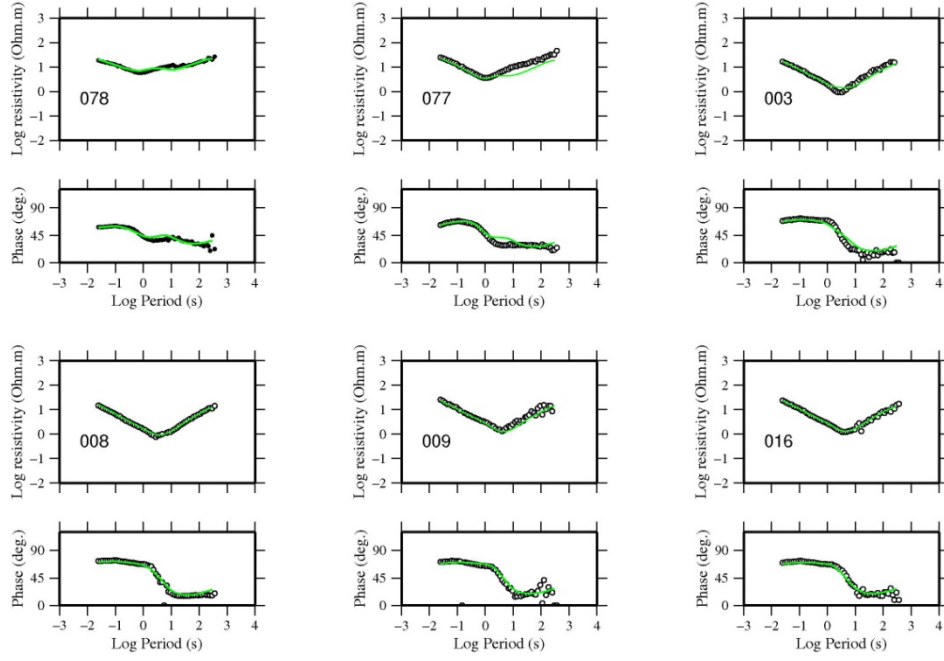
Figure C.3: *Fit of TE mode in joint TE and TM mode inversion apparent resistivity ρ$_a$ in (Ωm) and phase φ in (°) of MT sites on Profile ac4000. Solid green curves show the response of the inversion model. The black circles are measured MT data points.*
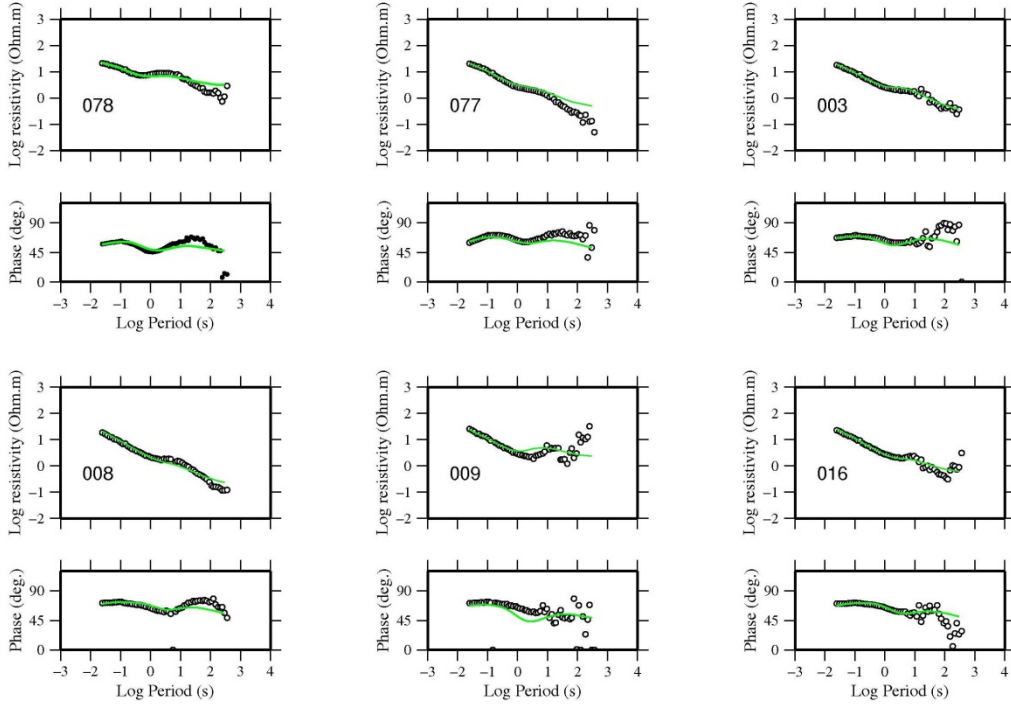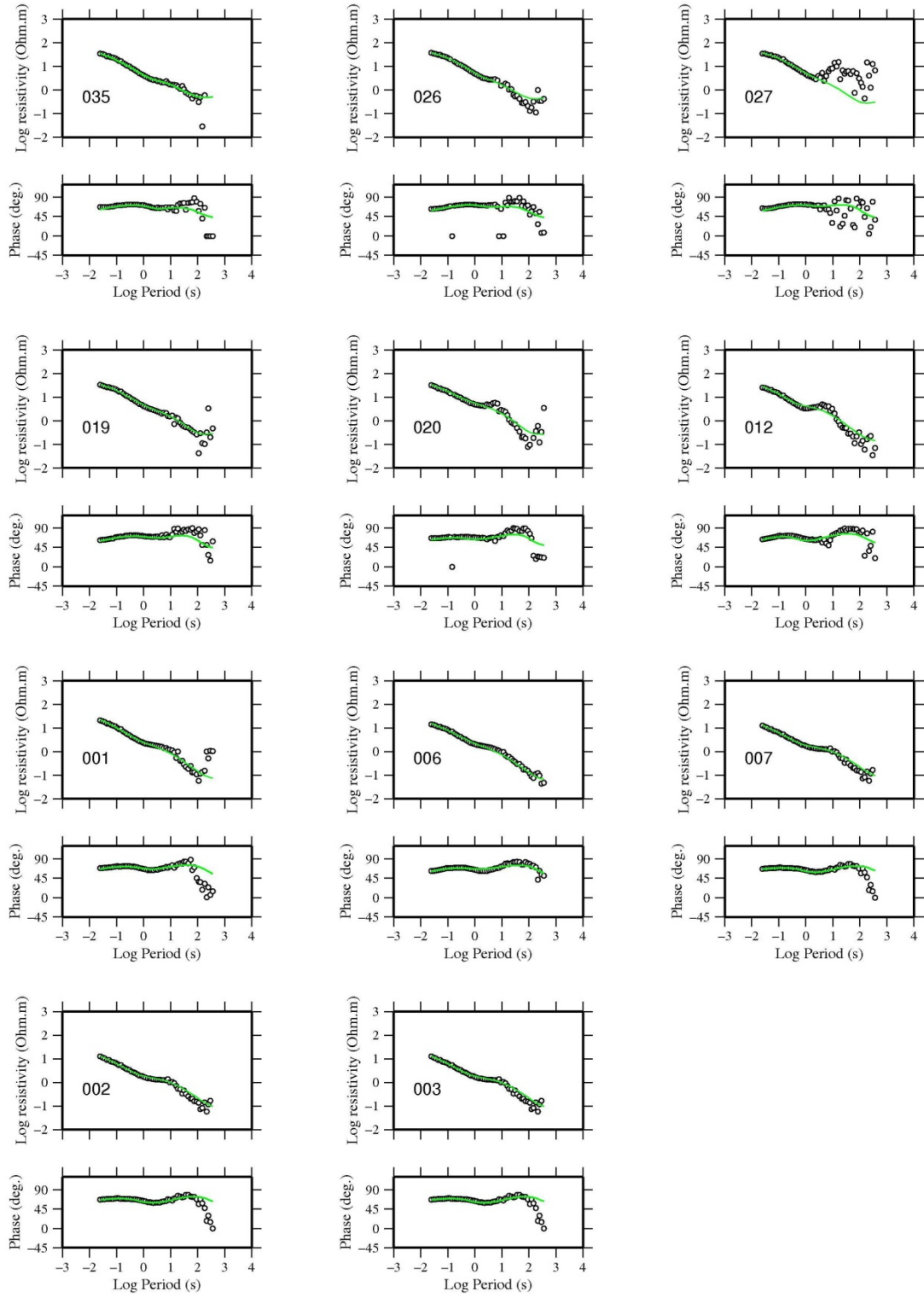

Figure C.4: *Fit of TM mode in joint TE and TM mode inversion apparent resistivity ρ$_a$ in (Ωm) and phase φ in (°) of MT sites on Profile ac4000. Solid green curves show the response of the inversion model. The black circles are measured MT data points.*
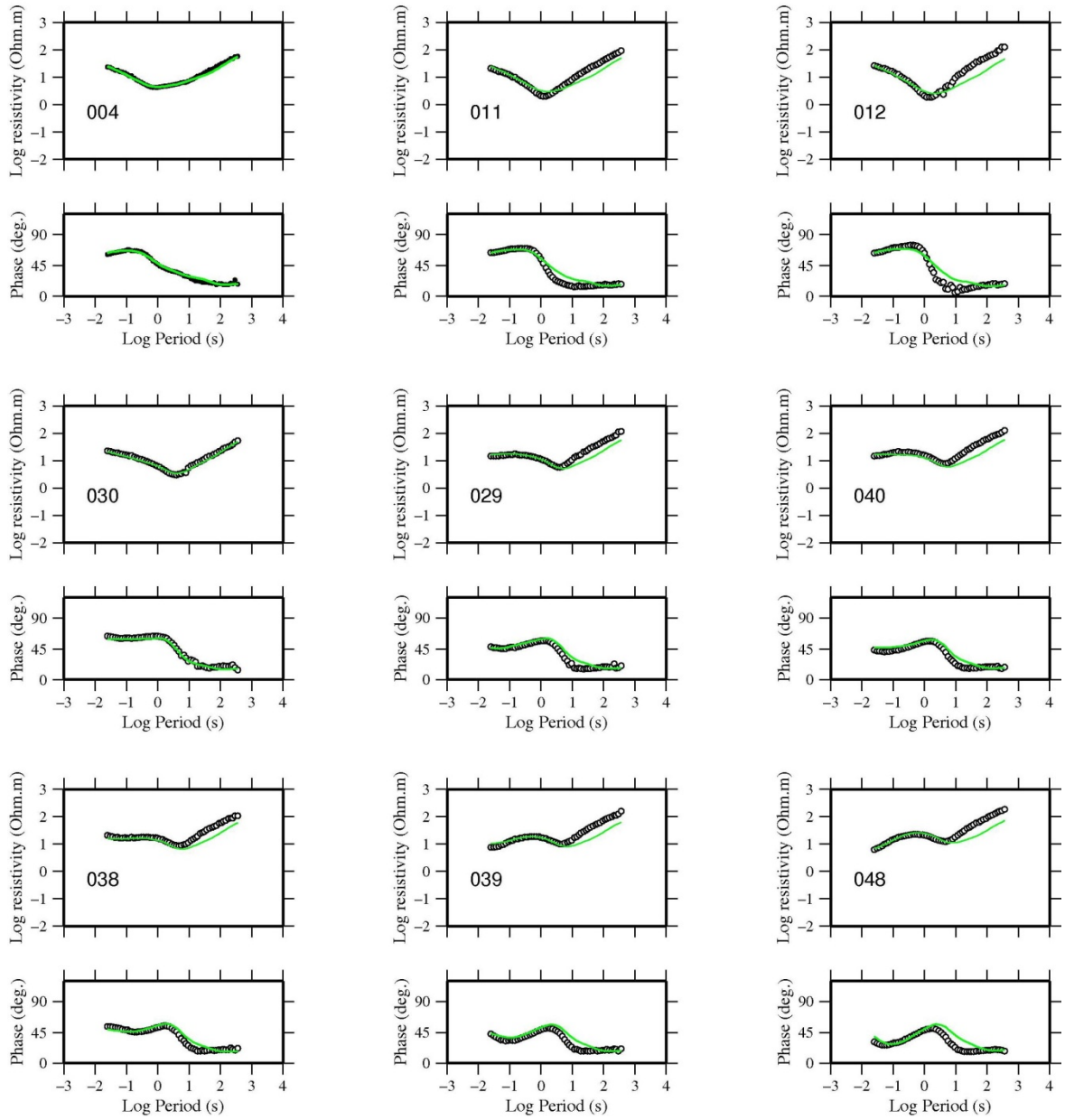
Figure C.5: *Fit of TE mode in joint TE and TM mode inversion apparent resistivity ρₐ in (Ωm) and phase φ in (°) of MT sites on Profile-2. Solid green curves show the response of the inversion model. The black circles are measured MT data points.*
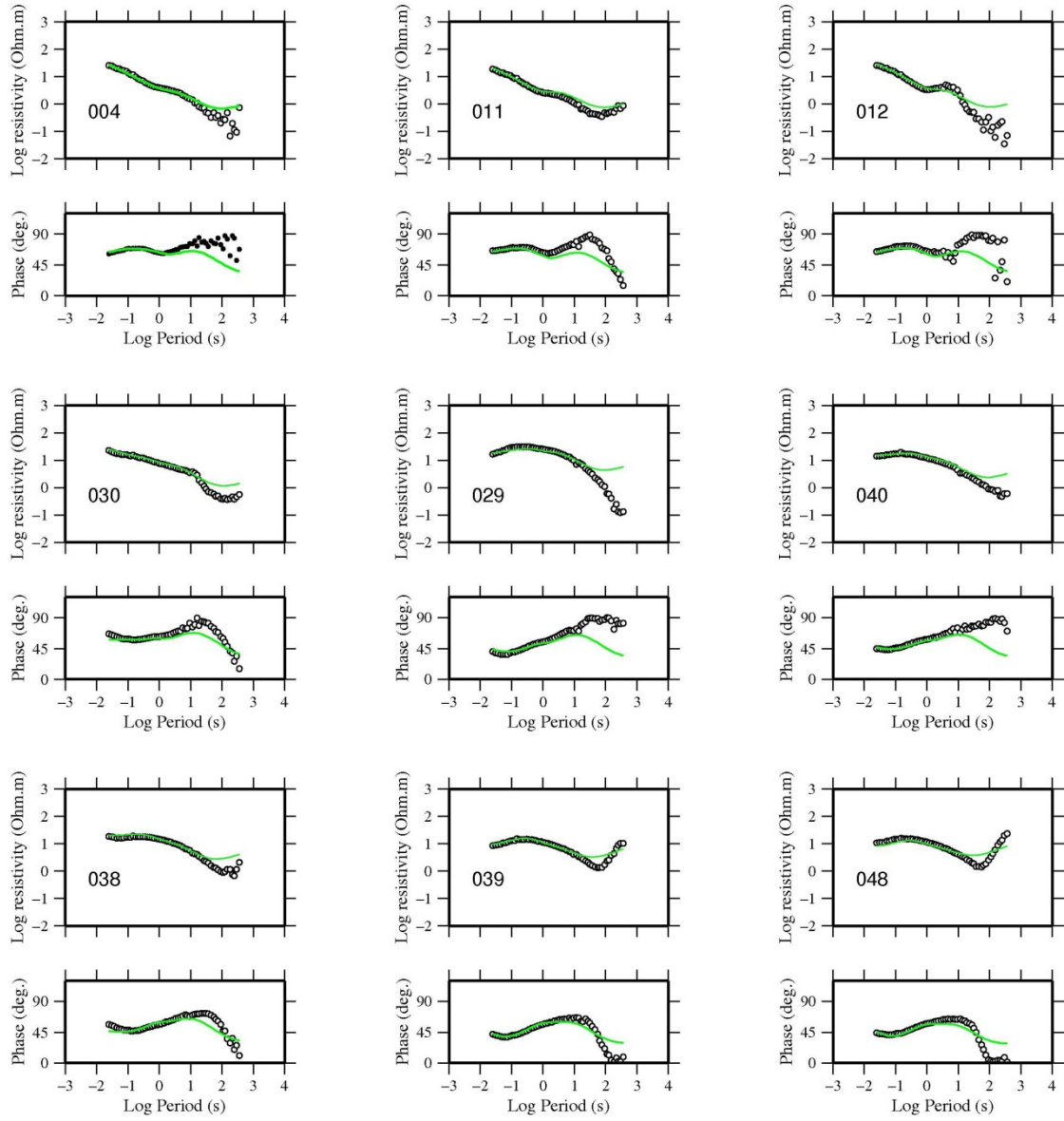
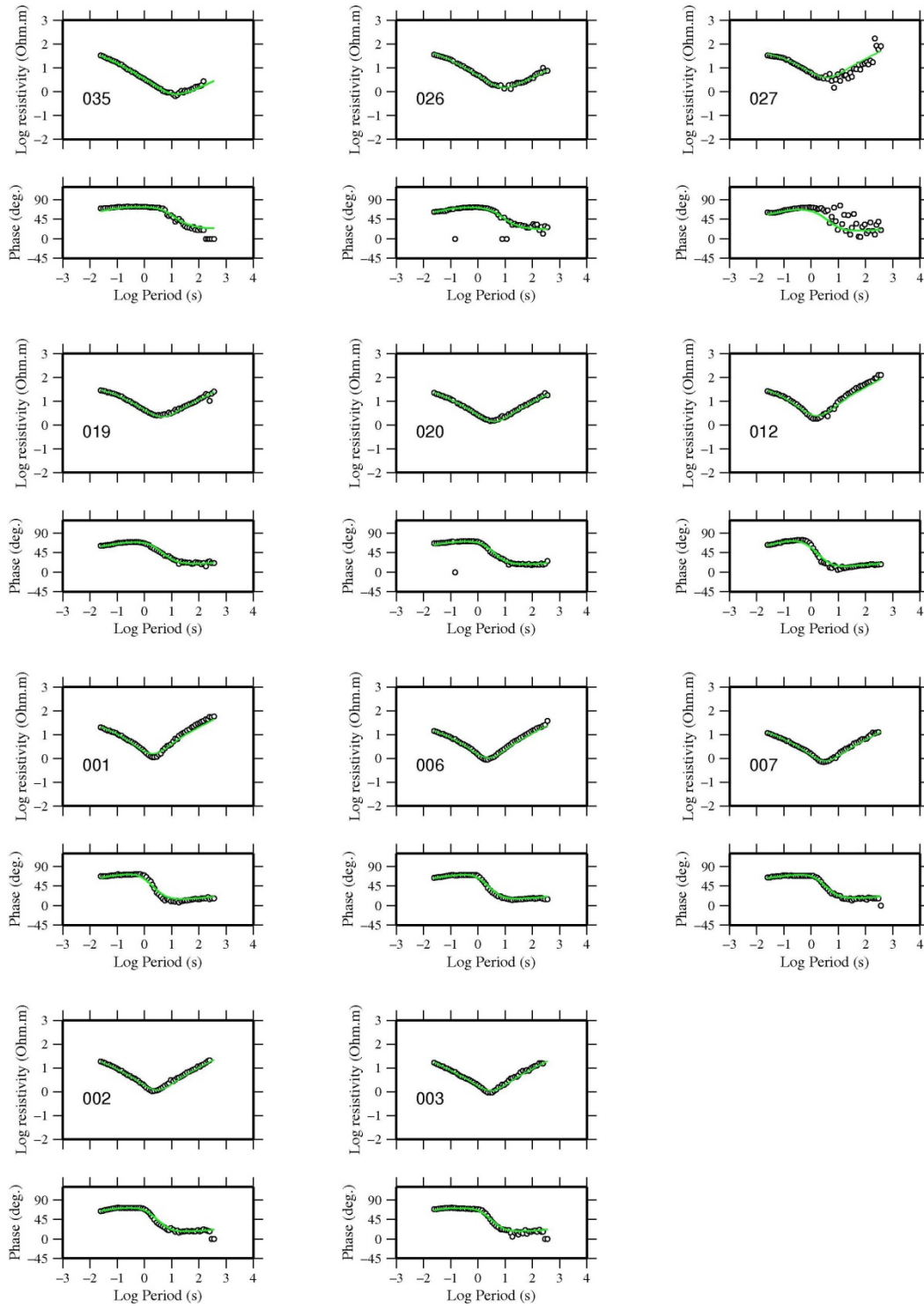***Figure C.6:*** *Fit of TM mode in joint TE and TM mode inversion apparent resistivity ρ_a in (Ωm) and phase ϕ in (°) of MT sites on Profile-2. Solid green curves show the response of the inversion model. The black circles are measured MT data points.*

Figure C.7: *Fits of the 2D inversion for TE mode apparent resistivity ρ$_a$ in (Ωm) and phase φ in (°) of MT sites on Profile ac-3000. Solid green curves show the response of the inversion model. The black circles are measured MT data points.*
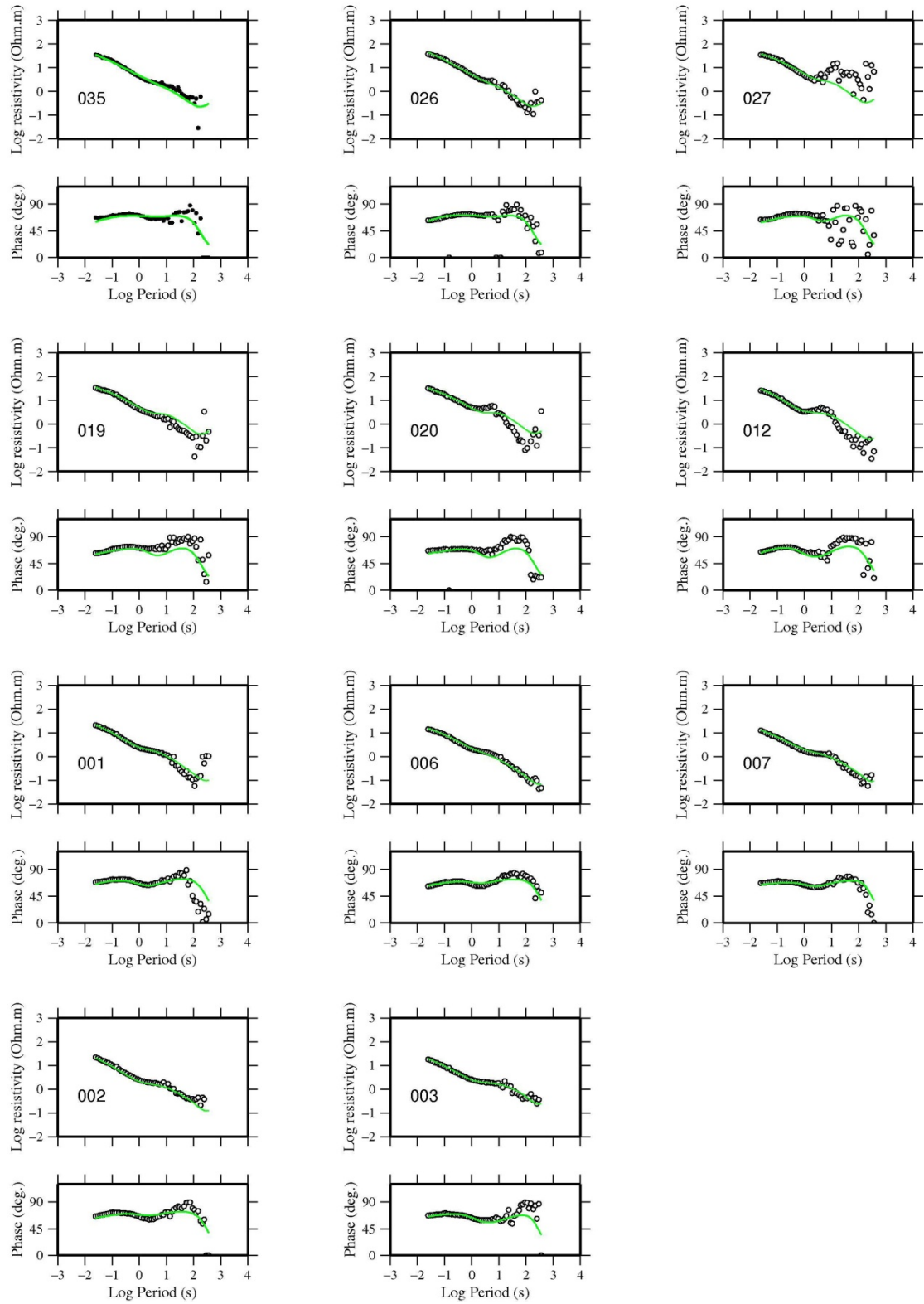
Figure C.8: *Fit of the 2D inversion for TM mode apparent resistivity ρ_a in (Ωm) and phase ϕ in (°) of MT sites on Profile ac-3000. Solid green curves show the response of the inversion model. The black circles are measured MT data points.*

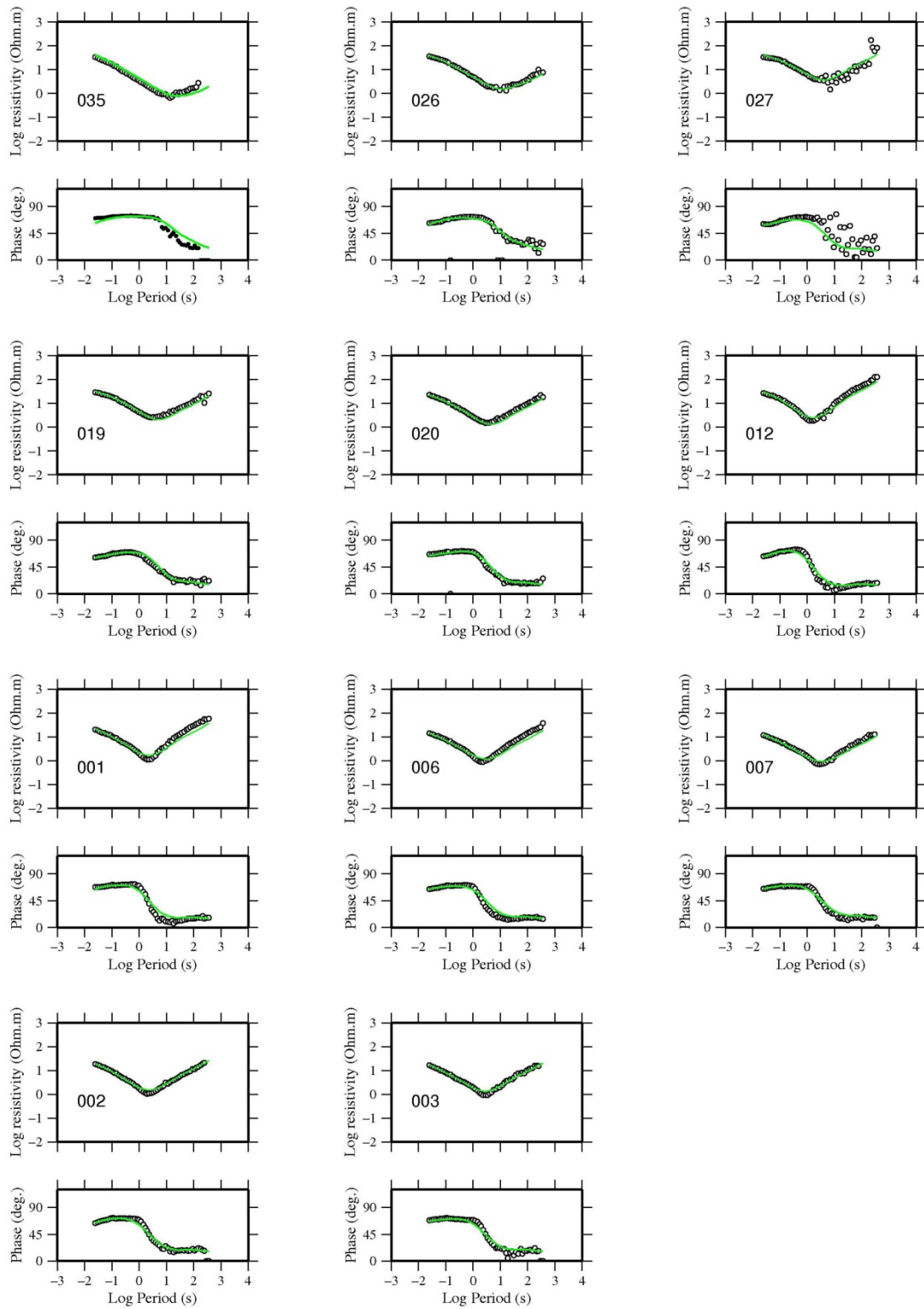***Figure C.9:*** *Fit of TE mode in joint TE and TM mode inversion apparent resistivity ρ$_a$ in (Ωm) and phase ϕ in (°) of MT sites on Profile ac-3000. Solid green curves show the response of the inversion model. The black circles are measured MT data points.*

Figure C.10: *Fit of TM mode in joint TE and TM mode inversion apparent resistivity ρ_a in (Ωm) and phase φ in (°) of MT sites on Profile ac-3000. Solid green curves show the response of the inversion model. The black circles are measured MT data points.*

***Figure C.11:*** *Fit of the 2D inversion for TE mode apparent resistivity ρ_a in (Ωm) and phase ϕ in (°) of MT sites on Profile al-1000. Solid green curves show the response of the inversion model. The black circles are measured MT data points.*

Figure C.12: *Fit of the 2D inversion for TM mode apparent resistivity ρ_a in (Ωm) and phase φ in (°) of MT sites on Profile al-1000. Solid green curves show the response of the inversion model. The black circles are measured MT data points.*

Figure C.13: *Fit of TE mode in joint TE and TM mode inversion apparent resistivity ρₐ in (Ωm) and phase ϕ in (°) of MT sites on Profile al-1000. Solid green curves show the response of the inversion model. The black circles are measured MT data points.*

Figure C.14: *Fit of TM mode in joint TE and TM mode inversion apparent resistivity ρₐ in (Ωm) and phase ϕ in (°) of MT sites on Profile al-1000. Solid green curves show the response of the inversion model. The black circles are measured MT data points.*

APPENDIX D: 3D MT Inversion Responses

The following Figures presents model responses and measured MT data for apparent resistivity (ρ_{xy} and ρ_{yx}) in (Ωm) and phase ϕ in (°) of MT sites from 3D inversion.
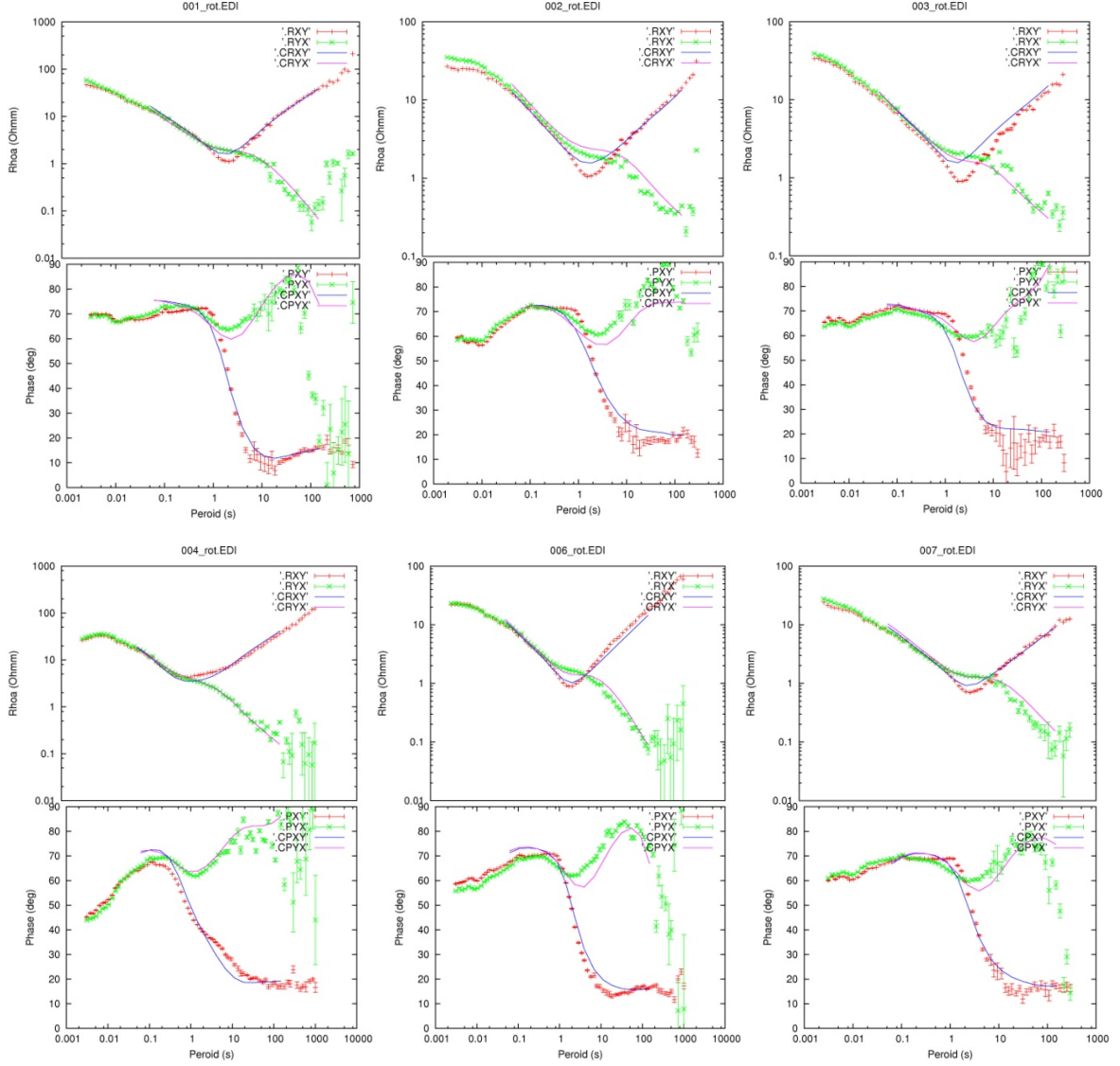
Figure D: *Fits of measured data values and model responses for the apparent resistivity and phase of MT sites from 3D inversion. Blue and purple solid lines: calculated responses of apparent resistivity and phase for xy and yx components, respectively. Red pluses and Green crosses: static shift corrected apparent resistivity and phase measured data for xy and yx components, respectively.*
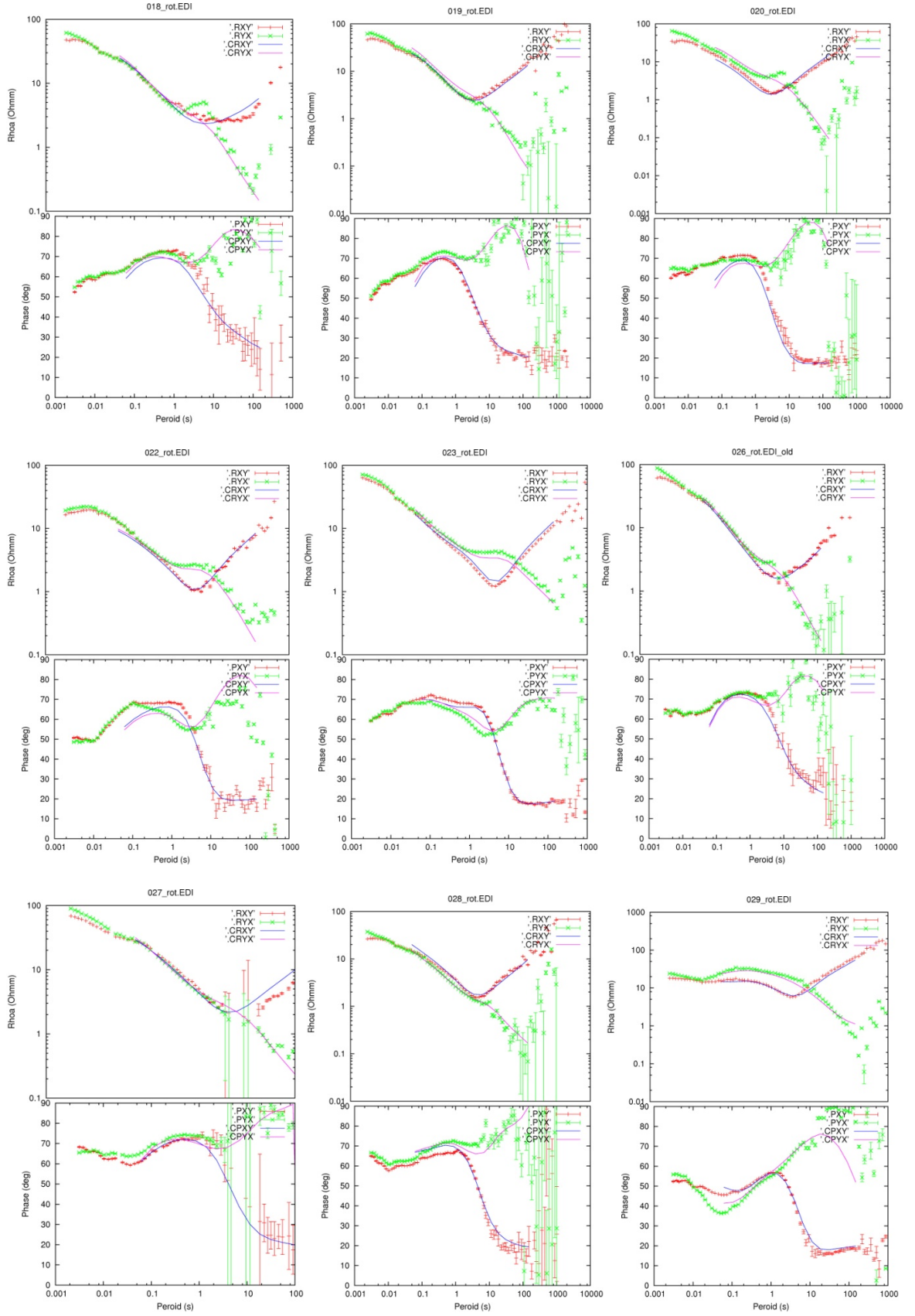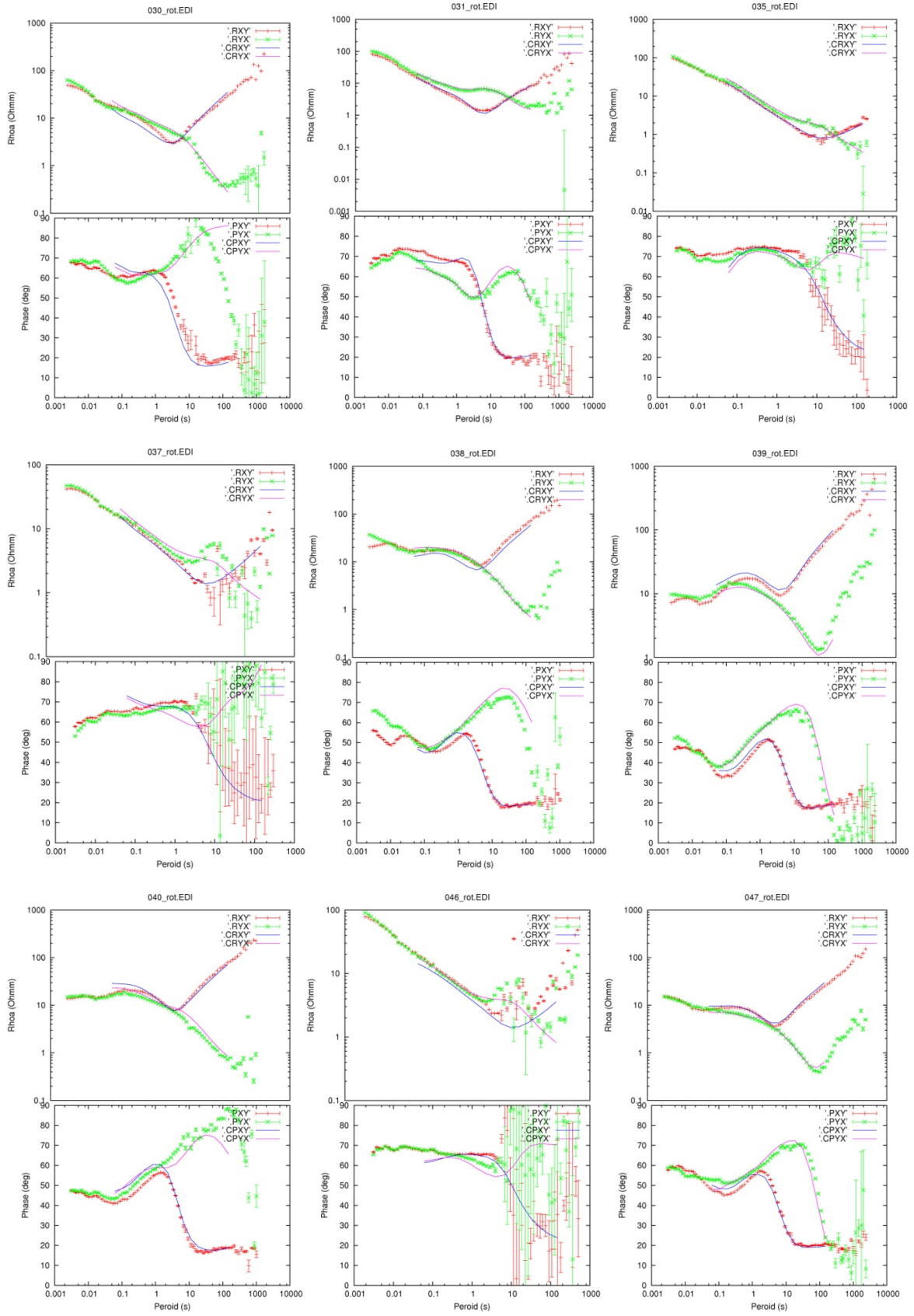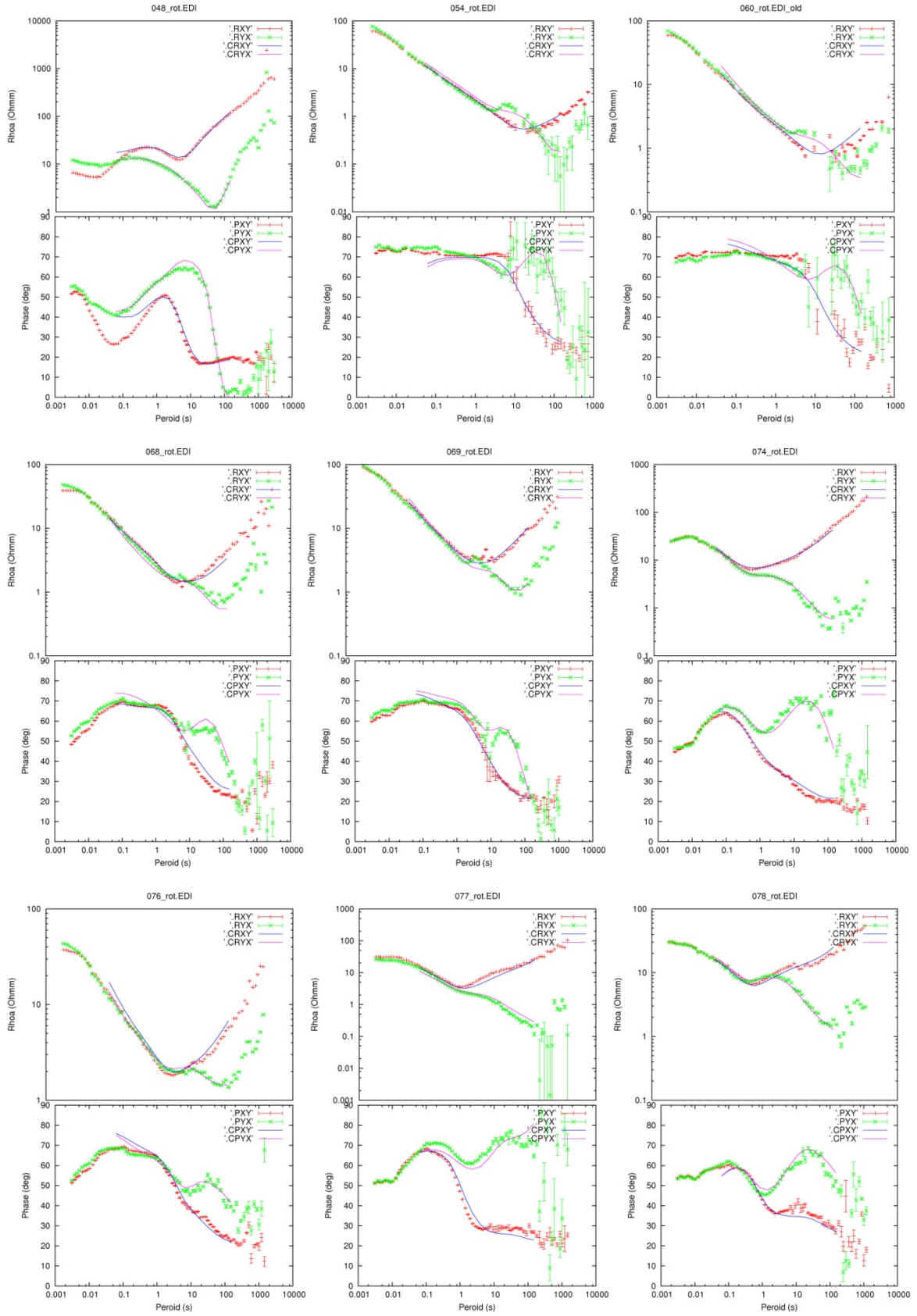
Figure D. Continued.

116

Figure D. Continued.

Figure D. Continued.
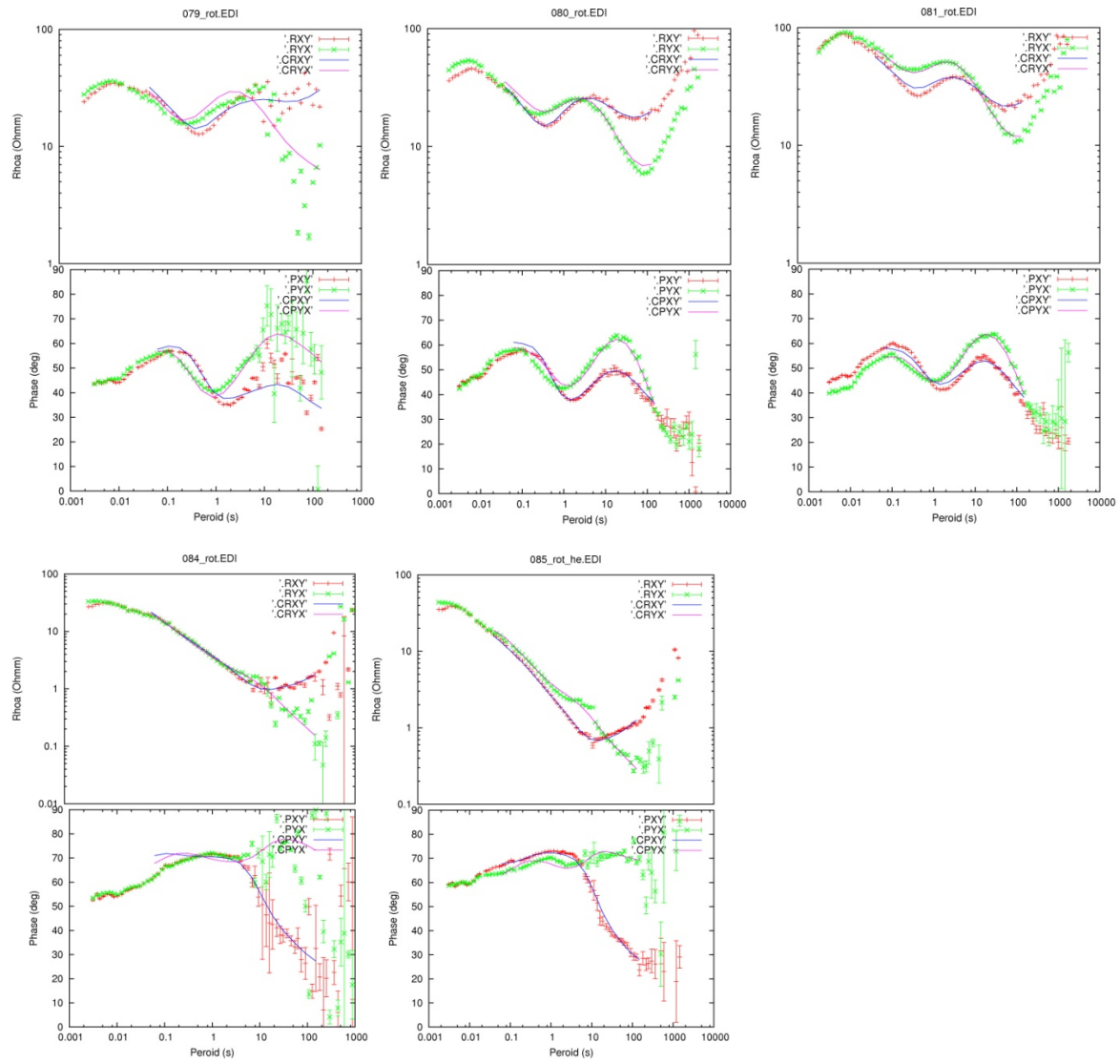
Figure D. Continued.

Figure D. Continued.